

Integration of Energy Storage in Solar-powered EV Smart Charging Systems

Vermeer, W.W.M.

DOI

[10.4233/uuid:88864ea7-6afd-4f6f-a36d-6f55010654a8](https://doi.org/10.4233/uuid:88864ea7-6afd-4f6f-a36d-6f55010654a8)

Publication date

2023

Document Version

Final published version

Citation (APA)

Vermeer, W. W. M. (2023). *Integration of Energy Storage in Solar-powered EV Smart Charging Systems*. [Dissertation (TU Delft), Delft University of Technology]. <https://doi.org/10.4233/uuid:88864ea7-6afd-4f6f-a36d-6f55010654a8>

Important note

To cite this publication, please use the final published version (if applicable). Please check the document version above.

Copyright

Other than for strictly personal use, it is not permitted to download, forward or distribute the text or part of it, without the consent of the author(s) and/or copyright holder(s), unless the work is under an open content license such as Creative Commons.

Takedown policy

Please contact us and provide details if you believe this document breaches copyrights. We will remove access to the work immediately and investigate your claim.

WILJAN VERMEER

INTEGRATION OF ENERGY STORAGE IN
SOLAR-POWERED EV SMART CHARGING SYSTEMS

INTEGRATION OF ENERGY STORAGE IN
SOLAR-POWERED EV SMART CHARGING SYSTEMS

DISSERTATION

for the purpose of obtaining the degree of doctor
at Delft University of Technology
by the authority of the Rector Magnificus, Prof. dr. ir. T.H.J.J. van der Hagen,
chair of the Board for Doctorates,
to be defended publicly on Wednesday 4th October 2023 at 17:30 o'clock.

by

Wiljan Wilhelmus Martinus VERMEER
Master of Science Electrical Engineering, Delft University of Technology, the
Netherlands
born in 's-Hertogenbosch, the Netherlands
2023

This dissertation has been approved by the promotor

Composition of the doctoral committee:

Rector Magnificus,	chairperson
Prof. dr. ir. P. Bauer,	Delft University of Technology, promotor
Dr. ir. G.R. Chandra Mouli,	Delft University of Technology, copromotor

Independent members:

Prof. dr. Madeleine Gibescu	Utrecht University
Prof. dr. ir. Omar Hegazy	Free University of Brussels
Prof. Dr.sc.techn. Dmitry Vinnikov	Tallin University of Technology
Prof. dr. ir. Olindo Isabella	Delft University of Technology
Prof. dr. ir. Marjan Popov	Delft University of Technology



Printed by: Proefschrifprinten.nl

Copyright © 2023 by Wiljan Vermeer

ISBN 978-94-6366-737-1

An electronic version of this dissertation is available at
<http://repository.tudelft.nl/>.

To all my loved ones.

SUMMARY

This thesis investigates the integration of electric vehicle (EV) charging, photovoltaic (PV) power, and battery energy storage (BES), using a direct current (DC) integrated multi-port power converter. The goal is to aid the energy transition using the intelligent operation of the aforementioned components to provide a more cost-effective system that helps increase the penetration of small-scale local PV system and increase the sustainability of local loads, such as EV charging. To achieve this, this work focuses on two parts: the power electronic converter and the smart charging control, including battery degradation.

POWER ELECTRONICS

In this thesis a modular DC-integrated multi-port converter is developed. The DC integration allows to reduce the amount of power converters hereby reducing its costs, while increasing efficiency and power density. All converters ports are developed for bidirectional operation to maximize its flexibility. a two level DC-AC converter is used for the bidirectional AC grid connection. Next, a 4-phase interleaved flyback converter is used for isolated EV charging. Finally, two interleaved four-switch buck-boost (FSBB) converters are used for both the PV and BES ports. All DC-DC converters utilize quasi-resonant boundary conduction mode (QR-BCM), combined with silicon carbide semiconductors to achieve efficiencies up to above 99%. A novel control method for the interleaved FSBB converter is proposed to enable multi-mode QR-BCM operation. Based on an experimental comparison with three other soft-switching modulation schemes it is shown that the proposed modulation and control achieve the highest efficiency (up to 99.5%) with little to no compromise in power density and control complexity.

SMART CHARGING

Next, a two-level smart charging structure is proposed to utilize the flexibility obtained from the multi-directional power electronic hardware. The first level is a non-linear programming (NLP) model that optimizes the charging powers of the EV and BES in a moving horizon context, to minimize the operational costs, including primary frequency control market participation and battery degradation. To minimize the battery degradation, a literature

survey study has been done on lithium-ion ageing mechanisms and how to model it. Based on this survey the best suited degradation model is chosen and integrated in the NLP model. The second level of the proposed smart charging structure recalculates the setpoints based on grid frequency deviation, and PV forecasting errors.

Both the theoretical and experimental results show that the proposed control method is effective in reducing the lifetime system costs. In combination with optimal sizing of the components the total lifetime system costs can be reduced up to 460% compared to conventional non-optimal charging methods.

SAMENVATTING

Dit proefschrift onderzoekt de integratie van het opladen van elektrische voertuigen (EV), fotonvoltaïsch ("photovoltaic" PV) vermogen en accu-energieopslag ("battery energy storage" BES), met behulp van een geïntegreerde gelijkstroom ("direct current" DC) multi-poort vermogensomvormer. Het doel is de energietransitie te ondersteunen door het instaat stellen van de intelligente werking van de bovengenoemde componenten. Met als resultaat een meer kosteneffectief systeem dat helpt met de toename van kleinschalige lokale PV-systemen en de verduurzaming van lokale belastingen, zoals het opladen van EV's. Om dit te bereiken richt dit werk zich op twee onderdelen: de vermogens-elektronische omvormer en de slimme laadregeling, inclusief batterijdegradatie.

VERMOGENSELEKTRONICA

In dit proefschrift wordt een modulaire DC-geïntegreerde multipoortconverter ontwikkeld. De DC-integratie maakt het mogelijk het aantal vermogensomzetter te verminderen, waardoor de kosten worden verlaagd, terwijl de efficiëntie en vermogensdichtheid toenemen. Alle omvormers zijn ontwikkeld voor bidirectionele werking om de flexibiliteit te maximaliseren. Een DC-AC-converter met twee niveaus wordt gebruikt voor de bidirectionele AC-netaansluiting. Vervolgens wordt een 4-fase interleaved flyback converter gebruikt voor het geïsoleerd opladen van EV's. Ten slotte worden twee interleaved four-switch buck-boost (FSBB) omvormers gebruikt voor zowel de PV- als de BES-poorten. Alle DC-DC converters maken gebruik van quasi-resonante grensgeleidingsmodus ("quasi-resonant boundary conduction mode" QR-BCM), gecombineerd met siliciumcarbide halfgeleiders om rendementen tot boven 99% te bereiken. Er wordt een nieuwe regelmethode voor de FSBB-omvormer voorgesteld om een multimodale QR-BCM-werking mogelijk te maken. Uit een experimentele vergelijking met drie andere soft-switching modulatie methodes blijkt dat de voorgestelde modulatie en regeling de hoogste efficiëntie bereiken (tot 99,5%) met weinig tot geen compromissen in vermogensdichtheid en regelcomplexiteit.

SLIMME LAADREGELING

Vervolgens wordt een slimme laadstructuur op twee niveaus voorgesteld

om de flexibiliteit te benutten die wordt verkregen door de multidirectionele vermogenslektronika. Het eerste niveau is een non-linear programming model (NLP) dat het laadvermogen van de EV en de BES optimaliseert in een moving horizon context, om de operationele kosten te minimaliseren, met inbegrip van deelname aan de markt voor primaire frequentieregeling en inzicht in de degradatie van de batterijen. Om de batterijdegradatie te minimaliseren is een literatuuronderzoek gedaan naar lithium-ion verouderingsmechanismen en hoe deze gemodelleerd kunnen worden. Op basis van dit onderzoek is het meest geschikte degradatiemodel gekozen en geïntegreerd in het NLP-model. Het tweede niveau van de voorgestelde slimme laadstructuur herberekent de setpoints van het laadvermogen op basis van afwijkingen in de netfrequentie en PV-voorspellingsfouten. Zowel de theoretische als de experimentele resultaten tonen aan dat de voorgestelde regelmethode effectief is in het verminderen van de levensduurkosten van het systeem. In combinatie met een optimale dimensionering van de componenten kunnen de totale levensduurkosten van het systeem tot 460% worden verminderd in vergelijking met conventionele niet-optimale laadmethoden.

CONTENTS

1	Introduction	1
1.1	Background & Motivation	1
1.1.1	Overcoming the challenges of a decentralized energy system	2
1.1.2	Smart Direct Current Integration of EV, PV, and BES	4
1.2	Research Objective	5
1.3	Thesis Outline	7
1.4	Scientific Contributions	9
1.4.1	Publications	10
2	Four-Switch Buck-Boost Converter Design	15
2.1	Introduction	16
2.1.1	Related Work	16
2.1.2	Contribution	19
2.2	Modulation Strategy	20
2.2.1	Deriving the proposed modulation	20
2.2.2	Proposed buck-boost modulation	25
2.3	Implementation & Control	26
2.3.1	Digital Control for Interleaved QR-BCM	26
2.3.2	Feed-forward Mode Transitions	29
2.4	Experimental Verification	31
2.4.1	FSBBC Modulation Comparison	34
2.5	Chapter Conclusion	38
3	Multi-Port Converter Development	39
3.1	Introduction	40
3.2	Related Work	40
3.2.1	AC integration	40
3.2.2	High-frequency transformer integration	41
3.2.3	DC integration	42
3.2.4	Contribution	42
3.3	Design of the Multi-port Converter	43
3.3.1	DC-AC Converter	44
3.3.2	EV Converter	45
3.3.3	PV & BES converter	47
3.4	Closed loop Control	48
3.4.1	DC/AC converter	48

3.4.2	BES converter	50
3.4.3	PV converter	50
3.4.4	EV converter	51
3.5	Experimental Verification	52
3.5.1	Interleaved Flyback Converter	52
3.5.2	DC-AC Converter	52
3.5.3	Cascaded Control & Protection	54
3.5.4	Multi-port System Efficiency	54
3.6	Chapter Conclusions	54
4	Modelling Battery degradation	59
4.1	Introduction	60
4.1.1	Modelling of Battery degradation	60
4.1.2	Challenges of Empirical and Semi-empirical degradation Models	62
4.1.3	Related Work & Scientific gap	63
4.1.4	Contribution	64
4.2	Main degradation Mechanisms	65
4.2.1	Anode degradation	68
4.2.2	Cathode degradation	72
4.3	Review of Empirical Degradation Modelling	75
4.3.1	Calendar degradation	75
4.3.2	Cyclic degradation	86
4.4	Current Challenges & Future Trends	111
4.4.1	New Battery Chemistries	112
4.4.2	Second-life Batteries	112
4.4.3	Fast Charging	113
4.4.4	Thermally Managed Systems	113
4.4.5	Artificial Intelligence for degradation Estimation	113
4.5	Selection of degradation model	114
4.6	Chapter Conclusions	115
5	Optimal Control & Sizing	117
5.1	Introduction	118
5.1.1	Chapter Organisation	120
5.1.2	Related Work	120
5.1.3	Contribution	123
5.2	Control Structure	124
5.3	Optimal Scheduling	125
5.3.1	Objective Function	126
5.3.2	Constraints	129

5.4	Real-Time Control	137
5.4.1	without FCR	137
5.4.2	with FCR	138
5.5	Case Studies	139
5.6	Results: Optimal Scheduling	141
5.6.1	Optimal Power Management & Component Size	141
5.7	Results: Real-Time Control	146
5.7.1	Lifetime Net Present Costs	146
5.7.2	Effect of Component Degradation	148
5.7.3	Sensitivity Analysis	150
5.8	Chapter Conclusions	151
6	Smart Charging Integration	153
6.1	Introduction	154
6.2	Integrating Smart Charging Control	154
6.3	Results: Smart Charging	155
6.3.1	Charging Scheme Comparison	158
6.4	Chapter Conclusions	161
7	Conclusion	163
7.1	Regarding Research Questions	163
7.1.1	Multi-mode QR-BCM modulation	164
7.1.2	Modulation comparison	164
7.1.3	Topology selection	165
7.1.4	Closed-loop control	165
7.1.5	Optimal sizing	168
7.1.6	Smart Charging Control	169
7.1.7	Modular DC-integrated multi-port converter	170
7.1.8	Integrated Hierarchical Smart Charging Control	171
7.2	Future Work	172
7.2.1	Ancillary service control for DC-AC converter	172
7.2.2	Stand alone off-grid operation	172
7.2.3	Benchmarking smart charging algorithms	172
7.2.4	Artificial Intelligence for parameter estimation	173
8	Appendix	175
8.0.1	Loss modelling	175
8.0.2	Passive component sizing	175
	Bibliography	177

INTRODUCTION

1.1 BACKGROUND & MOTIVATION

To reduce emissions from sectors such as the built environment and transportation, it is critical that they are electrified and powered by renewable energy sources (RES). However, this electrification and decentralization, poses significant challenges on the existing infrastructure as it is not equipped for this increased electrical demand and generation. This is visualized in the congestion heat map of the Netherlands shown in Fig. 1(a)-(b). The heat maps are directed to electricity producers or consumers, from here on abbreviated as prosumers, requiring a grid connection larger $3\times 80A$. The figures show that already the majority of the large-scale Dutch prosumers are already facing congestion issues on a regular basis. Even worse, for a significant part of the country it is already prohibited to install new connections of above $3\times 80A$ for feeding in energy, such as large-scale solar-PV installations.

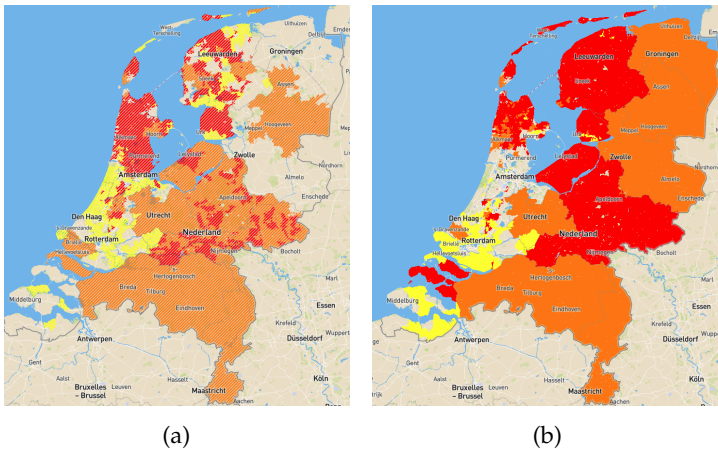


FIGURE 1: Heat maps of congestion in the dutch electricity network, (a): demand and (b): generation. Yellow indicates that there is thread of scarcity of transport, orange is a pre-announcement of structural congestion, and red indicates that congestion is a structural problem in the grid [1].

To put this in perspective, in 2021 only 12.28% of the national energy consumption in the Netherlands was powered by RES [2]¹. Additionally, in sectors such as transport, the majority (91% in 2021) is still directly powered by burning fossil fuels and, therefore, first need to be electrified² before they can become sustainable. Fortunately, the share of electric vehicles in new car sales has drastically increased over the last five years, from 1.1% in 2016 to 21.6% in 2021, and this number is expected to increase in the future [3]. However, the electrification of transport will result in a drastic increase of electrical power and energy. In 2021 the energy used for transportation was approximately equal to all electrical energy [2]. A complete electrification of transport would therefore significantly increase the total electrical energy demand. In the future this will further increase as the number of electrical loads increases, e.g. electrical heating & cooling.

To sum up, the electrical energy demand is expected to significantly increase in the near future. However, the current electricity grid in the Netherlands is already regularly facing issues regarding congestions. Densely populated areas, like the west of the Netherlands, are mostly congested in terms of demand, hereby holding back the electrification of major loads such as transportation. Similarly, the less densely populated areas face problems with feeding in power, which is holding back the generation of sustainable energy. Therefore, to meet the agreements made in the Paris Accords, and further increase the penetration of RES, as well as the electrification of the energy demand, decentralized and local solutions are required. As will be discussed in the next section.

1.1.1 *Overcoming the challenges of a decentralized energy system*

One solution of the above-mentioned problems is reinforcing the electrical infrastructure. However, this is only a temporary solution which does not directly increase the penetration rate of RES. Additionally, the high amount of manual labor required makes this an ineffective solution both in terms of cost and time [4]. Reinforcing the grid is therefore only considered a partial and long term solution.

So, if grid reinforcement and large scale generation do not solve the problem, it needs to be solved locally. This means local renewable generation for local demand, hereby reducing the stress on the electricity grid, reducing transportation losses, and reducing emissions. For small-scale local gen-

¹ The actual number is even slightly lower if biomass fuels are not considered.

² or powered from truly sustainable fuel

eration, solar PV is the best suited option as it can be easily installed on rooftops and its levelized cost of energy is lower than the price of 'gray' grid electricity [5].

However, PV has an intermittent character and is often not fully simultaneous with its demand. Therefore, energy storage is required to prevent excessively feeding in energy, and power loads when PV power is not available. Unlike solar PV, and despite decreasing prices, battery energy storage (BES) is still not very cost effective when used in combination with small-scale PV generation [5], due to multiple reasons:

- The lifetime of BES systems are in the range of 5-15 years, significantly shorter than PV system which have a lifetime of >25 years [6]. A reduced lifetime results in a lower return of investment.
- Additionally, the diurnal and seasonal variations of PV result in a poor utilization of the BES capacity. In summer, production often significantly exceeds demand. Whereas in winter, generation is low and demand is high. As a result, the battery is often fully depleted in winter, and almost always fully charged in summer [7].
- Finally, as long as feeding in energy is remunerated, through schemes like annual net metering, small scale BES systems do not have a strong business case when combined with local PV generation. Feed-in tariff, however, this will be phased-out in the future to discourage prosumers feeding in energy [8].

One possible solution to incentivize installation of prosumer BES systems, is to start using them for previously untapped business cases such as peak-shaving, the day-ahead market, or the frequency containment reserve (FCR) market. This could potentially reduce the return on investment period, and help in increasing RES integration. Currently, these markets are only available for large MW-scale systems, but the increasing amount of prosumers in the decentralized energy systems allows to aggregate their flexibility by energy management systems or by third party aggregators. However, these business cases require a high level of controllability, which is currently missing in conventional prosumer PV-BES systems.

Another option for increasing RES penetration could be to use EVs as energy storage. As the EV fleet increases, their charging demand is expected to cause congestion during peak hours. Charging EVs from local PV power could serve multiple purposes by alleviating the grid stress of both EV charging and PV power feed-in, while powering EVs with a truly sustainable source of energy. Additionally, using bidirectional EV

charging systems, the large energy capacity of EVs can be used for renewable energy storage. This is called vehicle-to-grid (V2g), or vehicle-to-x (V2x). The obvious advantage of V2x is that it does not require additional stationary BES systems. However, EVs are not always on site of the PV system. Furthermore, the additional battery wear due to V2x is a potential limiting factor. Nonetheless, V2x has attracted great societal and technical attention [9], with an increasing amount of V2x-ready charges and vehicles being developed.

It is concluded that, despite the individual challenges of local PV generation, PV energy storage, and EV charging, the combination of EV, PV, and BES shows great potential and synergy. However, this potential and synergy needs to be untapped by proper integration and control.

1.1.2 Smart Direct Current Integration of EV, PV, and BES

The most conventional solution is to integrate EV, PV and BES is to use multiple DC-AC converters, such as solar inverters and alternating current (AC) EV chargers, such as shown in Fig. 2(a). However, all these components are all fundamentally based on direct current (DC). Therefore an AC integrated solution requires several DC-AC conversion steps, which reduces the efficiency and power density and increases the cost. This can be improved using a DC-integrated solution, as shown in Fig. 2(b).

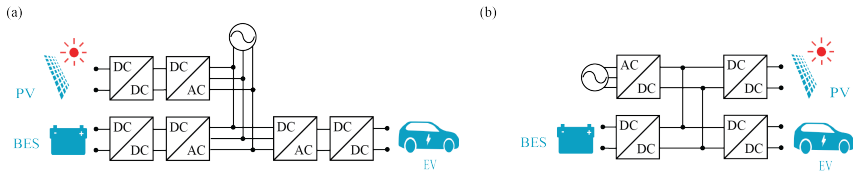


FIGURE 2: (a): AC integration, (b) DC integration of EV, PV and BES

However, only integrating EV, PV, and BES does not solve the high grid load, intermittent supply of renewable power, limited energy storage life-time, and increased ageing due to V2x. To solve these problems the solution requires a high level of intelligence, such as knowledge of: future demand and supply, energy prices, and the effects of battery ageing. Additionally, it requires the controllability to act on this knowledge. Only when all of these things are combined the appropriate actions can be determined. In the context of EV charging, such a high level of controllability is often referred

to as smart charging.

This thesis investigates how to intelligently integrate local PV power, bidirectional EV charging, and BES, to mitigate their individual challenges by optimizing the synergy between the components.

1.2 RESEARCH OBJECTIVE

To mitigate the challenges of a decentralized energy system with an increasing electrical demand, the main research objective of this thesis can be formulated as follows:

To enable intelligent operation of photovoltaic panels, bidirectional electric vehicle charging, and battery energy storage using a DC-integrated multi-port power converter.

The main research questions to achieve the research objective are:

To be able to enable the intelligent operation of PV energy, EV charging, and BES, the power electronic hardware needs to be developed with a good trade-off between efficiency, power density and costs. Since the PV and BES do not require galvanic isolation, the development costs could therefore be reduced if it possible to design one DC-DC converter suitable for both applications. In this regard, the first research question is stated as follows:

RQ1: How to design a highly-efficient and compact 10kW converter suitable for both PV and BES applications?

After the design of the non-isolated DC-DC converter, the design of the EV charger and DC-AC converter needs to be explored together with their integration into one multi-port converter. This is investigated in research question 2.

RQ2: How to design a DC-integrated multi-port converter for a 10kW EV, PV, BES, and AC grid-integrated smart charging system?

The second part of the thesis focuses on the intelligent control of the multi-port converter. As mentioned above, the multi-directional nature of the power converters requires a smart charging control scheme in order to utilize its high degree of freedom. Furthermore, truly intelligent control needs to be able to assess the trade-offs in its system. One of these trade-offs is the amount of battery power used versus its effect on battery lifetime. To understand this trade-off, a battery degradation is required. Therefore the third research question is stated as:

RQ3: How to model Li-ion battery degradation and how to mitigate it?

Once the processes in battery degradation are known, and a suitable battery degradation model is chosen, this knowledge can be used to determine how to optimize the control and dimensions of the system, and hereby achieve intelligent operation. This is investigated in the fourth research question.

RQ4: How to optimally size and control the integrated EV, PV, BES smart charging system to reduce the cost of energy and provide ancillary services?

Finally, the power electronic hardware and the smart charging control need to be integrated in order to quantify the benefits of the proposed smart charging system and verify its operation experimentally. This is the topic of the final research question.

RQ5: What are the benefits of the proposed smart charging system compared to a conventional AC-integrated charging system?

The outline of the thesis is discussed on the next pages.

1.3 THESIS OUTLINE

The five research questions above are each answered in a corresponding chapter. These chapters are divided into three parts, as shown in Figure 3. The first part focuses on the power electronic hardware. The second part focuses on the control system in place to optimally utilize the flexibility in the system. This includes a study on Li-ion battery degradation, to accurately assess the operational expenditure of energy storage. Finally, Part I and Part II are combined in Part III which includes the integration of the hardware and control and its experimental validation.

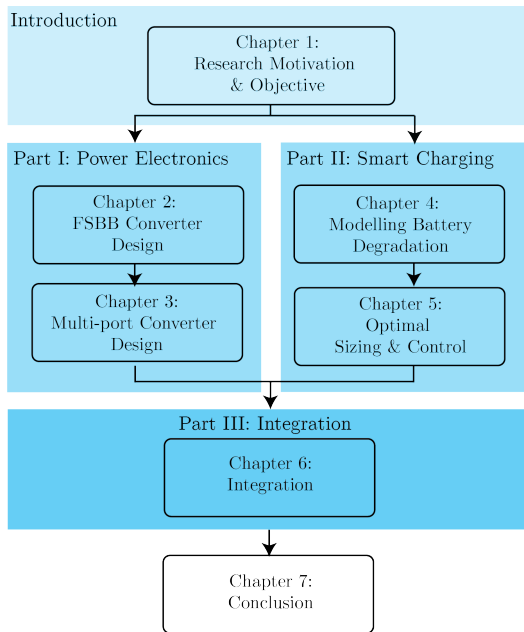


FIGURE 3: Outline of the thesis.

Part I: POWER ELECTRONICS

- **Chapter 2: Four-Switch Buck-Boost Converter Design (RQ₁)**

The goal of Chapter 2 is to design a non-isolated buck-boost converter applicable for both PV maximum power point tracking and battery charging. The buck-boost capability ensures that the converter is suitable for both single-phase and three-phase applications and a

wide range of PV and BES voltages. The focus of this chapter is on the derivation of a highly efficient quasi-resonant modulation scheme and its implementation. The modulation consists of three distinct operating modes, which ensure a high efficiency for any voltage. Additionally, a mode transition technique is presented that allows the converter to smoothly transition between the operating modes with different switching frequencies, without a loss of output power or large output ripple. Finally, an experimental comparison with three other-soft-switching modulation schemes for the same converter is performed.

- **Chapter 3: Multi-port Converter Development (RQ2)**

This chapter discusses the selection of multi-port converter topology based on a review of related studies. Afterwards it summarizes the design of the corresponding converter. Finally, the design of the closed loop control and protective measures are discussed.

Part II: SMART CHARGING

- **Chapter 4: Modelling Battery Ageing (RQ3)**

This chapter begins with an description of the main ageing mechanisms in Li-ion batteries. Next, a detailed review of empirical and semi-empirical battery ageing models is discussed, with a focus on operational stress factors and their interdependence, modelling techniques, limitations, and challenges. This allows the models to be used accurately at the relevant operating conditions.

- **Chapter 5: Optimal System Sizing and Control (RQ4)**

Chapter 5 discusses the developed hierarchical smart charging algorithm. The three level algorithm consists of an optimal scheduling algorithm that optimizes the power flows inside multi-port converter in a moving horizon window, a real-time controller that deals with forecasting errors, and the embedded control loops that ensure closed loop control and protection. This chapter focuses on the top two levels, as the embedded control is part of the power electronics section and is discussed in Chapter 1. The goal of the optimal scheduling algorithm is to minimize the cost of energy. This includes multiple business case, such as energy trading, FCR market participation, and battery degradation minimisation including second-life value. Additionally, it is also used to optimally size the components in the system.

Part III: INTEGRATION & EXPERIMENTAL VALIDATION

- **Chapter 6: Integration & Experimental Validation (RQ5)**

Chapter 6 aims to bridge the gap between smart charging algorithms and power electronic converters. This chapter discusses the implementation of the algorithm onto the multi-port converter. The experimental results show the operation and necessity of all three control levels. Finally, a comparison is made with between fixed-rate charging and direct-PV charging.

- **Chapter 7: Conclusion**

In the final chapter the key outcomes obtained from this thesis are discussed, and used to answer the main research questions of this thesis. Additionally, recommendations for future work are included.

1.4 SCIENTIFIC CONTRIBUTIONS

The key contributions of this work can be summarized as follows:

1. **A novel soft-switching modulation scheme for the four-switch buck-boost converter:** Most studies regarding soft-switching modulation schemes for the four-switch buck-boost converter (FSBBC) focus on constant frequency modulation schemes that allow for full zero-voltage-switching of the power switches. However, our work has indicated the short comings of constant frequency operation for wide-voltage range applications and proposed a novel variable-frequency multi-mode modulation scheme based on quasi-resonant boundary conduction mode. This includes a new mode transition technique that facilitates the multi-mode operation and hereby allows to simplify the switching pattern compared to constant frequency modulation schemes, without an imperative requirement of high-frequency current measurement.
2. **An extensive comparison of four-switch buck-boost modulation strategies:** The proposed FSBBC modulation is compared to three other soft-switching modulation schemes, including triangular current mode (TCM), bipolar quasi-resonant boundary conduction mode (B-QR-BCM), and constant-frequency quadrilateral current mode (CF-QCM). The proposed modulation strategy achieves the highest efficiency, and reduces the losses up to 60% compared to B-QR-BCM

and CF-QCM, with little to no compromise in terms of complexity and power density. Additionally, the obtained efficiency matches the highest reported efficiency of the FSBBC in the literature, despite a significantly higher power per phase and voltage range.

3. **A comprehensive review of battery degradation models:** Li-ion battery ageing, and empirical ageing models, are intensively studied in the literature. Several studies have proposed review papers on the ageing mechanisms of Li-ion batteries and the different types of ageing models used. However, for the first time, empirical and semi-empirical models are thoroughly reviewed and the correlations between different studies are investigated to highlight the limitations of the models, and focus on the reasons for the observed trends and insights. Due to the simplicity and widespread use of EMs, these limitations can potentially result in significant modelling errors.
4. **Integration of a novel smart charging control structure on the multi-port converter** For the first time in the literature, an actual industry compatible charging system is equipped with a smart charging control algorithm that optimizes its power flows and component ratings based on a unique combination of business cases such as, PV power forecasts, time-varying electricity prices, FCR market participation, and battery degradation. Our results show that the proposed system can significantly reduce the systems' return on investment period and improve lifetime revenue for the prosumer, while supporting the decentralized electricity grid.
5. **The integration of EV, PV, and BES using a 10kW DC-integrated, modular, multi-port converter:** The developed multi-port converter improves upon existing work by developing a modular, DC-integrated, four-port converter that integrates EV, PV, BES and DC-AC converter. In contrast to most studies in the literature the developed converter is compliant with industrial standards regarding EV charging and grid integration.

1.4.1 Publications

This thesis is based on the following journal publications:

- J1 W. Vermeer, M. Wolleswinkel, J. Schijfelen, G.R. Chandra Mouli, P. Bauer, *Design of a 10kW Multi-Port EV Smart Charging System Integrat-*

ing EV, PV, and Battery, 2023, (under review for) *IEEE Transactions on Transportation Electrification*

- J2 W. Vermeer, M. Wolleswinkel, J. Schijffellen, G.R. Chandra Mouli, P. Bauer, *Three-Mode Variable-Frequency Modulation for the Four-Switch Buck-Boost Converter: a QR-BCM vs. TCM Case Study and Control Implementation*, 2022, (under review at) *IEEE Transactions on Industrial Electronics*
- J3 W. Vermeer, G.R. Chandra Mouli, P. Bauer, *Optimal Sizing & Control of a PV-EV-BES Charging System Including Primary Frequency Control and Component Degradation*, 2022, *IEEE Open Journal of Industrial Electronics*
- J4 W. Vermeer, G.R. Chandra Mouli, P. Bauer, *A Comprehensive Review on the Characteristics and Modelling of Lithium-ion Battery Ageing*, 2022, *IEEE Transactions on Transportation Electrification*
- J5 W. Vermeer, G.R. Chandra Mouli, P. Bauer, *Real-time Building Smart Charging System Based on PV forecast and Li-ion Battery Degradation*, 2019, *Energies*

Other (conference) publications, not discussed in this thesis:

- C1 W. Vermeer, S. Bandyopadhyay, P. Bauer, (2019, June). *Design of Misalignment Tolerant Control for an Inductive Charger with V2G Possibilities. In 2019 IEEE PELS Workshop on Emerging Technologies: Wireless Power Transfer (WoW)* (pp. 273-278).
- C2 Vermeer, W., Stecca, M., Mouli, G. R. C., Bauer, P. (2021, April). *A Critical Review on The Effects of Pulse Charging of Li-ion Batteries. In 2021 IEEE 19th International Power Electronics and Motion Control Conference (PEMC)* (pp. 217-224). IEEE.
- C3 W. Vermeer, G.R. Chandra Mouli, P. Bauer, (2022, June). *A Multi-Objective Design Approach For PV-Battery Assisted Fast Charging Stations Based on Real Data. In 2022 IEEE Transportation Electrification Conference & Expo (ITEC)* (pp. 114-118). IEEE.
- C4 M. Stecca, W. Vermeer, T.B. Soeiro, L.R. Elizondo, P. Bauer, P. Palensky, (2022, June). *Battery Storage Integration in EV Fast Charging Station for Increasing its Revenues and Reducing the Grid Impact. In 2022 IEEE Transportation Electrification Conference & Expo (ITEC)* (pp. 109-113). IEEE.

- C5 D. Gaona, W. Vermeer, G.R.C. Mouli. P. Bauer, (2022, September). *Assessing the Demand Response Potential of Heat Pumps in All-Electric Buildings Equipped with PV, EV (V2G) and BES to Minimize Energy Costs. In 2022 IEEE 20th International Power Electronics and Motion Control Conference (PEMC)* (pp. 174-181). IEEE.

Part I
POWER ELECTRONICS

FOUR-SWITCH BUCK-BOOST CONVERTER DESIGN

This chapter discusses the derivation of a new modulation and its control implementation for the four-switch buck-boost converter, used for both the PV maximum power point tracking and BES charging. First, an analysis of a variable-frequency modulation is used to analyze and derive all degrees of freedom in the design. Conventional QR-BCM buck and boost operation proves the most efficient, but includes a power control discontinuity for voltage gains close to unity. To overcome this a new three-mode QR-BCM operation is derived. Additionally, a new mode transition technique for interleaved, multi-mode, variable frequency operation of the FSBBC is presented. The presented mode transition techniques enables the closed-loop operation of three-mode modulation, and hereby enables optimal efficiencies in all three modes.

This chapter is based on:

J2 W. Vermeer, M. Wolleswinkel, J. Schijffellen, G.R. Chandra Mouli, P. Bauer, *Three-Mode Variable-Frequency Modulation for the Four-Switch Buck-Boost Converter: a QR-BCM vs. TCM Case Study and Control Implementation*, 2022, (under review for) *IEEE Transactions on Industrial Electronics*

2.1 INTRODUCTION

This chapter focuses on the design of the converter used for both the PV and BES ports. Because of the similarity in specifications, the same 10kW interleaved FSBBC can be used for both non-isolated ports. The FSBBC is a common topology for applications with overlapping in- and output voltages because of its bidirectional buck and boost capabilities and relatively low component stress. Fig. 4 shows the FSBBC topology with switches S_{1-4} , and their parasitic drain-sources capacitances C_{ds1-4} .

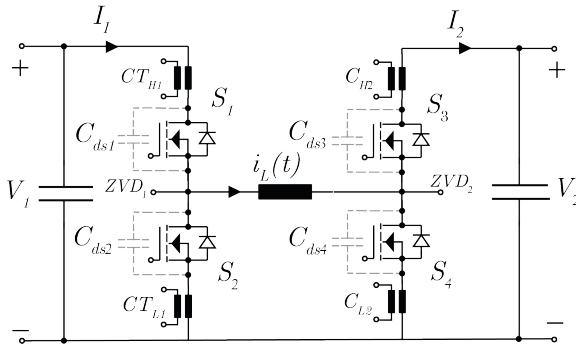


FIGURE 4: The cascaded buck-boost converter, with current transformers (CT_x) for measurement and protection.

2.1.1 Related Work

In most parts of its operating region, the FSBBC can be controlled similarly to a conventional half-bridge buck or boost converter. However, a third mode is often required for voltage gains close to one [10] due to practical duty cycle limitations. The transitions between these modes cause discontinuities in power control, and achieving smooth mode transitions during operation is still an ongoing topic in research. Table 12 summarizes the related studies regarding different modulation strategies for the FSBBC. The comparison criteria are whether they can switch softly, either zero-voltage switching (ZVS), or zero-current switching (ZCS) the number of control variables (N_{ctrl}), include interleaving (Interl.), the control scheme used (Control), maximum power (Power), and peak efficiency (η_{pk}). The first part regarding continuous conduction mode is mostly focused on achieving smooth mode transitions. For example, the authors of [10] present a tech-

nique to compensate for the transition region discontinuity and boost region non-linearity. In [11], the authors present a digital adaptive on-time controller for smooth mode transitions and fast reference tracking performance. Multiple 3- and 4-mode modulation schemes are derived in [12], which are compared based on inductor current ripple. However, these hard-switching strategies are limited in their power density and efficiency and have only been validated on low-power single-phase prototypes and, therefore not necessarily applicable to higher powers.

Study	Modulation	ZVS	N_{ctrl}	Interl.	Control	Power	η_{pk}
[10]	CCM	x	1	x	PI	2W	x
[12]	CCM	x	1	x	PI	60W	99%
[13]	CCM	x	1	x	PI	≤ 50 W	x
[11]	CCM	x	1	x	PI	700W	98.5%
[14]	CCM	x	1	x	PID	25W	96%
[15]	CCM	x	1	x	PID & FF	≤ 3 W	97%
[16]	VF-CCM	x	2	x	PI	100W	99.3%
[17]	CCM+DCM	x	2	x	MPC	25W	93.5%
[18]	CCM	x	2	x	PI	300W	98%
[19]	CCM	x	2	x	type-III & FF	3W	95%
[20]	CF-CCM	✓	3	x	PI	220W	95%
[21]	CF-QCM	✓	3	x	x	3kW	99.4%
[22]	CF-QCM	✓	3	✓	LUT	12kW	98.3%
[23]	CF-QCM	✓	3	x	LUT	300W	98%
[24]	CF-QCM	✓	3	x	x	200W	97.8%
[25]	CF-QCM	✓	3	x	PI	300W	98.5%
[26]	CF-QCM	✓	2	x	LUT	200W	98.8%
[27]	VF-QCM	✓	3	x	x	3kW	99.6%
[28]	QCM+QR-BCM	✓	1	x	x	3kW	98.1%
[29]	CF-QCM	✓	3	x	type-I	500W	98.7%
[30]	CF-QCM	✓	3	x	LUT	280W	98.1%
[31]	TCM+B-QR-BCM	✓	1	x	x	1kW	99.5%
[32]	QR-BCM	✓	1	x	x	500W	97%
Prop.	QR-BCM	✓	1	✓	type-III & FF	10kW	99.6%

TABLE 1: Related studies regarding modulation strategies for the FSBBC. Acronyms: Look-up table (LUT), Feed Forward (FF), Proportional (P), Integrator (I), derivator (D), Variable (V)/Constant (C) frequency (F), Model Predictive Control (MPC)

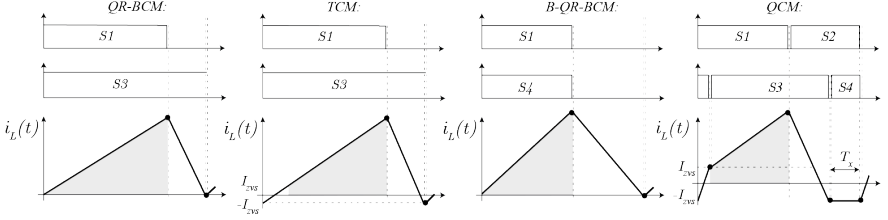


FIGURE 5: Gate signals and inductor current for QR-BCM, TCM, bipolar QR-BCM (B-QR-BCM) and QCM [28]. The grey area under the current waveform represents the amount of power transferred. For simplicity, all switching instances are depicted as ideal. However, all strategies employ quasi-resonant switching to achieve ZVS or ZCS.

At higher powers, soft-switching strategies provide much better performance. For the FSBBC, these studies can be divided into two parts, constant-frequency (CF) quadrilateral current modulation (QCM) and triangular current modulation (TCM) (or similarly boundary conduction mode (BCM), or quasi-resonant BCM (QR-BCM)). The basic implementation of these modulations is shown in Fig. 5. QR-BCM and TCM are widely applied with buck or boost converters, in literature and industry, due to their high efficiency and relative simplicity. However, when applied to the FSBBC, the multi-mode operation poses additional control challenges due to discontinuities in the switching frequency. In [31], the authors use unipolar TCM in the buck and boost regions and bipolar TCM (B-TCM) in the buck-boost region. Despite high peak efficiencies in buck and boost mode, the high frequency and increased inductor root-mean-square (RMS) current in buck-boost mode forms a thermal bottleneck in the overall design. Additionally, the authors do not present a way to overcome the switching frequency discontinuity. It is likely that because of this discontinuity, no study has yet shown closed-loop operation for (QR-)BCM or TCM, including voltage variations near unity voltage gain, using the FSBBC, as shown in Table 12. On the contrary, the QCM modulation strategies operate at a constant frequency and do not require any mode transitions. Furthermore, the high degree of freedom (the duty cycle of each half-bridge D_{S1} , D_{S3} and the phase-shift θ between them) can be used to minimize inductor RMS current [23], freewheeling current [24], or overall total losses [30]. However, the resulting switching patterns are very complex and can have up to three independent control variables (D_{S1} , D_{S3} , and θ), as shown under N_{ctrl} in Table 12. As a result, regular controllers alone are insufficient and complex 3D look-up tables (LUT) are required. Also, sufficient care has to

be taken when designing these look-up tables to prevent discontinuities and instabilities [22]. Additionally, for applications with wide voltage- and power ranges the look-up tables become very large, and require external RAM/storage [25]. This complicates digital hardware design, and the data latency limits possible controller bandwidth. In [25] the authors have overcome this by simplifying the switching pattern. Similarly, in [29] the authors simplified the QCM switching pattern by defining a continuous and discontinuous QCM operating mode, with corresponding mode transitions, in order to negate the necessity of a look-up table. Finally, it is concluded in [23, 29, 30] that the RMS current under QCM can be minimized by reducing the circulating current period (T_x in Figure 5) and by shortening the initial rising flank. In [28] T_x is even set to zero to minimize peak current. The downside of the resulting variable frequency QR-BCM modulation is that it requires multiple operating modes and corresponding mode transitions, which were not proposed in [28].

To conclude, significant efforts have gone into optimizing and simplifying the QCM modulation strategies. However, the constant frequency operation is an inherent limitation of efficiency. On the other hand, variable frequency modulation strategies show very high potential efficiencies but have multiple operating modes and research into mode transitions for variable frequency modulation strategies is lacking (in contrast to CCM schemes).

2.1.2 Contribution

Based on the literature review presented above, the main contributions of this chapter are summarized as follows:

- The first design of a 10kW interleaved FSBBC converter operating in closed-loop quasi-resonant BCM, including smooth mode transitions for multi-mode variable-frequency operation.
- A new control scheme is proposed that allows to simplify the switching pattern compared to QCM strategies and does not require any look-up tables. Furthermore, it does not have an imperative requirement for high-frequency current measurement.
- Our calculations show that adopting QR-BCM with zero-current switching allows simplifying the converter design and control, without a decrease in efficiency, compared to zero-voltage switching triangular current mode (TCM).

2.2 MODULATION STRATEGY

The converter specifications are shown in Table 2. To improve power density and efficiency, a 2-phase interleaved converter will be developed. However, all analysis in this section is generic for single- and multi-phase converters. Hence, a 5kW single-phase converter is used for the derivation.

V_1	V_2	P	N_{phase}	min-max f_s
300-900V	300-900V	10kW	2	20-400kHz

TABLE 2: FSBBC specifications

2.2.1 Deriving the proposed modulation

In this section, the proposed modulation strategy is derived. To do this the following assumptions are made:

- Switching instances are ideal, i.e. instant and lossless.
- The inductance, and in- and output voltages are constant.
- Power transfers from side 1 to side 2, i.e. $I_{in} \geq 0$.

The four switches of FSBBC allow for a wide variety of possible modulation strategies. To narrow down the options of potential modulation strategies, the following criteria are set:

- Based on [23, 29, 30], S_2 and S_4 should not be conducting simultaneously to reduce the RMS current values.
- Additionally, all turn-on instances of all switches should be 'soft', either zero-voltage or zero-current.
- The converter should be able to operate in the specified voltage and power range in Table 2.

A generic representation of the only modulation strategy that fulfils all these requirements is shown in Fig. 6. However, this strategy still has several degrees of freedom that need to be optimized, as will be discussed in the remainder of this section.

First, the volt-second balance is calculated to get the voltage transfer ratio. It turns out that the voltage transfer ratio V_{gain} is independent of the phase-shift between the half-bridges δ , and for $I_1 \geq 0$ equals:

$$V_{gain} = \frac{V_2}{V_1} = \frac{D_1}{1 - D_4}, \quad \text{with, } 0 \leq D_4 \leq D_1 - \delta \quad (1)$$

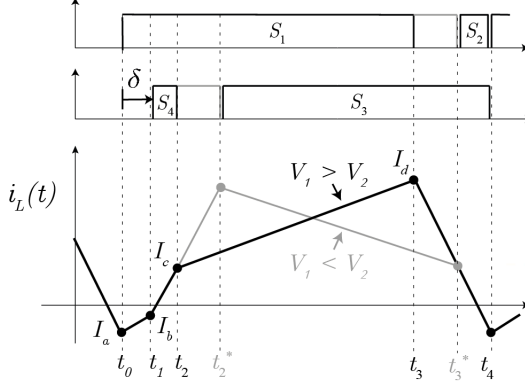


FIGURE 6: Gate signals and inductor current waveforms of the investigated variable-frequency modulation scheme.

Eq. (1) shows that multiple solutions exist for the same voltage gain $\frac{V_2}{V_1}$. Additionally, V_{gain} is independent from δ and I_0 and these are therefore additional degrees of freedom. The resulting $D_1 - D_4$ solution space for a fixed output voltage of 600V is shown in Fig. 7(a). Next, the values of the four currents $I_0 - I_3$, as shown in Fig. 6, can be calculated according to Eq.(2)-(5), with inductor voltage V_L , current flank period D_n and frequency $\frac{1}{T_s}$.

$$I_1 = I_0 + \frac{(V_1 - V_2)\delta T_s}{L} \quad (2)$$

$$I_2 = I_1 + \frac{V_1 D_4 T_s}{L} \quad (3)$$

$$I_3 = I_2 + \frac{(V_1 - V_2)(D_1 - \delta)T_s}{L} \quad (4)$$

$$I_4 = I_3 + \frac{-V_2(1 - D_1)T_s}{L} \quad (5)$$

For achieving ZVS or ZCS turn-on of S_1 and S_4 at t_1 it is required that $I_1 \leq 0$. As a result, any increase in δ requires a further decrease of I_0 to still achieve quasi-resonant operation. Since I_0 should be minimized to minimize i_L^{RMS} , and δ does not affect voltage gain, it is set to zero.

This leaves D_1 , D_4 and I_0 as free variables in the design. Now, based on Eq. (2)-(5), and using the general RMS of a waveform $i(t)$ and rewriting it to a piecewise linear form, with segment lengths D_k and current values I_k according to Eq.(6), I_L^{rms} can be calculated according to Eq. (7).

$$I_{rms} = \sqrt{\frac{1}{T} \int_0^T i^2(t) dt} = \sqrt{\sum_{n=1}^k D_n i_k} \quad (6)$$

$$I_L^{rms} = \frac{1}{\sqrt{3}} \sqrt{\sum_{n=1}^4 D_n (I_n^2 + I_n I_{n-1} + I_{n-1}^2)} \quad (7)$$

Next, to calculate $f_s = 1/T_s$, Eq.(9) is derived by solving Eq.(8) for T_s , using current segments $I_0 - I_4$ written as functions of time. Eq.(8), describes the input power based on inductor current [22].

$$P_1 = \frac{V_1}{T_s} \sum \left(\int_0^{D_4 T_s} i_1(t) dt + \int_{D_4 T_s}^{D_1 T_s} (I_1 + i_2(t)) dt \right) \quad (8)$$

$$T_s = \frac{2LP}{V_1(V_1(D_1^3 + 3X + 2D_1 D_4 - 2D_4^2) - V_2(D_1^3 + 3Y + D_4^3))} \quad (9)$$

with,

$$X = D_1 D_4^2 - D_1^2 D_4 \quad \& \quad Y = D_1^2 D_4 - D_1 D_4^2 \quad (10)$$

To choose the values of D_1, D_4 Eq.'s (7) and (9) are plotted in Fig. 7(a)-(c) for $P = 5\text{kW}$ and $L = 100\mu\text{H}$, with I_0 set to zero. Note that the value of I_0 can be considered as a near constant offset to the contour plot of i_L^{rms} , hence D_1, D_4 can be determined independently of I_0 . Fig. 7(c) shows that for most voltage gains, f_s can be minimized by choosing the maximum allowable value for D_1 .

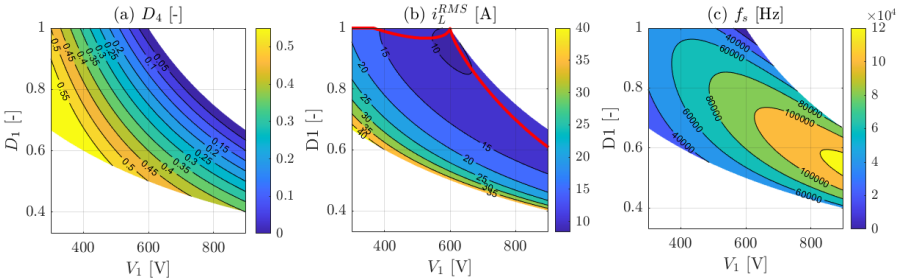


FIGURE 7: Solution spaces of: (a) Eq (1), (b) Eq. (7), and (c) Eq.(9). The solution is displayed for $V_2 = 600\text{V}$, $P_1 = 5\text{kW}$ single phase converter (or 10kW 2-phase) with an $100\mu\text{H}$ inductor. The minimum RMS value is indicated by the red line in (b).

However, the minimum value of I_L^{rms} for any voltage gain is obtained by slightly increasing D_4 from its minimum value. A trade-off therefore exists between minimizing conduction losses at the cost of increasing switching frequency¹, and corresponding frequency-dependent losses, such as core- and switching-losses. Therefore, Fig. 8 shows the variation of losses over the solution space, as calculated according to Appendix B. From Fig. 8 it is concluded that the effect of increasing f_s , by increasing D_4 , has a much more drastic effect on the losses than the slight decrease in RMS currents. Therefore, the total losses can be minimized by minimizing D_4 , which coincides with triangular BCM or TCM.

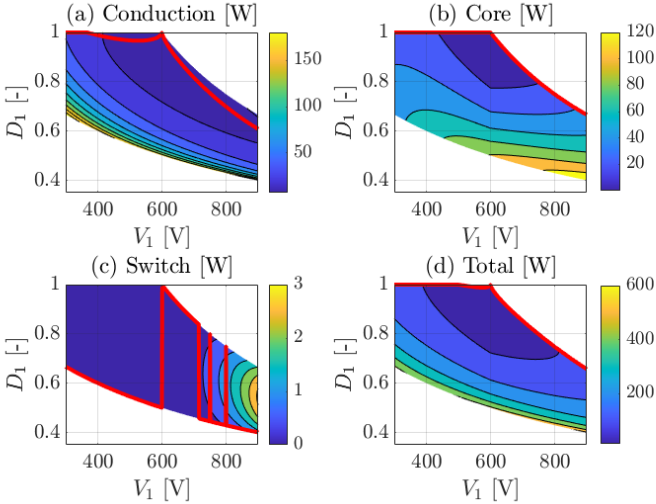


FIGURE 8: Surface plot of (a): Conduction loss, (b): Core loss, (c): Switching loss, and (d): Total loss at 5kW. The red line indicates the minima.

Finally, the last remaining degree of freedom in the modulation is the choice of I_0 . Obviously, I_0 should be minimized to reduce RMS currents. However, for the conditions² specified in Eq.(11) A negative value of $I_0 = I_{zvs}$ is required to achieve full ZVS [33].

$$1 \leq V_{gain} \leq 2 \quad \& \quad V_{gain} \leq \frac{1}{2} \quad (11)$$

- 1 Using $71\mu\text{m}$ litz-wire, combined with a maximum switching frequency of 400kHz, the skin-effect can be neglected in this analysis.
- 2 These conditions apply in case of triangular QR-BCM or TCM. Different conditions apply to the trapezoidal current shape of Fig.7, as seen in Fig. 8(c)

To analyze the effect of I_0 on efficiency, the total losses for both BCM and TCM are shown in Fig. 9. Here, the minimum required value of I_{zvs} in boost mode can be calculated according to Eq.(12) [33].

$$I_{zvs} = \sqrt{\frac{C_r V_2 (2V_1 - V_2)}{L}} \quad (12)$$

Here C_r is the combined capacitance of one half-bridge ($C_r = 2C_{ds}$). At an output voltage of 600V and an input voltage range of 300-900V, I_{zvs} ranges from 0-1.7A. Based on Fig. 9, it is concluded that the increased conduction and core losses of TCM outweigh the capacitive switching losses under QR-BCM (ZCS). Naturally, the switching losses will increase when the switching frequency increases under partial load. However, the effect of I_{zvs} with TCM relatively also increases under partial load. In terms of complexity, QR-BCM is significantly easier to control and more robust as it does not require any high-frequency current measurements or additional circuitry to ensure full ZVS under any given operating condition. Therefore QR-BCM is the preferred modulation strategy.

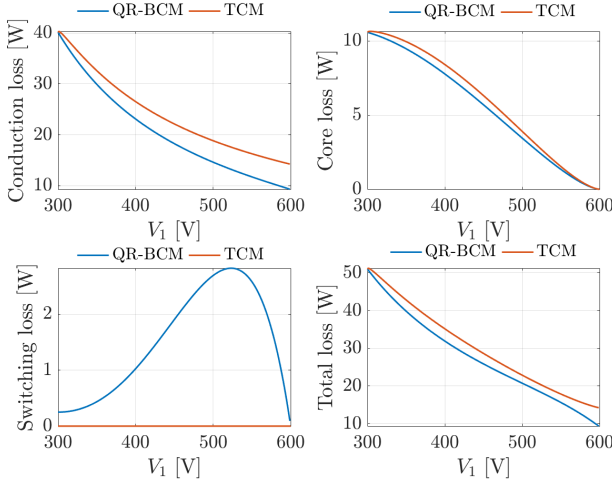


FIGURE 9: Comparison of losses under triangular QR-BCM and TCM modulation, for $V_2 = 600\text{V}$ and $300 \leq V_1 \leq 600$, so that $1 \leq V_{gain} \leq 2$. Outside this region QR-BCM and TCM are equal, i.e. $I_{zvs} = 0$. $35\text{m}\Omega$ switches are assumed.

To conclude this section, losses can be minimized by choosing the minimum value of D_4 for any voltage gain, resulting in conventional buck- and boost-operation with either S_1 or S_3 always on. Next, QR-BCM is preferred over TCM in terms of efficiency and complexity. However, both QR-BCM and TCM introduce a problem for voltage gains close to one as the switching frequency will approach zero, as shown in Fig. 7(c) and 10. The next section discusses how this discontinuity is overcome with the proposed modulation scheme.

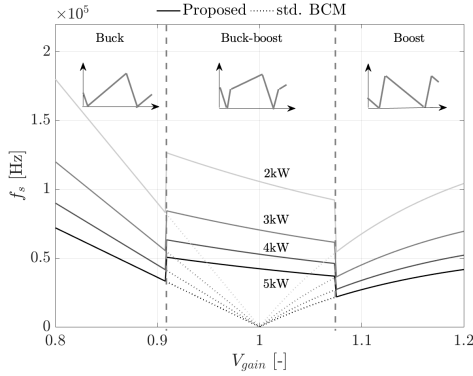


FIGURE 10: switching frequency when operating in QR-BCM, proposed vs standard (no transition).

2.2.2 Proposed buck-boost modulation

Since f_s is inversely proportional to the output power, a power control discontinuity for $V_{gain} = 1$ exists for QR-BCM operation. Additionally, the operation of the converter is constrained by minimum and maximum on-time limitations of the microcontroller, and audible switching frequencies are preferably avoided. To overcome this issue, a buck-boost transition region is introduced where D_1 is slightly decreased, and D_4 is increased accordingly. After including 3% hysteresis, the linear curve drawn between the two outer limitations of the duty cycle ($D_1^{max} = 0.98$ and $D_4^{min} = 0.03$) is used to determine the desired D_4 in the transition region, while staying close to the theoretical optimal operation. The resulting duty cycles and switching frequency are shown in Fig. 11 and 10, respectively. The increase in D_4 changes the current shape in buck-boost mode to a trapezoidal current, as shown in Fig. 10. Due to the hysteresis and duty cycle constraints, it

is impossible to have a continuous gradient of switching frequency over the entire voltage range. Even though the change in D_4 is minimal, the resulting jump in frequency is still very significant. For example, an increase in f_s of 80% is required when transitioning from boost to buck-boost at full power, as shown in Fig. 10. Therefore, additional measures must be taken to prevent overcurrents or large output power swings. The next section discusses the implementation of the proposed control scheme and the techniques used to achieve these smooth mode transitions.

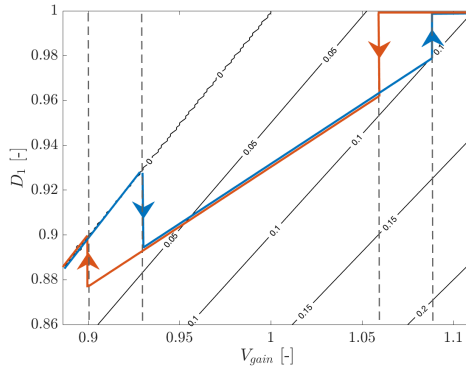


FIGURE 11: Course of duty cycles D_1 and D_4 (surface), near the transition region, including hysteresis.

2.3 IMPLEMENTATION & CONTROL

The switching frequency discontinuity, shown in Fig. 10 causes a discontinuity in power control and, additionally, it can trip the over-current protection. This section discusses the measures implemented to provide smooth and fast mode transitions. To do this, first, the general implementation of the digital control for 2-phase interleaved QR-BCM is discussed, after which the mode transitions are explained.

2.3.1 Digital Control for Interleaved QR-BCM

The proposed 10kW FSBBC operates in three distinct modes and utilizes two interleaved phases to increase the efficiency and power density, by power sharing and ripple cancellation, respectively. Buck operation will be discussed as an example. However, the operation is similar in all three

modes. The fundamental waveforms for the converter in buck mode are shown in Fig. 12.

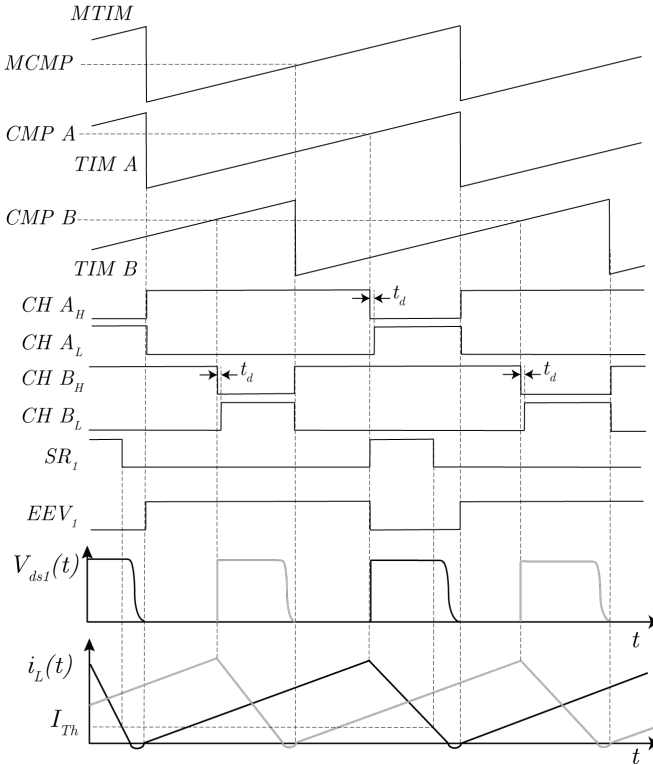


FIGURE 12: Key waveforms for a 2-phase interleaved FSBBC in buck mode. The always-on switches/timers are not shown.

Depending on the operating mode, a different switch operates as the master switch, e.g. S_1 of phase 1 in buck mode (and S_4 for boost mode). The switch node voltage (ZVD_x in Fig. 4) of this master switch is measured using the capacitive divider circuit shown in Fig. 13. By delaying the measured flank of ZVD_x , the edge of the external event EEV_x can be synced to half the $L-C_{ds}$ resonance period (T_{res}) of each half-bridge. The resulting rising- or falling-edge of the EEV_x then triggers a reset of the master switch pulse-width-modulation (PWM) timer (TIMA) and the master timer (MTIM), starting a new cycle when the drain source voltage is at its minimum. To ensure correct timing, a 470pF capacitance is placed in

parallel to the FET. Additionally, the parasitic C_{ds} flattens out above the minimum voltage of 300V, and hence the total parallel capacitance can be considered constant. Under full ZVS conditions body diode conduction will ensure ZVS before $\frac{1}{2}T_{res}$ has been reached.

The EEV is also used to update the master compare (MCMP) registers, which holds the required phase shift of all three slave timers (half-bridges) with respect to the master timers, e.g. the phase shift between TIMA and TIMB in Fig. 12. Using the EEV, the phase shift is updated every PWM cycle, independently from the control loop using an interrupt request (IRQ)³. As a result, the phases are always shifted by 120 degrees and perfect interleaving is ensured. Depending on the operating mode, and corresponding active master switch, either the falling- or rising-edge of the EEV is used.

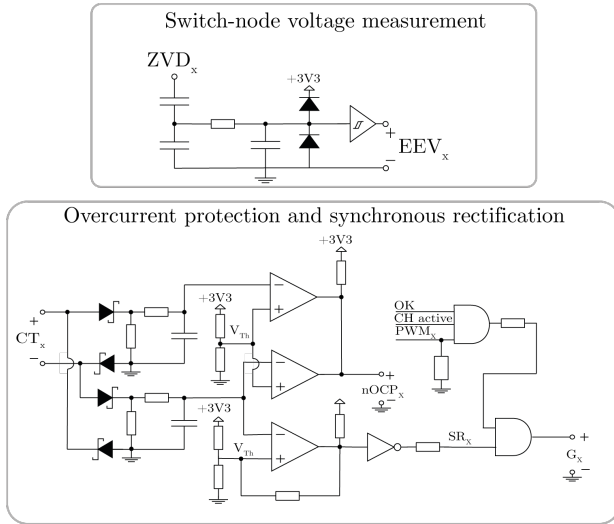


FIGURE 13: Control circuitry for drain-source voltage valley detection, synchronous rectification, and overcurrent protection.

Next, the overcurrent protection and synchronous rectification (SR) circuits for each switch, are shown in Fig. 13. Here CT corresponds to the secondary side of the current transformers placed on the drain or source of each FET, as shown in Fig. 4. Since the converter operates in QR-BCM, the control can be simplified by turning off the synchronous switch just before

³ An IRQ is a signal that temporarily stops the running program to execute a special program or function; an interrupt handler

the current drops to zero. This is done using the hysteresis comparator shown in Fig. 13 with threshold V_{th} (and current threshold I_{th}) and results in the SR_x signal. The SR_x signal, together with the PWM signal from the microcontroller, the channel activation signal CH_{active} , and general OK signal OK , are then used to determine the gate voltage G_x , as shown in Fig. 13. Finally, all PWM registers operate in pre-load mode and therefore are only updated when the accompanied timers are reset at every EEV. This allows the control loop to run at a fixed 25kHz rate, and decouple it from the PWM frequency. In the next section, the feed-forward mode transitions are described.

2.3.2 Feed-forward Mode Transitions

To operate continuously in the entire voltage region, mode transition mechanisms have been implemented. To prevent overshoots, the mode transitions of each phase need to be executed when the inductor current of that phase equals zero. This is achieved using IRQ handlers triggered by the corresponding EEV of each phase whenever the voltage thresholds of the operating mode are exceeded. Depending on the required operating mode, every transition is slightly different. However, the general procedure consisting of actions A1 to A6 is the same and is discussed in this section. The corresponding EEV will trigger the mode transition interrupt of each phase. An exemplary buck to buck-boost transition is shown in Fig. 14.

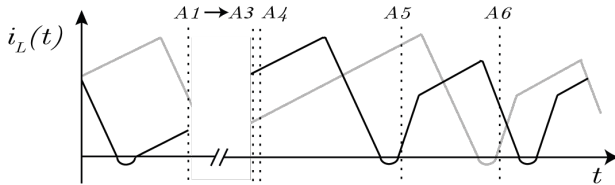


FIGURE 14: Buck to buck-boost mode transition. All actions A1-A6 are indicated. During actions A1-A3 several periods might have past.

- A1: The existing operating mode voltage threshold is exceeded and the transition procedure is initiated.
- A2: Next, the switching period and on-times of the first cycles in the next operating mode are calculated. The on-time of the switches is calculated according to Eq.(9) and Fig. 11. During boost operation $D_1 = 1$, and during buck operation $D_3 = 1$

- A3: The controller output, gain, and its internal variables are fed forward based on the calculations of action A2. Actions A1-A3 might take several switching periods depending on the switching frequency, as indicated by the broken x-axis in Fig. 14. In this time, a control update might be due. Therefore, a control update exception is activated to prevent register updates based on outdated information.
- A4: After A1-A3, the IRQ handler is fully initialized, therefore any previous IRQ flags are cleared and the IRQ of the master phase is enabled. This will start the IRQ handler at the next EEV.
- A5: At the next EEV, the IRQ handler is executed. Inside the IRQ handler the following actions are taken:
1. The IRQ handler is disabled, preventing future EEVs from triggering an interrupt.
 2. The corresponding PWM channel of the next master switch is activated with " CH_{active} " in Fig. 13.
 3. The pre-load registers of the PWM timers and phase-shift are updated based on the calculated values (T_{bo} , T_{bb} , and T_{bu}).
 4. the PWM timers (TIM A-D), phase shift controller (MCMP), the EEV, and the EEV sensitivity are reconfigured for the next operating mode.
 5. The corresponding timers are reset, which updates the PWM timer registers based on the pre-load registers. Additionally, the set/reset configuration of the timers is updated, corresponding to the required operating mode.
 6. The phase 2 IRQ is enabled. By nesting the IRQ handler, it is ensured that the master phase IRQ is executed first.
- A6: The EEV of the second phase initiates its IRQ handler, following a similar procedure as the master phase (A5).

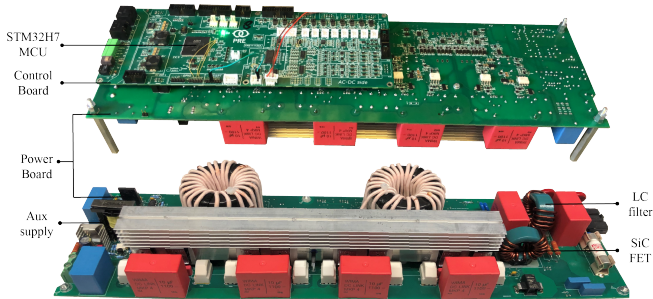


FIGURE 15: Top and bottom side of the 10kW interleaved cascaded buck-boost converter. The converter is 48cm long and 13cm wide.

2.4 EXPERIMENTAL VERIFICATION

The proposed modulation and closed-loop control scheme of the interleaved FSBBC are implemented on the 10kW prototype shown in Fig. 15. Fig. 16(a)-(c) show the three different operating modes, switching with full ZVS (under the measured conditions, full ZVS can be achieved with QR-BCM). Additionally, two example closed-loop mode-transitions at 10kW are shown in Fig. 16(d)-(e). Finally, Fig. 16(f) shows how the control can maintain a constant output current while traversing all three operating modes under a 200V output voltage step. The results demonstrate how each phase can transition smoothly and separately, with an instantaneous change in switching frequency while preserving output power. By triggering the transition using the EEV, large current spikes are prevented, and each interleaved phase can transition at its own inductor current zero-crossing. Additionally, the feed-forward mode transitions take care of the power control discontinuity as they facilitate the discontinuous step in switching frequency. Note that the current amplitude in buck-boost mode is lower for the same output power due to the trapezoidal current shape.

Next, all efficiencies are measured with a Yokogawa WT500 power analyzer with 0.1% specified power accuracy. The achieved efficiency is shown in Fig. 17. The buck-boost region shows the lowest efficiency due to the higher switching frequency and RMS currents. These results confirm the conclusion from section II.A that the highest efficiency can be achieved for minimal on-time of S_4 for a given voltage gain. The high overall efficiency and peak efficiency (99.5% at full power, 99.6% at partial load) of the prototype match the highest peak efficiency in the literature for the FSBBC [27, 31], despite significantly larger power per phase and input voltage range, as

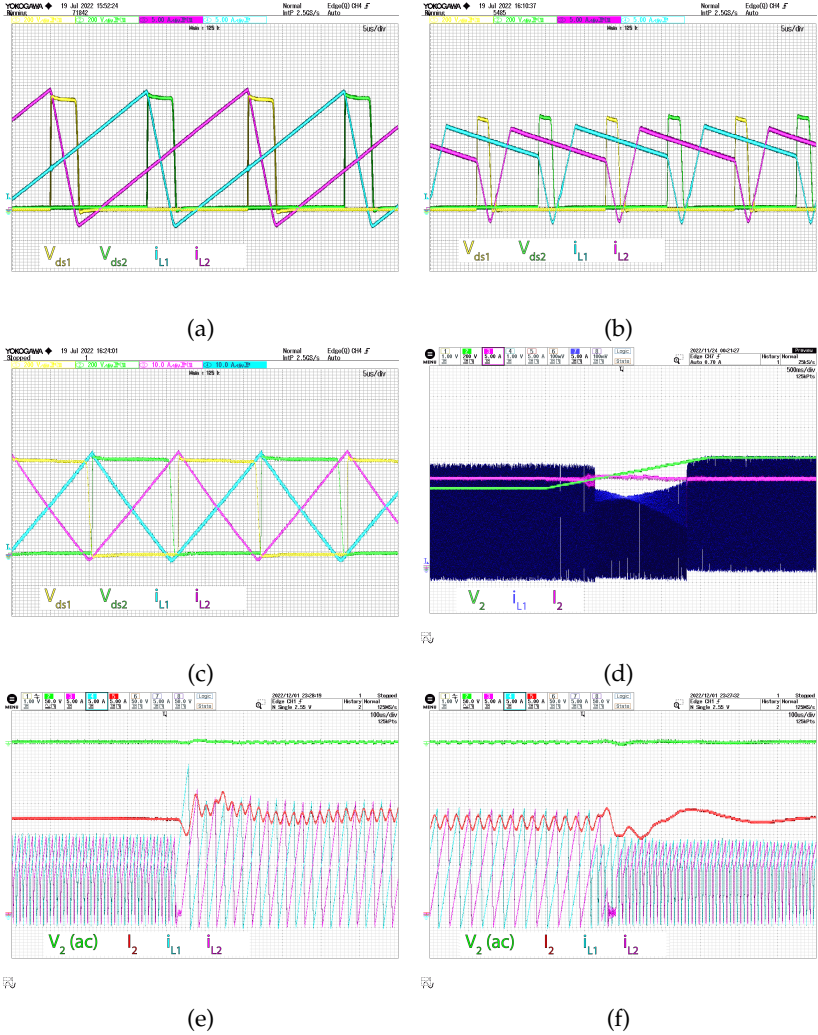


FIGURE 16: (a)-(c):Inductor currents and drain-source voltages at 10kW, $V_o = 600V$. (a): buck $V_i = 700V$, (b): buck-boost $V_i = 550V$, (c): boost $V_i = 300V$. (d)-(f): Closed-loop mode transitions at 10kW $V_o = 600V$. (d): buck-boost to buck mode, (e): boost to buck-boost, (f): buck to buck-boost. Here $V_{ds,x}$ denotes the drain-source voltage of switch x , and i_{Lx} the inductor current of phase x , and V_2 , i_2 denote side 2 voltage and current, respectively.

shown in Table 7. Additionally, these studies do not present a way to control their converters in a closed loop. The following section will compare two other closed-loop FSBBC modulation schemes, presented in [25] and [28].

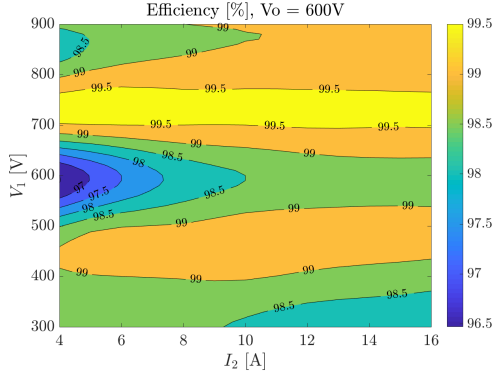


FIGURE 17: Interpolated efficiency measurements of the proposed modulation over its operating range.

Parameter	proposed	[27]	[31]
V_1	300-900V	300-500V	400V
V_2	300-900V	200-600V	100-500V
Maximum power	10kW	3kW	3kW
η_{pk} @ max P	99.5%	99.5%	99.5%

TABLE 3: Prototype specifications compared to existing studies.

	proposed	B-QR-BCM	QCM
Inductance	100 μ H	275 μ H	35 μ H
Core	077614A7	0077615A7	0077614A7
Litz wire	1000x0.071	1000x0.071	1000x0.071
FET	UF3C120040K4S	UF3C120040K4S	UF3C120040K4S
Capacitor	WIMA MKP-4	WIMA MKP-4	WIMA MKP-4

TABLE 4: Components used for the converter design and comparison.

2.4.1 FSBBC Modulation Comparison

To further examine the effectiveness of the proposed control, a comparison based on efficiency and power density is done with three other modulation schemes: QCM, B-QR-BCM and TCM. To begin, Fig.18 shows that the difference in efficiency between the proposed QR-BCM and TCM is negligible. At full power, QR-BCM performs slightly better, whereas at partial power, TCM performs marginally better. However, in both cases, the difference is negligible. This is a significant conclusion since most studies in the literature always strive for full ZVS switching, even though the efficiency improvement compared to ZCS is negligible. And, importantly, ZCS QR-BCM is significantly easier to implement since it does not require high-frequency current measurement or any ZVS tracking circuitry. The remainder of this section will be focused on the comparison with the QCM modulation presented in [28], and B-QR-BCM.

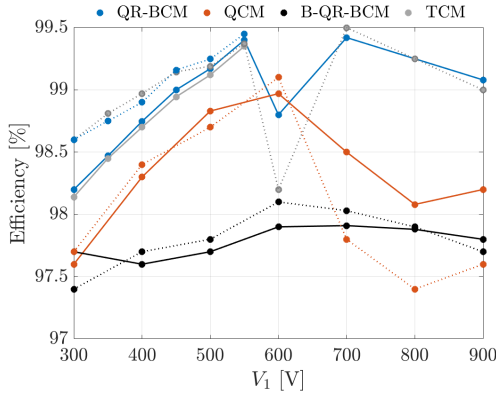


FIGURE 18: Efficiency comparison of QR-BCM, QCM, B-QR-BCM, and TCM.

The modulation proposed in [28] provides a simplified QCM approach which allows to minimize the inductor RMS current while still having only one control variable. Secondly, B-QR-BCM is implemented. The main advantage of B-QR-BCM is that it only requires one operating mode for any voltage gain. All modulation schemes in this comparison can operate continuously over the entire voltage range and are controlled by a single control variable and therefore do not require look-up tables of any sort. The experimental waveforms under identical conditions are shown in Fig. 19(a)-(c). The same single-phase prototype is used for all three schemes, apart from the inductor, which is optimized for every scheme. The inductance

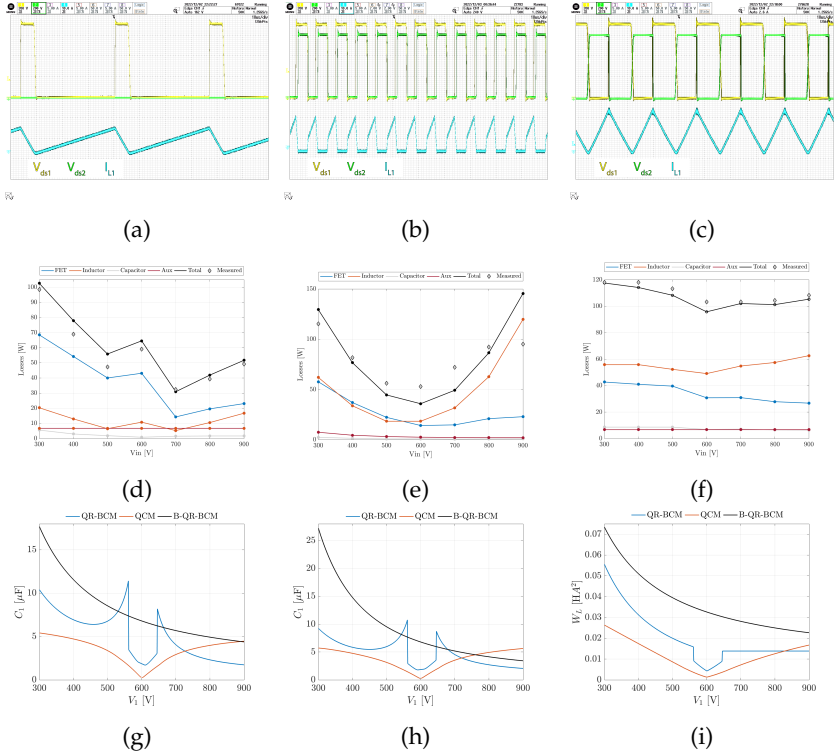


FIGURE 19: (a): The proposed modulation (buck mode), (b): QCM modulation, (c) B-QR-BCM modulation, all measured at 50% partial load with 700V input voltage and 600V output voltage. (d)-(f): Loss distribution based on measured quantities for the proposed control (QR-BCM), B-QR-BCM and QCM, respectively. (g)-(i): Passive component sizes (in- and output capacitor and inductor), for all three modulations. Here $V_{ds,x}$ denotes the drain-source voltage of switch x , and $I_{L,x}$ the inductor current of phase x .

values and components used for each scheme are given in Table 4. For B-QR-BCM higher permeability cores were used to achieve the higher inductance value. The achieved efficiencies for full power and 50% partial power are shown in Fig. 18, and the calculated losses are shown in Fig. 19(d)-(f). The calculations are done according to Appendix B. Additionally, the potential power density for each modulation is estimated based on the

passive component sizes, calculated according to Appendix C. The findings of the comparison are summarised in Table 5.

2.4.1.1 Efficiency

Overall, the proposed modulation shows the highest efficiency for most voltage gains. This is achieved due to the low RMS current combined with significantly lower switching frequency (at maximum power), as shown in Fig. 20(a)-(c). Only for voltage gains close to 1 the QCM modulation performs slightly better. The reason for this is twofold. Firstly, the QCM modulation appears to be operating at its best for voltage gains close to one. For $V_{gain} = 1$, $T_x = 0$, and almost the entire period is used for power transfer. Additionally, the buck-boost mode for QR-BCM operation is less efficient due to the trapezoidal current shape, resulting in higher frequency and RMS current than buck- or boost operation. The effect of T_x on QCM efficiency is visible from Fig. 20(a)-(d): for voltage gains diverging from one, T_x increases which results in higher peak- and RMS currents, especially at high voltages. Fig. 19(e) shows that the core losses are most affected by this, as the high peak currents and high switching frequency result in a very high equivalent frequency (f_{eq} in Eq. 112). Physically, this is due to high magnetizing losses resulting from high $\frac{dB}{dt}$ in the magnetic core. The effect on conduction losses is less significant due to the short duration of the peak currents. This is an inherent limitation of the constant frequency behaviour of QCM. Note that lowering f_s does not solve this, as it would again increase T_x . Another 'disadvantage' of the QCM modulation scheme is the negative current offset I_{zvs} to achieve full ZVS, which as shown above does not necessarily outweigh the capacitive switching losses under ZCS. Regarding B-QR-BCM, its efficiency is compromised by a very high inductor current which is inherent to the switching pattern of B-QR-BCM. For example, in an ideal scenario, the peak inductor current of a QR-BCM boost converter is twice the input current, i.e. $\max(I_L) = 2I_1$. However, using B-QR-BCM the peak inductor current is equal to $\max(I_L) = 2I_1/D_1$. The full input power needs to be delivered in a relatively shorter part of the switching period, resulting in higher peak currents and resulting RMS currents. This naturally results in increased losses, especially due to the already higher inductance value.

2.4.1.2 Power Density

From Fig. 19(g)-(i) it is concluded that in terms of power density, the QCM modulation requires the lowest passive component volume. Assuming that

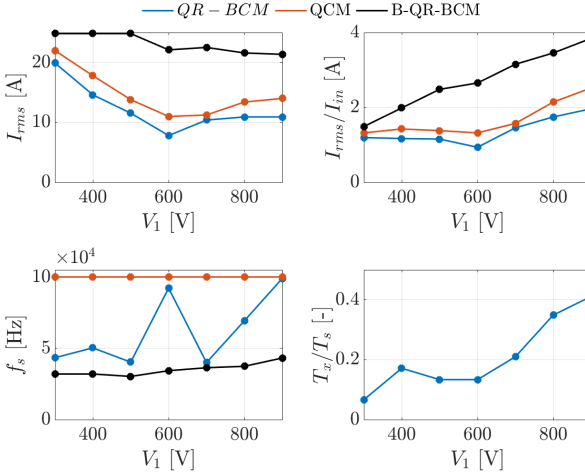


FIGURE 20: Measured variation of the following variables for each modulation scheme: (a) RMS currents, (b) ratio of RMS- to input current, (c) switching frequency. Additionally, (d) shows the ratio of T_x/T_s with QCM. All were measured at 5kW output power with varying input voltage.

the inductor can be scaled based on the work W_L done and not its power dissipation. The proposed modulation requires slightly larger capacitances and inductors since its switching frequency is lower at maximum power. The B-QR-BCM requires the largest passive components, as both in- and output capacitors must carry the full in- and output current for substantial parts of the switching period. Additionally, a higher inductance is required compared to QR-BCM and QCM, resulting in more work done by the inductor. Since the maximum FET losses are similar, all modulation can utilize similar heatsinks.

2.4.1.3 Complexity

At the cost of reduced efficiency and power density, the B-QR-BCM scheme is the easiest to implement and control. Despite variable frequency behaviour, it does not require mode transitions and does not have an imperative requirement on high-frequency current measurements. Next, the proposed QR-BCM scheme is slightly more complicated as it requires mode transitions but is very simple in hardware design. Finally, the reviewed

QCM scheme requires mode transitions to transition between CCM and DCM mode and is dependent on multiple high-frequency current measurements with both positive and negative thresholds.

	Proposed	QCM	B-QR-BCM
Efficiency	++	+	-
Density	+	+	-
Complexity	+	-	++

TABLE 5: Summary of modulation comparison results

2.5 CHAPTER CONCLUSION

In this chapter a three mode variable-frequency modulation for the FSBBC is proposed. Based on a loss analysis it was concluded that QR-BCM synchronous buck and boost operation is the most efficient modulation. More specifically, QR-BCM operation is preferred over TCM both in terms of losses and in terms of complexity.

To overcome the problem of power control discontinuity for voltage gains close to unity, a new buck-boost mode was proposed. Additionally, a smooth mode transition technique based on the digital, interleaved QR-BCM implementation was proposed to provide smooth and continuous power control over the entire voltage range. The experimental results show that the proposed closed-loop QR-BCM control scheme for the FSBBC, solves the problem of power control discontinuity under multi-mode, variable frequency, operation. Additionally, it is applicable for both single- and multi-phase converters, as shown using the developed two-phase 10kW experimental prototype. Additionally, with 99.5% peak efficiency, the measured efficiency equals the highest in literature, despite a larger power- and voltage-operating range and based on a significantly simpler modulation scheme. This, in turn, is made possible by the ability to transition between different operating modes and optimize the modulation based on the voltage gain.

Finally, a comparison with a QCM and B-QR-BCM modulation scheme has been performed. It is concluded that the proposed modulation scheme shows the highest overall efficiency, especially for wide-voltage-range applications, with limited- to no compromise in power density and complexity.

This chapter discusses the hardware and control loop design of the DC-integrated multi-port converter. First, the different topologies of multi-port converters are discussed and the best-suited multi-port converter topology is chosen based on survey of related studies. After that, it summarizes the design of the corresponding converter. Finally, the design of the closed loop control and protective measures are discussed.

This chapter is based on:

- J₁ W. Vermeer, M. Wolleswinkel, J. Schijfelen, G.R. Chandra Mouli, P. Bauer, *Design of a 10kW Multi-Port EV Smart Charging System Integrating EV, PV, and Battery*, 2023, (under review for) *IEEE Transactions on Transportation Electrification*

3.1 INTRODUCTION

The previous chapter discussed the design of the converter used for the PV and BES ports. In this chapter this converter will be integrated with the EV charger, and the multi-port converter control loop will be discussed.

To fully utilize the flexibility in the multi-port converter, it should be designed for multi-directional power flows. This includes bidirectional EV charging, also known as vehicle-to-X (V2X), such that both the EV and BES can act as renewable energy storage. Additionally, the converter should be designed to achieve a high efficiency and power density.

The goal of this chapter is to determine the best suited multi-port converter topology, and discuss the hardware and control loop design of the DC-integrated multi-port converter.

3.2 RELATED WORK

First, the related literature is reviewed to find the best suited multi-port topology and identify the contribution of this chapter. An overview of studies integrating EV, PV, and BES is shown in Table 12, which summarizes which ports are included, the multi-port converter topology, the DC-AC converter topology (single-phase or three-phase (ϕ)), the maximum charging voltage of the EV, whether the converter provides galvanic isolation (iso.), and whether they authors have included experimental results (exp.). Based on Table 12. three different methods for integrating the different ports can be distinguished:

- 50Hz AC grid integration
- High-frequency transformer integration
- DC integration

A schematic representation of these three methods is shown in Fig. 21. The next subsections discuss the related studies of all three methods in more detail.

3.2.1 AC integration

The most conventional solution is integration using the AC grid [34]. However, this requires several DC/AC conversion steps, resulting in reduced power density, reduced efficiency, and increased cost. Additionally, it is more difficult to implement integrated control such as smart charging. For this reason, this option is not investigated in detail. Several studies improve

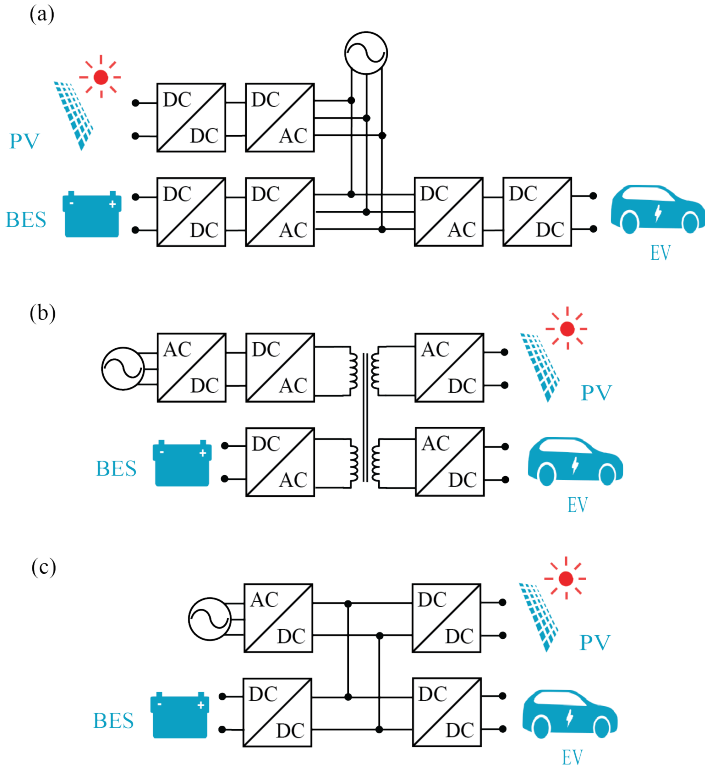


FIGURE 21: Different methods of integrating EV, PV, and BES. (a): 50Hz AC grid integration (b): high-frequency transformer integration, and (c): DC integrated solution.

upon this by integrating EV, PV and BES (or any combination of these) into one multi-port system.

3.2.2 High-frequency transformer integration

In [35–39], high-frequency, multi-winding, transformers are used in combination with multiple active bridges (MAB) to integrate the different ports. The advantage of these MAB converters is that ZVS can be achieved in a large part of the operating region, and they are well suited for high voltage-gain conversions and applications requiring isolation. However, the multi-winding transformers are limited in their maximum power capability, have complex coupled control loops, and due to their multiple

windings, are prone to high-frequency magnetic losses like the proximity effect, resulting in relatively low average DC-DC efficiencies (90 – 96%) [40]. Furthermore, galvanic isolation is only required for EV charging. Using a HFT based multi-port converter would lead to unnecessary isolation for the PV and BES ports, resulting in unnecessary additional complexity.

3.2.3 *DC integration*

Other studies focused on DC-integrated topologies, which allow for simpler decoupled designs. Additionally, it allows for modularity, where each ports' power rating can be easily increased and tailor-made for different smart charging applications. The disadvantage of the DC-integrated topology is that it requires more design effort to individually design each ports' converter. Based on the summary of DC-integrated multi-port converter studies shown in Table 12, the following conclusion can be drawn:

- Only four out of 17 DC-integrated topologies provide galvanic isolation with respect to the EV.
- Just seven out of 27 studies can charge batteries above or around 400V. As a result, combined with the galvanic isolation requirement, only 15% of the reviewed studies comply with modern EV charging standards.
- Only five out of 27 studies focus on three-phase systems and are therefore able to fast-charge and fully utilize the modular nature of the DC-integrated topology.
- Finally, despite integrating BES and bidirectional EV chargers, no study has focused on optimal power management, also known as smart charging. Multiple studies have shown that without proper power management, it is impossible to unlock the full potential of BES and vehicle-to-grid (V2G), making it cost-ineffective.

3.2.4 *Contribution*

Based on the literature review above, the main contribution of this chapter is the design of a multi-port converter that integrates 10kW PV, EV, and a BES, while connected to the AC grid. The designed converter is compliant with modern EV charging standards, such as galvanic isolation, voltage requirements, and EMC requirements. The design will be discussed in the next sections.

Study	EV	PV	Batt.	Topology	ϕ	V_{ch}^{max}	iso.	Exp.
[34]	12kW	3kW	3kW	AC	3	x	x	x
[35]	500W	500W	500W	HF-AC	x	200V	✓	✓
[36]	2kW	2kW	2kW	HF-AC	x	200V	✓	✓
[37]	50kW	50kW	50kW	HF-AC	x	96V	✓	x
[38]	x	60W	60W	HF-AC	1	28V	x	✓
[39]	1kW	x	1kW	HF-AC	3	400V	✓	✓
[41]	400W	250W	x	DC	x	12V	✓	✓
[42]	x	250W	200W	DC	x	48V	x	✓
[43]	1.92kVA	x	x	DC	1	105V	x	✓
[44]	1.44kVA	x	x	DC	1	400V	x	✓
[45]	5kW	5kW	x	DC	1	200V	x	✓
[46]	4kW	4kW	4kW	DC	1	360V	x	✓
[47]	5kW	5kW	x	DC	1	200V	x	x
[48]	4kW	4.8kW	x	DC	1	12V	x	✓
[49]	3.3kW	2.8kW	x	DC	1	400V	✓	✓
[50]	50W	50W	x	DC	1	9V	x	✓
[51]	3.3kW	3.3kW	3.3kW	DC	1	250V	x	✓
[52]	3.3kW	3.3kW	x	DC	1	240V	x	✓
[53]	3.6kW	x	x	DC	1	400V	x	✓
[54]	8kW	5kW	x	DC	1	400V	✓	x
[55]	600kW	20kW	x	DC	3	40V	x	x
[56]	8.4kW	3.7kW	x	DC	3	240V	x	✓
[57]	12.6kVA	5kW	12.6kVA	DC	3	400V	x	✓
[58]	10kW	10kW	x	DC	3	500V	✓	✓
prop.	10kW	10kW	10kW	DC	3	500V	✓	✓

TABLE 6: Related studies regarding the DC-integration of EV, PV, and BES. Acronyms: ϕ indicates a single- or three-phase system, V_{ch}^{max} indicates the maximum EV charging voltage, iso. indicates whether the converter provides galvanic isolation, Pwr. management indicates the power management strategy, finally Exp. indicates whether experimental results were included.

3.3 DESIGN OF THE MULTI-PORT CONVERTER

Based on the literature review presented above, the DC integrated multi-port topology is selected as it requires the least amount of conversion steps and allows for a modular design thanks to the decoupled control loops and scalability of the DC link. The modularity of the DC-integrated topology allows to customize the power ratings of each port (EV, PV, and BES), making it applicable to a wider range of applications, which can reduce the overall system cost.

The specifications of the system are given in Table 7. The rated power of each port is selected at 10kW as a balance between EV charging requirement and PV generation [7]. For powers above 10kW, more modules can be added. The EV port is designed to be compatible with CCS and ChaDeMo charging standards. Next, both the PV and BES ports are designed for a wide voltage range, ensuring that these are applicable for a wide range of configurations. Due to the similarity in PV and BES specifications, the same non-isolated DC-DC converter can be used for these ports. This again reduces the overall cost.

Parameter	Value
Nominal power	10kW
AC connection	400V, 50Hz, 16A
Total Harmonic Distortion	< 5%
Internal DC link voltage	750V
EV battery voltage	50-500V
EV current	-30A to 30A
EV voltage ripple	<500mV
EV current ripple	<1A RMS @ 10kW
BES battery voltage	300-900V
BES current	-33A to 33A
BES voltage ripple	<500mV
BES current ripple	<1A RMS @ 10kW
PV MPPT voltage	300-900V
PV current	-33A to 33A
PV voltage ripple	<500mV
PV current ripple	<1A RMS @ 10kW

TABLE 7: Specifications of the 10kW EV, PV, BES integrated charging system.

This thesis focuses on the design of the PV and BES converters, and continuous the existing work done in [59]. Therefore, the design of the DC-AC converter and EV port are only summarized here, and are based on [59].

3.3.1 DC-AC Converter

A standard three-phase two-level DC-AC converter, as shown in Fig. 22, is used for grid connection. The converter controls its grid current using

sinewave PWM at a switching frequency f_s of 47kHz. The main task of the DC-AC converter is to maintain the power balance on the DC link, by maintaining a DC link voltage of 750V. To ensure that all control loops can be decoupled, six 470 μ F electrolytic capacitors are used as energy buffers on the DC link (two in series, three in parallel). On the AC side, three LCL filters are used to filter out the harmonics of each phase. Since the operation and loss modelling of the DC-AC converter operated with sinewave PWM is well known, it is not explained in more detail in this chapter. More information on this topic can be found in [60, 61].

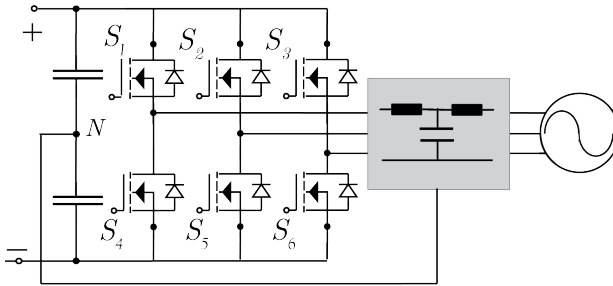


FIGURE 22: Power schematic of the two-level DC-AC converter.

3.3.2 EV Converter

The EV-port requires galvanic isolation, therefore, based on [62], the interleaved flyback (IFBC) topology is selected. Four interleaved phases are used, each utilizing a 2.5kW three-winding transformer, with two series-connected windings on the DC-link side. A schematic representation of the topology is shown in Fig. 28. On the EV side, two MOSFETs are placed in parallel to reduce the conduction losses.

To achieve a high-efficiency and power density, all power-semiconductors are made from Silicon-Carbide (SiC). Additionally, the IBFC is operated with quasi-resonant boundary conduction mode (QR-BCM). With QR-BCM operation, the converter operates at the boundary of continuous conduction mode and discontinuous conduction mode. The inductor current therefore always drops to zero ampere. After that, the LC resonance caused by the HFT leakage inductance and the parasitic drain-source capacitance C_{ds} of the FET, discharges C_{ds} until zero-voltage-switching (ZVS) or low-voltage-switching is achieved. Fig. 24 shows the QR-BCM operation principle. The resulting variable-frequency operation reduces, or completely eliminates,

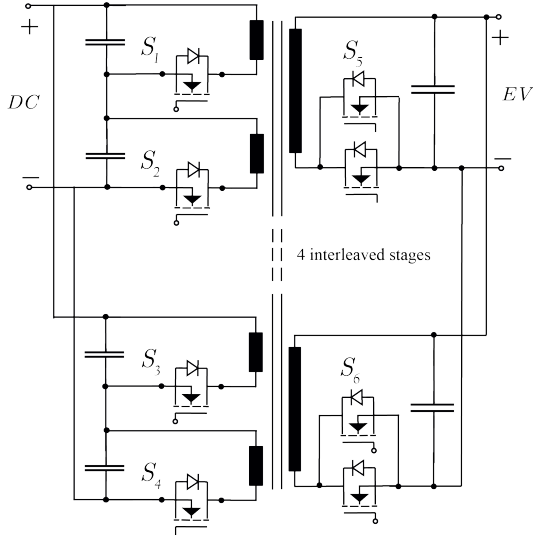


FIGURE 23: Power schematic of the interleaved flyback EV converter.

the switching losses and switching harmonics, resulting in improved efficiency and a lower electromagnetic interference (EMI).

During $0 \leq t \leq (D + D_1)T_s$ the MOSFETs S_x and S_y are conducting and the inductor current rises. After $t = DT_s$, the energy stored in the inductor is transferred to the secondary side, and the inductor current reduces to zero ampere. At $t = (D + D_1)T_s$, the inductor current has fallen to zero. At this time, the LC-resonance starts to exchange energy from the parallel capacitances of the FETs, $C_{32}, C_{33}, C_{35}, C_{36}$, to the primary inductance of the transformer. Once the voltage over the FETs has reduced to zero or its minimum resonance voltage, the FETs are turned on again at $t = T_s$. Depending on the ratio of V_{EV} and V_{DC} , either full zero-voltage switching (ZVS) or low voltage switching (LVS) with zero-current switching (ZCS) is achieved. The switching frequency ranges between 40kHz at maximum power and up to 350kHz for partial power. For even lower powers, valley skipping is implemented. The operation principle in V2x (discharging) is similar. Only then switches S_{31} and S_{38} are turned on first.

More details on the design and loss modelling of the IFBC with QR-BCM operation can be found in [58].

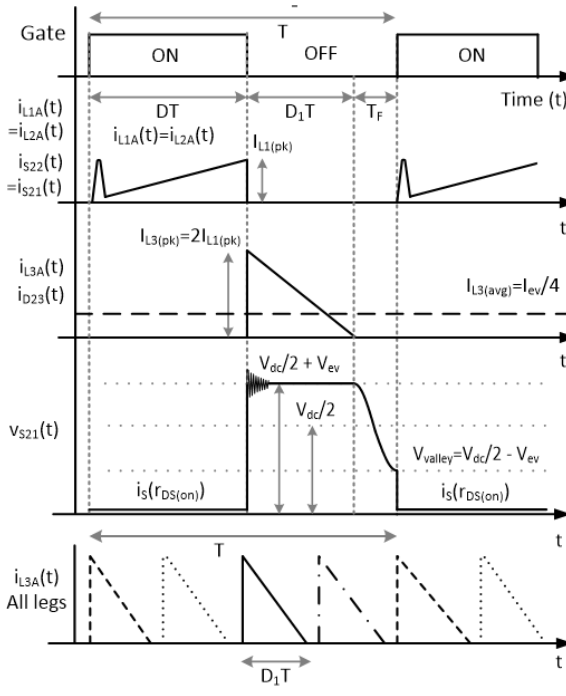


FIGURE 24: Waveforms for quasi-resonant operation for the interleaved flyback converter.

3.3.3 PV & BES converter

The specifications of the PV and BES ports are very similar. Both do not require galvanic isolation, the PV and BES voltages are equal, and their power rating is equal. Therefore, it is decided that the same DC-DC converter can be used for both the EV and BES. Since the output voltage ranges above and below the DC link voltage, a buck-boost topology is required. The four-switch buck-boost converter (FSBBC), shown in Fig. 4, is chosen because of its relatively low component count and non-inverting output voltage.

Naturally, the design of the FSBBC is dependent on the modulation of the switches. Since the FSBBC has a high degree of freedom in terms of switching modulation, it requires further investigation. In the next chapter a new modulation scheme for the FSBBC will be derived and its implementation will be discussed.

The full power schematic of the multi-port converter is shown in Fig. 25. It is comprised of the four-phase IFBC for the EV port, two two-phase interleaved FSBBC for the PV and BES port and the two-level DC-AC converter for the grid connection. The next section, will discuss the closed-loop control and protections of each port.

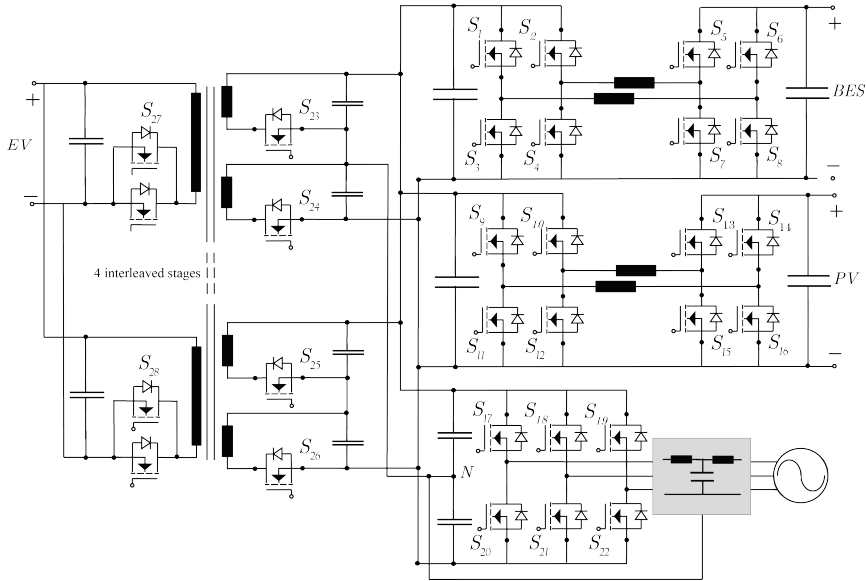


FIGURE 25: Power electronic hardware schematic of the multi-port converter

3.4 CLOSED LOOP CONTROL

Fig. 26 shows the V-I control loops of all converters. All DC/DC converters have multiple cascaded control loops in parallel for voltage- and current control. Only the minimum setpoint of each control loop is active at a time to ensure stability, as depicted by the common anode diodes.

3.4.1 DC/AC converter

As said above, the DC/AC converter maintains the power balance on the DC link. Thanks to the DC-integration, this can be easily done by controlling the DC-bus voltage. If the DC-bus voltage control is sufficiently fast to

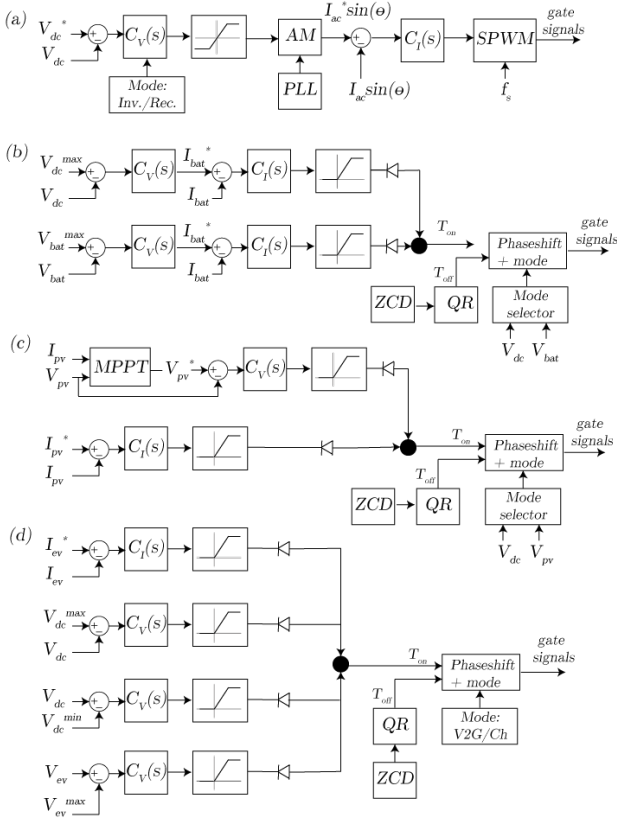


FIGURE 26: Here all four embedded V-I control loops for shown. Each port has its own control loops. (a): Stationary BES charger, (b): PV MPPT converter, (c): EV charger, and (d) DC/AC converter. The primary task of the BES and EV converter is to control their charging current, whereas the PV converter performs maximum power point tracking by controlling the PV panel voltage. Finally, the DC-AC converter maintains power balance by controlling the DC-link voltage. Besides their primary tasks, the DC-DC converters also include in- and output voltage control loops, cascaded with their primary loops. This allows the design to be designed modularly while maintaining power balance.

negate any disturbance from the DC/DC ports, all control loops can be decoupled, and the design can be considered modular. To ensure this, three parallel by two series $470\mu\text{F}$ 450V electrolytic capacitances are used as DC-

link energy buffers. The DC bus voltage is controlled to 750V by the grid current $I_{AC}\sin(\theta)$. Here a PLL is used to estimate the voltage phase angle and maintain a high power factor. In case of a power direction change, the control is reset at zero current to prevent overshoots on the DC link.

3.4.2 BES converter

For the BES port, two cascaded V-I control loops operate in parallel, one for battery voltage control and the other for DC bus voltage control, both used in cascade with the output current. The battery voltage control reduces the charging current when the maximum charging voltage is reached (CC-CV charging). The latter, DC bus voltage control, is used as a safety measure to curtail power in case of inverter overloading. This is required despite the RTC efforts to compensate the EV and BES setpoints based on forecasting errors due to its communication delays and limited resolution of two seconds. In this time, the intermittency of the PV can still overload the DC-link / DC-AC converter. If, in that case, the EV or BES power is not curtailed accordingly, an under or over-voltage will blow the converter components (either by exceeding the component voltage rating in case of over-voltage or by exceeding the thermal limitations in case of under-voltage). Since the EV and BES are both bidirectional, both under- and over-voltage control is required. As discussed above, this is a critical feature for a smart charging system, especially in case of no other inverter constraints, as the optimization will often use the full power of the inverter to utilize an advantage. To prevent controller interference between the DC/AC converter and the BES charger, the minimum and maximum DC-bus voltage setpoints of the BES charger are set to 730V and 770V, respectively, deviating 20V from the nominal voltage setpoint. As a last resort, all setpoints are reset to zero at voltages below 700V or above 800V to prevent a breakdown in case of failure.

The resulting setpoints control the on-time T_{on} of the switches. Next, the zero inductors current detection (ZCD) and QR-BCM detection circuits determine the off-time. Based on the resulting variable switching frequency, the phase shift block maintains the desired phase shift between the interleaved phases.

3.4.3 PV converter

The PV converter has three parallel control loops. The main loop performs MPPT based on a perturb & observe algorithm [63]. It takes PV current and

voltage measurements as inputs and perturbs the voltage setpoint to find the MPPT. Additionally, it has a DC-bus voltage and PV current control loop to limit the duty cycle based on its maximum current and DC-bus voltage. The latter has a setpoint even higher than the BES converter DC-bus voltage controller and is merely used as a safety measure to shut down in case of a DC-bus over-voltage. Since the PV converter utilizes the same hardware as the BES converter, the zero current detection and QR-BCM detection are identical.

3.4.4 *EV converter*

Four parallel control loops determine the bidirectional EV charger setpoints. The primary function is to control the EV charging and discharging current. Additional functions include DC bus over-voltage control and EV battery voltage control when the maximum battery voltage is reached. Finally, it also has protections in place to shut down in case of under- and overvoltages.

Since the inverter primarily maintains the power balance, and every connected converter has multiple parallel control loops, safety and stability can be ensured even when the number of converters is increased, and the resulting topology can be considered modular. The experimental results related to the multi-port system control loops are discussed in the next section.

3.5 EXPERIMENTAL VERIFICATION

The EV-PV-BES integrated prototype is shown in Fig. 27.

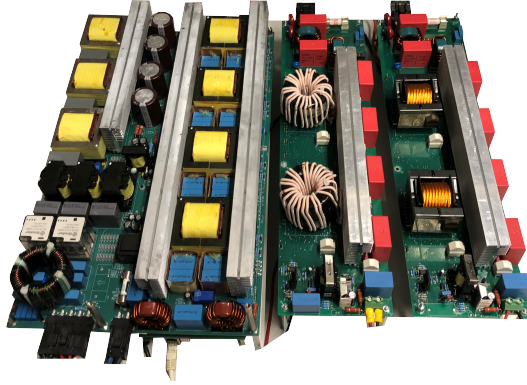


FIGURE 27: Experimental prototype of the DC-integrated EV-PV-BES multi-port converter. From left to right: the DC-AC converter including LC-filters for the grid connection, the 4-phase IFBC for isolated EV charging, and two the two phase FSBBCs for both the PV and EV.

3.5.1 *Interleaved Flyback Converter*

In Fig. 28(a)-(b) the drain-source and gate-source voltages of the EV charger are shown, for a 750V input voltage, 10A output current and 400V EV voltage. Under these conditions, full ZVS is achieved. If the output current and voltage are reduced, the maximum switching frequency of 400kHz will be reached and the converter will start valley skipping. The control will then wait till the second zero-crossing (or minimum) of the corresponding drain-source voltage before turning on the switch again. This way, low power loads can be achieved while limiting the switching frequency. An example of the flyback converter valley-skipping at 1A output current and 100V EV voltage is shown in Fig. 28(b).

3.5.2 *DC-AC Converter*

Fig. 29 shows the three phase grid currents and EV current during an EV load step from -8A to 8A. Fig. 29 shows the capability of the DC-AC converter to maintain power balance, even during a power direction change. When the EV current has a linear slope it is limited by the maximum

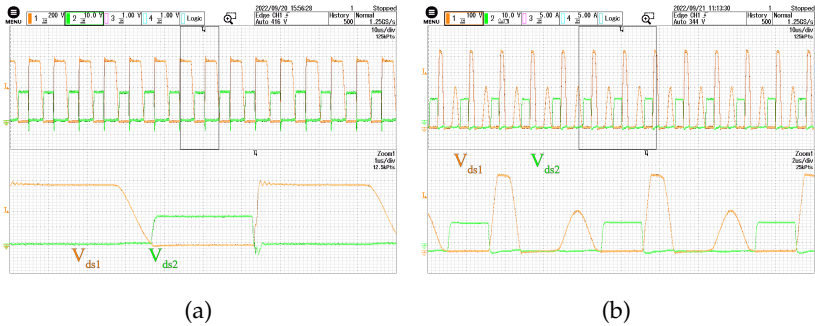


FIGURE 28: Drain-source voltages and gate-source voltages of the IFBC, at (a): 75V input voltage and 400V EV voltage, at 10A output current, and (b): 100V, 1A output voltage and current, respectively. Under the reduced load conditions the IFBC can start valley-skipping to limit the switching frequency.

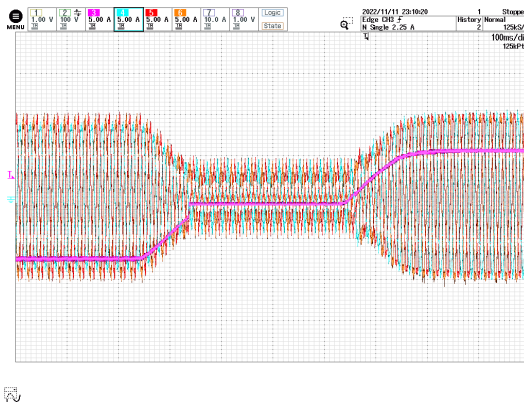


FIGURE 29: The AC grid currents and EV charging currents during a bidirectional EV load change from -8A to 8A (DC).

setpoint rate of change of 30A/s. By introducing a maximum rate of change the controller gains can be increased, resulting in fast and accurate control for both small and big load changes. Additionally, Fig. 29 also shows that the controllers are reset whenever the load current approaches zero. This allows the DC link voltage control to reset and prevent overshoots.

The primary task of the BES and EV converter is to control their charging current, whereas the PV converter performs maximum power point tracking

by controlling the PV panel voltage. Finally, the DC-AC converter maintains power balance by controlling the DC-link voltage. Besides their primary tasks, the DC-DC converters also include in- and output voltage control loops, cascaded with their primary loops. This allows the design to be designed modularly while maintaining power balance.

3.5.3 Cascaded Control & Protection

Fig. 30(a)-(b) show the experimental verification of the cascaded control loop shown in Fig. 26. As mentioned in the previous section, the primary task of the EV and BES is to control their charging current. However, in case their combined charging or discharging power overloads the inverter, the cascaded voltage control loops step in their current setpoints are adjusted to maintain power balance (by controlling the DC link voltage). The first converter to step is the FSBBC converter used for the BES, when the DC link voltage deviates more than 20V from its nominal 750V.

In Fig. 30(a)-(b) the FSBBC has a fixed output current setpoint of 14A, while the setpoint of the EV is increased from 8A to 18A. The combined power exceeds the maximum power of the DC/AC converter and when the DC bus voltage decreases the under-voltage control of the BES charger curtails its power to maintain a constant bus voltage of 770V, as shown in Fig. 30(a). The AC currents show that the output power of the DC/AC converter is not exceeded and is therefore not overloaded. In Fig. 30(b) the EV setpoint is again reduced to 8A, after which the BES stops curtailing its power and the DC link voltage is again controlled by the DC/AC converter. Please note that the DC bus voltage here is measured with an AC coupling. The cascaded control-loops allows the system to be modular, as all protection is performed on a module level.

3.5.4 Multi-port System Efficiency

Finally, the resulting port-to-port efficiencies are shown in Fig. 31. The non-isolated FSBBC (PV or BES) shows the highest efficiency with a peak efficiency of 99.5% at full power, next the IFBC has peak efficiency of 98.7% and the DC/AC converter has a peak efficiency of 98%. Combined this results in port-to-port peak efficiencies shown in Table ??.

3.6 CHAPTER CONCLUSIONS

This chapter has summarized the hardware and control loop design of the multi-port converter. First, based on a literature survey, it has been decided

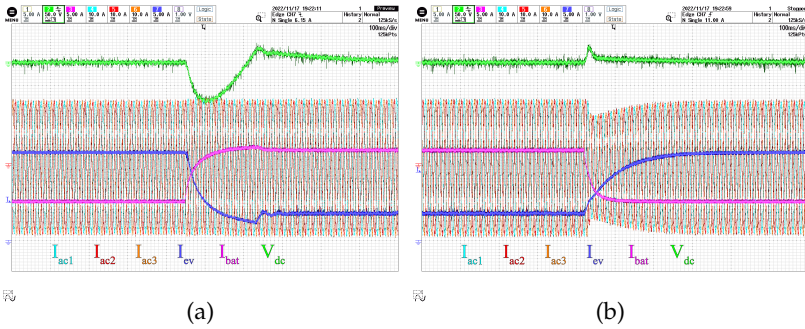


FIGURE 30: Cascaded V-I control loop of the FSBBC showing (a): power curtailment (DC link voltage control) in case of inverter overloading, (b): reset to current control, with the DC-AC converter again controlling the DC link voltage, after the EV setpoint has been reduced.

Direction	peak efficiency at full power
PV → EV	98.2%
PV → BES	99%
PV → grid	97.5%
grid → EV	96.7%
BES → EV	98.2%

TABLE 8: Caption

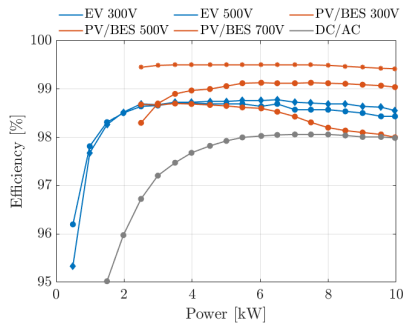


FIGURE 31: Efficiency of the flyback converter (EV), the four-switch buck-boost converter (PV/BES), and the DC/AC converter.

that the DC-integrated multi-port converter is the best suited topology for this application, since it requires the least amount of conversion steps and the modular design allows it to be scalable for different use cases.

Next, the experimental verification of the proposed 10kW four-port converter is discussed. The experimental results show the operation of all converters, and show the ability of the cascaded control loops to curtail BES power in case of inverter overloading. The proposed converter exhibits a peak efficiency of 98.2% for PV \rightarrow EV, 99% for PV \rightarrow BES, 96.7% for grid \rightarrow EV, and 98.2% for BES \rightarrow EV.

Part II
SMART CHARGING

MODELLING BATTERY DEGRADATION

This chapter introduces the various modelling techniques used to model battery degradation and provides a detailed review of empirical and semi-empirical battery degradation models. The chapter focuses on empirical and semi-empirical models because their relative simplicity makes them applicable for use in optimization problems, such as smart charging. However, at the same time, this simplicity is the pitfall of these models as they tend to oversimplify the degradation behaviour. Therefore, a good understanding of battery degradation behaviour and modelling limitations is required for correct implementation and use.

This chapter is based on:

- J1 W. Vermeer, G.R. Chandra Mouli, P. Bauer, *A Comprehensive Review on the Characteristics and Modelling of Lithium-ion Battery degradation*, 2022, *IEEE Transactions on Transportation Electrification*

4.1 INTRODUCTION

Over time and use, lithium-ion batteries (LIBs) lose part of their energy capacity and power handling capability as a result of parasitic side reactions. This is called battery degradation, and the time it takes before a specific energy capacity threshold (or power handling threshold) is reached is called the lifetime of the battery. Unfortunately, battery lifetime is often a trade-off with other desired characteristics, such as maximum current rating, maximum cycle depth, and density. Therefore, from an application perspective, a direct trade-off exists between momentarily achieving the highest gain by heavily using the LIB, versus reducing the load of the LIB and achieving a longer lifetime. This is directly applicable to smart charging as well. For example, the objective of a smart charging system could be to minimize the cost of energy, if the cost of electricity would temporarily drop, the smart charging system would like to fully captivate on that moment and start charging its energy storages, both vehicular and stationary, at maximum power. As a result, it bought relatively inexpensive energy. However, the operational expenditure of heavily loading the LIBs is not taken into account, and the total cost of acquiring that energy might be sub-optimal.

The goal of this chapter is to get a good understanding of LIB degradation behaviour and its modelling, so that the effects of LIB degradation can be taken into account in the control and sizing of the EV-PV-BES integrated smart charging system, discussed in the next chapter. This is achieved by reviewing empirical and semi-empirical modelling techniques and degradation studies, focusing on the trends observed between different studies and highlighting the limitations and challenges of the various models.

4.1.1 *Modelling of Battery degradation*

Methods for modelling LIB degradation behaviour are divided into four different categories:

1. Physics-Based Models (PBM)
2. Equivalent Circuit Models (ECM)
3. Machine Learning Models (MLM)
4. Empirical Models (EM)

A comparison of these models is given in Table 9. Physics-based models,

Model	Complexity	Accuracy	Amount of data	Applications
PBM	high	high	low	battery design
ECM	medium	medium	high	SoH estimation
MLM	medium-high	medium	high	SoH estimation
EM	low	low-medium	high	System design & Optimization

TABLE 9: Comparison of different degradation model techniques.

also known as electrochemical models intend to model the electrochemical and physical processes in the battery. The first PBM was developed by Doyle and was based on the porous electrode model [64, 65]. The pseudo-2D model expanded on this by adding a thermal model [66], including diffusion kinetics and Butler-Volmer kinetics [65]. Later, the effect of parasitic side reactions, such as solvent oxidation [67] or SEI layer growth [68, 69] were added to these equations to account for degradation. Others have tried to reduce the computational complexity for these models to be more widely applicable [70]. PBMs can achieve high accuracy, but they require many partial differential equations and a thorough understanding of all physical and chemical mechanisms. Furthermore, LIB degradation is frequently caused by multiple factors, making molecular modelling even more difficult and prone to miss out on macro-level effects [71]. As a result, electrochemical models are generally not used by non-chemical engineers/researchers [72].

Equivalent circuit models (ECM) do not require this information and instead model the transient response of the battery using passive circuit components such as resistances, capacitances, and inductances. More complex models can also be used to simulate the internal diffusion and charge transfer processes. And based on impedance data, degradation can be incorporated using variable components. This, however, requires large test matrices to quantify the degradation with respect to operational conditions. Due to their mathematical simplicity, they are frequently used in real-time applications, such as battery state estimations [73]. Often combined with state-estimators such as Kalman- or particle filters [71, 73].

Another common state-of-charge (SoC) and state-of-health (SoH) estimation technique involves machine learning (ML), such as support vector machine or neural networks. Different ML approaches exist, some train the algorithm to extract the SoH from the differential voltage curve or incremental capacity curve of the battery [74, 75]. The advantage of these approaches is that they only require easily obtained parameters such as

voltage, current and temperature. Others combine ML with different models to train the algorithm based on model parameters such as ohmic resistance, polarization resistance and polarization capacitance [76, 77], or combine empirical modelling techniques with regression models to predict the SoH [78]. High accuracies can be obtained with ML methods, however, large data sets are needed to train the algorithms [71, 79]. Finally, empirical and semi-empirical models (abbreviated as EM) curve-fit the relationship of various stress factors onto the data resulting in a relatively simple analytical formula. Their simplicity allows using EMs in a wide variety of studies, such as system-level design problems, optimization models, battery management systems, among other things. Additionally, the analytical formulae give an intuitive feel to the effect of various stress factors. However, large test matrices are required to decouple their impact (if even possible), which is generally limited by the available equipment. As a result, EMs are prone to oversimplify the complex behaviour of LIB degradation and the correlation between stress factors, this is discussed in more detail in the next section.

4.1.2 *Challenges of Empirical and Semi-empirical degradation Models*

Without a good understanding of LIB degradation behaviour and modelling limitations, the simplicity of EMs can pose challenges as they can easily lead to significant modelling errors. A summary of these challenges is given below:

1. Accelerated test conditions: degradation tests are frequently performed under accelerated degradation conditions such as high temperature, high C-rates, and high voltages to speed up degradation. While this reduces the amount of time required for testing, it also reduces the accuracy of the models when they are utilized outside of the test conditions. For example, models are often developed based on temperatures of 40°C and higher. Whereas very rarely models are tested below 25°C, and even fewer studies have evaluated multiple operating conditions below 25°C. As will be demonstrated in this study in section III.4, the use of testing conditions at temperatures that will never actually be reached or sustained for longer periods of time during normal operation can cause unreliable results. Especially at temperatures below room temperatures, where the effect of high-temperature degradation mechanisms will decrease, and other degradation mechanisms take over.

2. Limited test conditions: large test matrices are required to accurately model the effect of multiple stress factors, which are generally limited by the amount of available equipment. Here a good understanding of the expected degradation behaviour can help to determine the test conditions more strategically.
3. Stress factor interdependency: a good understanding of the interdependencies between stress factors is required to select an appropriate model and testing conditions for a particular use case. For example, based on the reviewed studies in this paper, it is observed that a strong correlation between the effect of temperature and C-rate exist. However, not many models model the interdependency of these stress factors. As a result, the actual operating range of the model might be limited to only the accelerated testing conditions. Furthermore, even within the test condition range, significant errors might occur when these interdependencies are not considered.
4. Modelling limitations: besides the effect of operational conditions, a good understanding of the model's fundamental limitations is also required. For example, depending on the chosen parametrical fit, EMs might be limited to a specific part of the battery lifetime or might be less suited for applications with very irregular charge cycles or applications with a different calendar- to cyclic degradation ratio.

4.1.3 *Related Work & Scientific gap*

In [80, 81] an in-depth review of the main degradation mechanisms on a material level is discussed. These studies are elaborated in [82, 83], where the authors also review the factors influencing degradation on a cell and battery pack level. The authors of [65, 71, 84] review the main degradation mechanisms and provide an overview of different degradation estimation techniques, including electrochemical models, equivalent circuit models, empirical models and statistical models. A similar approach for data-driven health diagnostics and prognostic techniques is performed in [79]. In [85] a comparison of several EMs is performed based on a conceptual smart grid framework. Furthermore, several studies have reviewed the various techniques for state-of-health estimation [86–89]. In [88] the authors discuss different types of self-adaptive SOH monitoring techniques, such as support vector regression, neural networks, or particle filter method. Additionally, a more broad overview of different types of SOH and remaining-useful-

life (RUL) estimation techniques is given in [86, 87, 89], including direct measurement techniques, model-based techniques, and adaptive filtering techniques.

All of the studies mentioned above aim at providing a broad overview of different kinds of degradation mechanisms or degradation estimation techniques, whether that includes model-based techniques, data-driven techniques are self-adaptive techniques. In most of them, EMs are briefly mentioned as a part of this. However, given the scope of these studies, they do not provide an in-depth review of different empirical models, nor do they provide any insights into the correlations found between different studies. Even [85], which is entirely focused on EMs, provides a simplified description of the effect of operational stress factors. Furthermore, none of the above mentioned studies actually review and compare the degradation behaviour of different degradation studies, which makes it even more difficult to provide generalizations in terms of impact of operational conditions, or modelling accuracy. As explained above, this is especially problematic for EMs, since without a proper understanding of battery degradation, empirical degradation modelling, and its limitations and challenges, the simplicity of EMs can easily lead to significant modelling errors in a wide variety of studies.

4.1.4 *Contribution*

LIB degradation is an important factor for developing new LIBs and optimizing their techno-economic performance. In this regard, multiple studies have reviewed the various methodologies for degradation estimation. However, based on the aforementioned challenges and related work it is concluded that a significant scientific gap still exists. Since no study has yet thoroughly reviewed empirical and semi-empirical models and has investigated the correlations between different studies, to highlight the limitations of the models, and focus on the reasons for the observed trends and insights. Due to the simplicity and widespread use of EMs, this can potentially result in significant modelling errors. To this extent, the main contributions of this study are summarized as follows:

1. A comprehensive review of empirical and semi-empirical modelling techniques for LIB degradation, with a focus on operational stress factors and their interdependence, modelling techniques, limitations, and challenges, so that these models can be used accurately at the relevant operating conditions.

2. A detailed review of the degradation behaviour of various LIB cells, investigating the correlations between different degradation studies and examining the relationship with operating conditions, degradation mechanisms, and modelling techniques.

In the remainder of this chapter the main degradation mechanisms for LIBs are summarized in section 2.2. Next, the review of degradation behaviour and different modelling techniques is discussed in section 2.3. Here, a distinction is made between calendar and cyclic degradation. The modelling techniques, limitations and challenges, and key insights are discussed per stress factor for both calendar and cyclic degradation. Lastly, the current challenges and future trends regarding LIB degradation and degradation modelling are described in section 2.4.

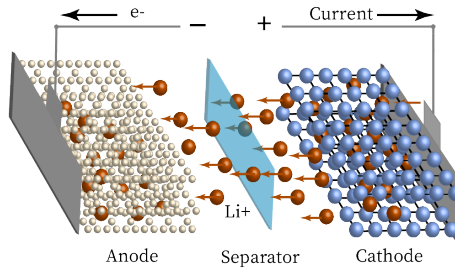


FIGURE 32: A simplified representation of a lithium-ion battery consisting of an anode, cathode, separator, and electrolyte (the electrolyte is not shown for clarity, as it fills the entire battery). The arrows indicate a charging process where the Li-ions intercalate into the anode, resulting in an opposite electron flow.

4.2 MAIN DEGRADATION MECHANISMS

Figure 32 shows a simplified representation of an electrochemical battery. The four main components of a LIB are the:

1. Anode, the most often used material is graphite [80, 90, 91], other common materials are lithium-titanate-oxide (LTO) or Silicon [92].
2. Cathode, which is made of a composition material that contains Lithium. Commonly used materials are Lithium Iron Phosphate (LFP), Lithium Nickel Manganese Cobalt Oxide (NMC), Lithium Manganese Oxide (LMO), and Lithium Nickel Cobalt Aluminium (NCA).

3. Electrolyte, a composition of lithium salts and organic solvents [85]. The electrolyte is mainly used to transfer ions between the cathode and the anode.
4. Separator, a porous plastic that separates the anode and cathode to prevent short-circuiting the electrodes.

During charging, Li-ions deintercalate¹ from the cathode, move through the electrolyte and separator before they intercalate at the anode. The resulting flow of ions creates an electrical current opposite to the flow of electrons, as shown in Figure 32. The degradation of LIBs occurs during both cycling and idle state and is caused by physical stress, and chemical side reactions [82, 93]. Additionally, many factors influence battery degradation, such as cell chemistry, cell design, pack design, and operating conditions. LIB degradation is commonly categorized into three different degradation modes [80, 82, 90, 94, 95]:

1. Loss of Lithium Inventory (LLI): represents the loss of active lithium ions that are no longer available for cycling. Causes for LLI can be parasitic side reactions such as, surface film formation, decomposition reactions, lithium plating, among other things. LLI is associated with capacity fade, i.e. the loss of effective mAh of the cell.
2. Loss of Active Material (LAM): represents the loss or structural degradation of the available anode or cathode material. Possible causes include electrode surface layer growth or cycling induced cracks/exfoliation. LAM can cause both power and capacity fade.
3. Conductivity Loss (CL): also known as contact loss [80], describes the degradation of electrical parts such as the current collector corrosion and binder decomposition.

A fourth addition could be the loss of electrolyte, which would lead to LAM and CL after a certain point and is therefore not separately mentioned. Even though differentiated into three categories, the degradation modes often interact, and a single degradation mechanism such as surface layer formation can trigger multiple degradation modes. A summary of operational conditions, the corresponding degradation mechanisms and their effect on LIB degradation is shown in Figure 33. Furthermore, A graphical representation of all degradation mechanisms is shown in Figure 34. The following two subsections will discuss these degradation mechanisms, here a division is made between the mechanisms that occur at the anode and

¹ Intercalation is the insertion of molecules into the electrodes

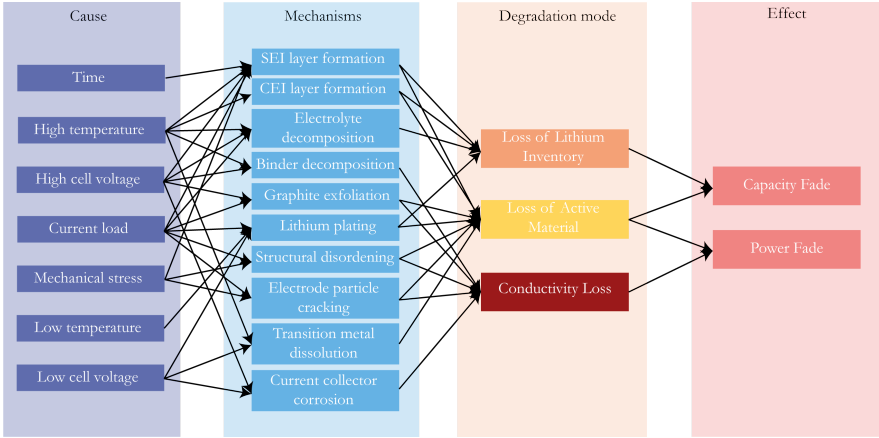


FIGURE 33: Overview of the correlation between operational stress factors (the causes for degradation), the corresponding degradation mechanisms, degradation mode, and their effect on LIB degradation. Based on a combination of [90, 93, 95].

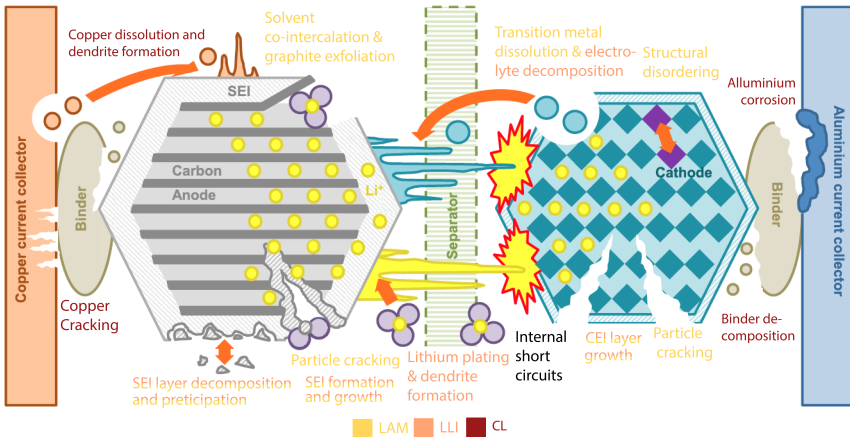


FIGURE 34: Graphical summary of degradation mechanisms in graphite based LIBs. The degradation mechanisms are colour coded with respect to the accompanied degradation mode. The figure is adapted from material made publicly available by C.R. Birki et al. in [90], under Creative Commons Attribution 4.0 License CC-BY.

the cathode, respectively. The degradation of the electrolyte and its effect on battery degradation mainly takes place at the electrodes [80] and is therefore not separately discussed.

4.2.1 *Anode degradation*

The majority of LIBs use graphite as their anode material [80, 84, 96], so this section focuses on graphite based LIBs.

4.2.1.1 *Solid Electrolyte Interphase Layer*

The operating voltages of various common electrode materials in comparison to the electrochemical stability window of organic electrolytes are shown in Figure 35. The operating voltage of graphite anodes is in the 0.05V-1V range [93, 97], which is outside the organic electrolyte stability window of 1V-4.5V. As a result, graphite-based LIBs are thermodynamically unstable, resulting in a reductive electrolyte decomposition reaction. This reaction consumes Li^+ ions and forms a surface layer on the anode, resulting in LLI and LAM [80, 91, 93]. Especially in the first few cycles, the reaction rate is high, creating a surface layer permeable for Li-ions but less permeable for electrolyte components. This reduces the rate of decomposition and further electrode corrosion [80, 98–100]. However, even though the reaction rate reduces, the transport of solvated lithium and other electrolyte components through this semi-permeable layer continues throughout the battery's life. This reaction mainly occurs at the interphase between the electrolyte and the anode and is called the Solid Electrolyte Interphase (SEI) layer. The Solid Electrolyte interphase (SEI) layer's growth is often one of the main degradation factors of graphite anodes. It reduces the battery's available energy capacity and power handling capability. Another type of anode surface layer grows on the basal plane surface and is impermeable for Li-ions and therefore sometimes referred to as the non-SEI layer [101]. However, often the SEI and non-SEI layers are both referred to as SEI layer [80]. Therefore this convention is followed here as well.

After the initial formation of the SEI, it continues to grow during both cycling and idle conditions. The rate at which the SEI layer grows is dependent on the operating conditions of the cell [104, 105]. During idle conditions, SEI growth is mainly driven by temperature and state of charge (SoC). At a higher SoC, more Li-ions are intercalated into the anode, decreasing the anode potential and increasing the reductive reaction rate [97]. Additionally, an increasing temperature also increases the reaction rate and might cause

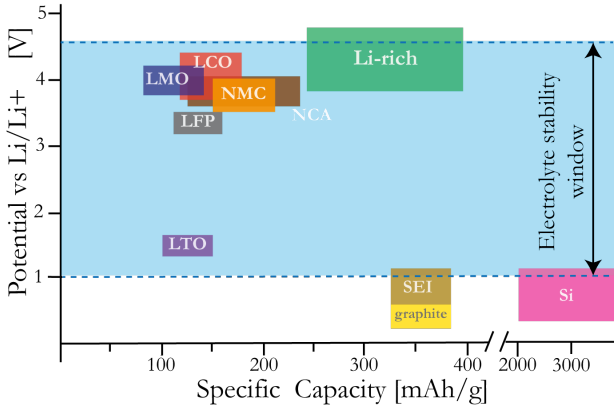


FIGURE 35: Voltage versus energy capacity of five common electrode materials, compared to the electrochemical stability window of liquid organic electrolytes, adapted from [102, 103]. It shows that graphite is outside the electrochemical stability window of organic electrolytes, rendering graphite-based Li-ion batteries thermodynamically unstable and causing SEI layer growth.

the less stable organic SEI components to change into more stable inorganic products, reducing the SEI layer's ionic conductivity. At extreme temperatures above 60°C even thermal runaway can cause the cell to catch fire or explode. Aside from SoC and temperature, volume changes caused by the (de-)intercalation of Li-ions during cycling cause mechanical stress on the electrodes. These volume changes can crack the SEI, allowing new reactions to occur. As a result of this crack and repair, the SEI continues to grow, resulting in additional LLI and LAM [80, 106, 107]. Furthermore, cycling, especially with high C-rates, creates a more porous SEI layer compared to idle conditions [104, 105]. This increased porosity allows for more reductive reactions to occur, whereas a more dense SEI layer reduces the reaction rate. Other factors influencing the reaction rate are electrolyte composition and electrode balance [100, 108]. Two opposing theories exist regarding SEI formation: 1. The first theory assumes that the formation takes place at the electrode/electrolyte interface and that the electronic conductivity of the SEI should be the limiting factor of formation [81]. 2. The second theory states that SEI formation takes place at the anode-SEI interface and is limited by the solvent diffusion process [109]. However, both theories result in a degradation behaviour that follows a $\sqrt{\text{time}}$ relationship, which

is typical for the passivation character of the SEI layer and similar to what is often observed in experiments.

4.2.1.2 *Lithium plating*

At lower temperatures, generally below 20°C , the diffusion rate of lithium into the anode or electrolyte reduces, and the intercalation potential of graphite material approaches that of metallic lithium. Metallic lithium plating may occur as a result of this. Lithium plating is especially likely to occur at low SoC, low temperature, and high C-rates [90]. Furthermore, after a certain age, the anode resistance can reach a critical limit. After this limit, the anode potential drops below 0V vs Li/Li^+ , and lithium plating starts to occur [105, 110].

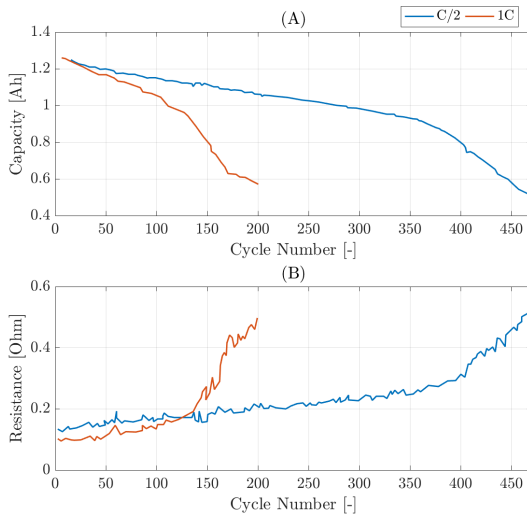


FIGURE 36: Effect of lithium plating on remaining capacity and internal resistance for two LCO cells: after a certain age lithium plating can start to occur, causing an increased degradation rate (inflexion point) in both capacity and resistance deterioration [81].

Unlike SEI layer growth, lithium plating is a positive reinforcing phenomenon: as it occurs, it deposits on the anode, reducing the active surface area and resulting in a higher current density at the remaining available pores, further increasing the metal plating. As a result, a knee-point in the

degradation behaviour is frequently observed at the age at which lithium plating occurs. An example of this is shown in Figures 36 (a)-(b), where two inflexion points are observed in both the capacity and impedance deterioration. Lithium plating causes LLI and possibly reduces the cell's safety, as lithium dendrites can start to grow, leading to internal short circuits [80].

4.2.1.3 *Mechanical Stress at Anode*

The intercalation of lithium ions into the anode can result in abrupt changes in volume as the particles undergo a phase transition [80, 111]. During a phase transition, the orientation of the molecules changes as more lithium is inserted, resulting in different geometrical and electrical properties. This causes volume change induced mechanical stress, which can lead to anode structural damage (LAM), surface layer cracking (LLI and LAM), and contact loss with the composite electrode (CL). The active material's volume change may also result in a decrease in electrode porosity, which is required for the electrolyte to reach the bulk of the electrode. [80].

4.2.1.4 *Transition Metal Dissolution*

Most lithium batteries' cathodes contain transition metals such as iron, nickel, cobalt, manganese, and vanadium. Similarly, most battery electrolytes contain the salt LiPF_6 . The cycling and storage of these cells, particularly at high cell voltages and high temperatures [112], can result in the formation of hydrogen fluoride (HF) from impurities inside the electrolyte, which increases the acidity of the electrolyte. The resulting HF corrodes the cathode and dissolves the transition metals, contributing to several degradational mechanisms in both the anode and the cathode, causing capacity fade and impedance rise. To begin, metal dissolution can cause structural degradation of the cathode (LAM), resulting in reduced lithium insertion capability [113]. Furthermore, after dissolution, the metals can migrate through the electrolyte and deposit on the anode, acting as catalyzers for the reductive decomposition reaction that causes SEI layer growth [114]. Finally, the deposition of transition metals on the anode during this reductive process may induce the formation of lithium metal dendrites on the deposited metals (LLI and LAM). These dendrites can cause internal short circuits, posing a significant safety risk.

Particularly spinel-containing chemistries, such as LiMn_2O_4 are vulnerable to transition metal dissolution, as the extent of dissolution can be much greater, resulting in more structural degradation of the cathode (LAM).

Although transition metal dissolution is unavoidable during the charging process, it can be reduced by reducing impurities in the electrolyte, using dopants, and using protective coatings around the cathode to reduce direct contact between the cathode and the electrolyte. [114].

4.2.1.5 *Other degradation Mechanisms*

Other degradation mechanisms at the anode include graphite exfoliation: the structural degradation of graphite (LAM) as a result of high current densities or solvent co-intercalation, particle cracking (LAM) as a result from mechanical stress or high current load, binder decomposition (CL) caused by high temperatures and high cell voltages, corrosion of current collectors (CL) and loss of electrical contact (CL). For more details, interested readers are direct to [80, 81, 90].

4.2.1.6 *Lithium-Titanate-Oxide and Silicon-based Anodes*

The main advantage of Lithium-Titanate-Oxide (LTO) anodes over graphite anodes is their higher potential, as shown in Figure 35. As a result, these anodes are not thermodynamically unstable and therefore do not form an SEI layer [115]. Furthermore, LTO is a zero-strain material that does not change volume when charged or discharged. As a result, LTO-anode batteries can handle extremely high C-rates while still retaining a long lifetime. This comes at the cost of a lower energy density due to their higher potential [116].

On the other hand, silicon (Si) based anodes have a superior energy density, with a theoretical capacity of 3580 mAh/g, compared to 350mAh/g for graphite-based anodes and 175mAh/g for LTO-based anodes [117]. However, during cycling, the volume of the silicon particles can change by up to 280 percent. These volume changes cause excessive mechanical stress, reducing their lifetime significantly [92].

4.2.2 *Cathode degradation*

The cathode is the lithium-containing part of a cell, and the limiting factor during charging as its maximum voltage determines the end of charge voltage. Similarly, the anode is the limiting factor during discharge due to its minimum discharge voltage limit [90, 118]. In terms of degradation, the cathode is generally regarded as less significant [119, 120].

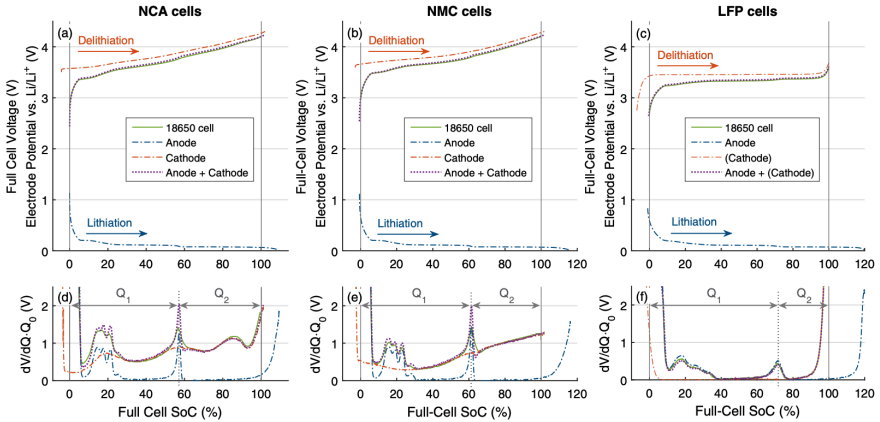


FIGURE 37: (a-c): Voltage and differential voltage profile of an NCA (a), NMC (b), and LFP (c) full cells during low current charging, including a reconstructing of full cell voltage based on half-cell voltage profiles (dotted lines). (d-f): Differential voltage spectra of the three different cells. Figures (c) and (f) show that the cathode voltage profile of an LFP cell is very flat compared the other two chemistries, due to the two-phase regime. The figure is obtained from the publicly available material of P. Keil et al. in [23], under the Creative Commons Attribution 4.0 License CC-BY.

Common cathode chemistries are LCO, LFP, NMC, LMO and NCA. These chemistries all have their strengths and weaknesses, varying in energy- and power-density, toxicity, safety, cost and natural abundance, among other things. Although many more chemistries exist, this review focuses on the most common materials.

The main degradation mechanisms of cathode materials include surface film formation, mechanical stress, and transition metal dissolution. Other degradation mechanisms on the inactive components include current collector corrosion, binder decomposition, and conducting agent oxidation [80, 111], as seen in Figure 34. The most significant degradation mechanisms are discussed below.

4.2.2.1 *Cathode Surface Layer Film*

Surface layer films (also known as Cathode Electrolyte Interphase (CEI) layer) can form on the cathode, similar to the anode, but due to electrolyte oxidation and salt deposition [80, 121, 122]. In contrast to the SEI layer, the cathode surface layer shows low lithium-ion conductivity, increasing the impedance. Furthermore, also gas evolution is possible [80, 81]. According to the authors of [81], organic products formed by reduction at the anode may also be transported to the cathode, where they are oxidized and deposit on the cathode surface, resulting in LAM and LLI. Similar findings have been made in [123]. Unfortunately, due to the higher voltage of the cathode, this surface film layer is more difficult to detect [121, 122].

4.2.2.2 *Mechanical Stress at Cathode*

The cathode, like the anode, can go through phase transitions during the intercalation and deintercalation of Li-ions, which can result in LAM and CL. The amount of volume change varies depending on the chemistry. LFP cells, for example, only have a two-phase regime consisting of FePO_4 and LiFePO_4 [124]. As a result the (cathode) voltage and differential voltage profile of these cells is very flat, as shown in Figure 37. Because of this two-phase regime, LFP cells exhibit only a slight increase in volume, around 6.8% [125] and have a very high rate capability as well as a good lifetime [124]. Other chemistries, such as NCA or NMC, show multiple phase transitions in both cathode and anode voltage profiles.

Manganese-containing chemistries, particularly LMO, exhibit additional mechanical stress as a result from Jahn-Teller distortion of Mn^{3+} particles. This results in a phase change from cubic to a tetragonal form. In the case of LMO, this can increase the cathode volume by approximately 16% [80, 93] resulting in additional LAM [126, 127]. Jahn-Teller Distortion occurs at low SoC. By controlling the end-of-discharge-voltage (EODV) and adding dopants, the capacity fade caused by volume change can be reduced .

4.2.2.3 *Transition Metal Dissolution*

As mentioned above, transition metals in the cathode can dissolve resulting in structural degradation of the cathode (LAM).

4.3 REVIEW OF EMPIRICAL DEGRADATION MODELLING

This section discusses the most common empirical and semi-empirical modelling techniques and their limitations. Furthermore, the cells' degradation behaviour is discussed, and where possible, explained using the described degradation mechanisms. LIB degradation can be divided into two different types:

- Calendar degradation: the degradation which occurs when the cell is in an idle state. Calendar degradation results from side reactions that take place due to thermodynamic instability of the materials [81].
- Cyclic degradation: includes the degradation as a result of cycling the battery. Various kinetically induced effects, such as volume variations or concentration gradients, result in additional degradation [81, 97].

Following the reviewed studies, this paper focuses more on capacity fading than resistance increase. A summary of all studies and their testing conditions can be found in Tables 10 and 11.

4.3.1 *Calendar degradation*

Capacity fading due to calendar degradation can be separated into two parts: reversible and irreversible capacity loss. By recharging the battery, the reversible part can be restored, whereas the irreversible part cannot. This review focuses on the irreversible part of calendar degradation. Reversible capacity loss is studied in more detail in [128, 129]. The three factors that influence calendar degradation are 1. Temperature, 2. SoC and 3. Time. In the following sections, the impact of these stress factors will be discussed separately. However, it is important to note that their degradation behaviour is not entirely independent of one another but is strongly correlated. A summary of all reviewed calendar degradation models, including their range of test conditions is shown in Table 10.

4.3.1.1 *Time*

MODELLING TECHNIQUES: TIME

It is widely reported in the literature that the major degradation effect for graphite anode based LIBs is the formation and growth of the SEI layer [123, 131, 142, 143, 148, 149]. As mentioned above, SEI layer growth is generally associated with a $\sqrt{\text{time}}$ degradation behaviour. To this extend,

Study	Chemistry	Cap.	Res.	Factors	Conditions		
					Temp.	SoC	Time
[130]	LFP	✓	x	SoC, T, time	30-60°C	30-100%	850 days
[131]	LFP	✓	x	SoC, T, time	40-55°C	10-90%	800 days
[132]	LFP	✓	✓	SoC, T, time	30-60°C	30-100%	450 days
[133]	LFP	✓	x	SoC, T, time	30-50°C	30-90%	300 days
[120]	LFP	✓	✓	SoC, T, time	30-60°C	30-100%	225 days
[134]	LFP	✓	✓	SoC, T, time	25-55°C	30-100%	305 days
[135]	LFP	x	✓	SoC, T, time	40-55°C	10-90%	225 days
[136]	LFP	✓	x	SoC, T, time	40-60°C	40-80%	105 days
[137]	LFP	✓	x	SoC, T, time	40-55°C	10-90%	-
[138]	NMC	✓	✓	SoC, T, time	30-60°C	30-100%	480 days
[139]	NMC-LMO	✓	x	SoC, T, time	60°C	10-100%	252 days
[140]	NMC-LMO	✓	✓	SoC, T, time	30-50°C	30-90%	290 days
[141]	NMC	✓	✓	SoC, T, time	0-45°C	25-100%	450 days
[72]	NMC	✓	✓	SoC, T, time	35-50°C	0-100%	520 days
[142]	NMC	✓	x	SoC, T, time	35-50°C	0-100%	520 days
[143]	NMC	✓	✓	T, time	10-46°C	50%	520 days
[144]	NMC-LMO	✓	✓	T, time	30-60°C	30-100%	1200 days
[145]	NCA	x	✓	SoC, T, time	30-55°C	90-110%	219 days
[146]	-	✓	x	SoC, T, time	30-60°C	30-100%	800 days
[147]	-	✓	x	SoC, T, time	0-60°C	5-100%	9 year

TABLE 10: Overview of studies investigating empirical and semi-empirical calendar life models

the time dependency of calendar degradation is most often modelled using a power-law relationship with z in a range of 0.5 to 0.8 [131], as shown in Eq.(13).

$$Q_{loss} = f(SoC, T)t^z \quad (13)$$

Where,

- Q_{loss} : lost charge.
- $f(SoC, T)$: function describing the state of charge and temperature dependency of calendar degradation

- t : time
- z : power exponent

An example of a corresponding degradation curve is shown in Figure 38. The exponential or pre-exponential components are often functions of SoC and temperature. In general, a higher SoC or higher temperature results in an increased calendar degradation rate. At a higher SoC, more lithium is intercalated in the anode resulting in a lower anode potential (V vs. Li/Li⁺)² and higher reaction rate. Similarly, as the particle collision rate increases at higher temperatures, the reaction rate increases. This is confirmed by the results of [72] shown in Figure 38. It also shows that for a lower SoC the capacity retention follows a more linear curve. Comparable results were observed in [130–132, 141, 150]. A possible explanation for the linear decay is cathode surface film growth, which has a non-passivation character. Therefore its reaction rate does not decrease over time³ [151]. Another explanation could be transition metal dissolution as a result of high-temperature storage.

LIMITATIONS & CHALLENGES: TIME

An occasionally observed result is a slight increase in capacity when the cell is still relatively new. This is most commonly observed for lower SoC storage, but is also observed under cycling conditions [72, 128, 141, 142, 152]. Again this is also shown in Figure 38, for the 0% and 10% SoC lines. After this initial increase in capacity, the capacity fading generally follows a similar trend as for other conditions, and therefore the found empirical fit is often still valid, even though it has been offset by the initial increase. The authors of [142] mention electrochemical milling as a potential cause for the increase in capacity. In [153] the so-called relaxation effect, due to the long resting period after cycling, is mentioned as a possible explanation. This relaxation effect can be caused by a change in local charge equilibrium, a drop in concentration gradient of active material and electrolyte, and a change in double-layer capacitance structure. Another explanation given in [128] denotes the passive electrode effect as a possible explanation; here, a slow movement of active lithium particles between the passive and active part of the anode is given as an explanation for the rise in capacity.

² lithium metal composites have a negative potential; therefore, voltages are measured with respect to this potential

³ A material becoming passive means that it is getting less affected or corroded by its environment

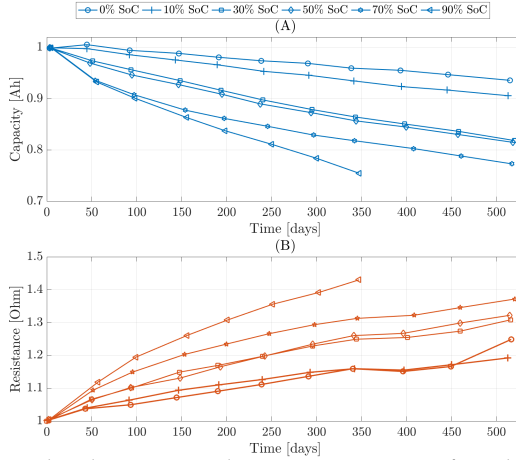


FIGURE 38: Normalized capacity and resistance over time for calendar degradation test of NMC cells performed at 50°C and various SoC [72]. Their results show a clear correlation with SoC, where higher storage level results in higher degradation rate.

KEY INSIGHTS ON THE EFFECT OF TIME

The effects of time on the calendar degradation of LIBs can be summarized as follows:

- SEI layer growth is reported as the main cause for the degradation rate following a $\sqrt{\text{time}}$ curve. Higher temperature and SoC result in a faster degradation rate.
- At lower SoC, the degradation of the cathode might be an explanation for the more linear decay of capacity.
- An initial increase in capacity is occasionally observed. Different explanations for this phenomenon are given in literature.

4.3.1.2 Temperature (Calendar)

The most critical stress factor for LIB degradation is temperature; all reaction rates, parasitic and non-parasitic, are related to temperature. It, therefore, affects all other stress factors.

MODELLING TECHNIQUES: TEMPERATURE (CALENDAR)

The most common semi-empirical technique to model the degradation due

to temperature is using the Arrhenius law [132, 141, 150, 154], given in Eq.(14). The Arrhenius law models the effect of temperature on chemical reaction rate.

$$k = A \exp \frac{-E_a}{RT} \quad (14)$$

Where,

- k is the reaction rate constant
- T is the absolute temperature
- A is the pre-exponential factor
- E_a is the activation energy
- R is the universal gas constant

The activation energy here refers to the additional energy required for a reaction to take place. The Arrhenius equation is often related to the rate of all parasitic side reactions leading to SEI growth [80] in LIB degradation research. Other models based on exponential or power-law relationships are also often utilized [94, 144].

LIMITATIONS & CHALLENGES: TEMPERATURE (CALENDAR)

Based on the summary of the testing conditions presented in Table 10 it is clear that the majority of the papers have investigated accelerated calendar degradation at elevated temperatures, ranging from 30°C-60°C. This is probably done to reduce the calendar life to a better manageable period. However, this raises the question of whether the degradation rate at 50°C-60°C is translatable to the degradation rate at 15°C-25°C. A rule of thumb is that the degradation rate doubles for every 10°C Celsius increase in temperature [72, 131, 144, 150, 154]. For studies using the Arrhenius law, this would result in an activation energy close to 50 kJ/mol. In some cases, this assumption is even used to derive the degradation model [155]. To test this hypothesis, the degradation data of the reviewed studies is sampled and analyzed according to Eq.(15).

$$\alpha = \frac{C(T_2)}{C(T_1)} \frac{10}{T_2 - T_1} \quad (15)$$

Here,

- $\frac{C(T_2)}{C(T_1)}$: the ratio of percentage capacity loss between temperatures.

- $T_{1,2}$: temperatures of samples 1 and 2.
- α : factor to test the hypothesis.

An α equal to 2 would indicate twice as much capacity degradation for every 10°C Celsius. Using Eq.(15) the data of each study is compared, only to cells from the same study, tested at the same SoC, and measured around the same time, such that only the temperature is variable. Figure 39 concludes that the given hypothesis often overestimates the calendar degradation, as the peak occurs at approximately $\alpha = 1.5$, which means that most tested cells increase degradation by 50% every 10°C . Further investigation did not show any other correlation between age or SoC.

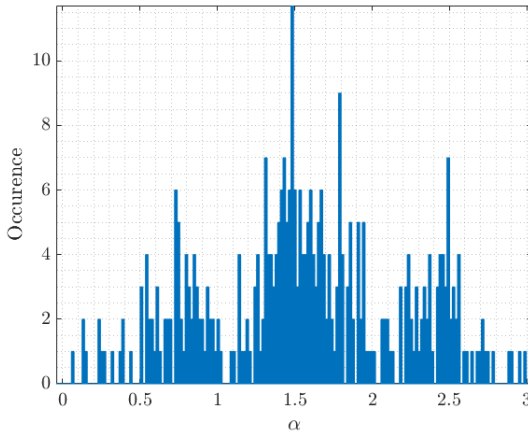


FIGURE 39: Found results for α of Eq.(15). In the tested studies, 60% of calculated values of α were below 2, and a peak around $\alpha = 1.5$ was observed, which means that most tested cells have an increased degradation rate of 50% for every 10° increase. The spread of values confirms the interdependency with other stress factors such as age and SoC, however, no clear correlation was found

Due to the complex nature of LIB degradation, it is challenging to give a rule of thumb figure as the degradation rate will always depend on multiple correlated factors. For this reason, the testing conditions, especially temperature, should be as close as possible to the operating conditions of the application, as extremely high temperatures result in different degradation mechanisms and therefore different degradation behaviour. An example of

this is shown in [144]. Here the authors show that for an NMC cell stored at a temperature of 60°C, the degradation rate increases tenfold when the cells are stored at 100% SoC compared to 20% SoC. In comparison, this difference at 30°C Celsius is negligible. A possible explanation could be the restructuring of the SEI layer as it starts to break down at higher temperatures, dissolves and re-precipitates. Furthermore, in [80] it is also reported that organic SEI products are changed into more stable inorganic products, thereby reducing the reaction rate but also reducing the ionic conductivity of the SEI and thus increasing the resistance.

KEY INSIGHTS ON THE EFFECT OF TEMPERATURE (CALENDAR)

The effects of temperature on the calendar degradation of LIBs can be summarized as follows:

- The Arrhenius law (or similar exponential forms) is the most common form of modelling the temperature dependency of calendar degradation.
- Temperature has a strong influence on all other stress factors and degradation mechanisms. To this extend, test conditions should be as close as possible to operating conditions in order to avoid modelling errors.

4.3.1.3 State-of-Charge (Calendar)

The last stress factor related to calendar degradation is the SoC (or analogously terminal voltage). Table 10 shows strong similarities between studies regarding testing conditions since most studies have modelled the effect of SoC based on three to four conditions.

MODELLING TECHNIQUES: SOC (CALENDAR)

In [138], the authors have modelled the SoC dependency as a polynomial function, where the interdependency of temperature and SoC is included by multiplication, as shown in Eqs.(16)-(18).

$$G(t) = A(T, SoC)e^{B(T, SoC)t} + Ce^{Dt} \quad (16)$$

with,

$$A(T, SoC) = a_1 \cdot SoC + a_2 \cdot T + a_3 \cdot SoC \cdot T \quad (17)$$

$$B(T, SoC) = b_1 \cdot SoC + b_2 \cdot T + b_3 \cdot SoC \cdot T \quad (18)$$

Here,

- $G(t)$: calendar degradation over time
- SoC: state of charge
- T : temperature
- $A(T, SoC), B(T, SoC)$: function to model temperature and SoC inter-dependency
- a_{1-3}, b_{1-3}, C, D : curve fit parameters

In [94, 156] calendar degradation is modelled as exponentially dependent on SoC, following Eq.(19).

$$A_{cal} = A_0 e^{\frac{SoC - SoC_0}{b}} \cdot A_0 e^{\frac{T - T_0}{c}} \sqrt{t} \quad (19)$$

Here,

- A_{cal} : calendar lifetime
- A_0 : specified calendar lifetime under conditions SoC_0 and T_0
- b, c : curve fit parameters

Eq.(20) shows how [130, 157–159] modelled the pre-exponential factor in the Arrhenius law to be SOC dependent. [130, 157] also model the activation energy to be dependent on SoC, as shown in Eq.(20).

$$Q_{loss}(t, T, SoC) = A e^{B \cdot SoC} \cdot e^{\frac{-E_a + C \cdot SoC}{kT}} t^z \quad (20)$$

here,

- Q_{loss} : lost charge
- A, B, C : curve fit parameters
- k : Gas constant
- T : temperature

In [132] the authors observed a linear increase for the SoC-dependent degradation. Therefore the kinetic dependency of (T, SoC) is modelled using an Arrhenius equation multiplied by SoC. The SoC dependency of calendar age-induced capacity degradation is modelled as a power-law relationship in [131, 137, 147, 154]. In contrast, the decrease in power capability is modelled in a linear relationship in [137].

Although diverse modelling methodologies are documented in the literature, the general trend suggests an increase in degradation with increasing SoC, especially at higher temperatures, [72, 144].

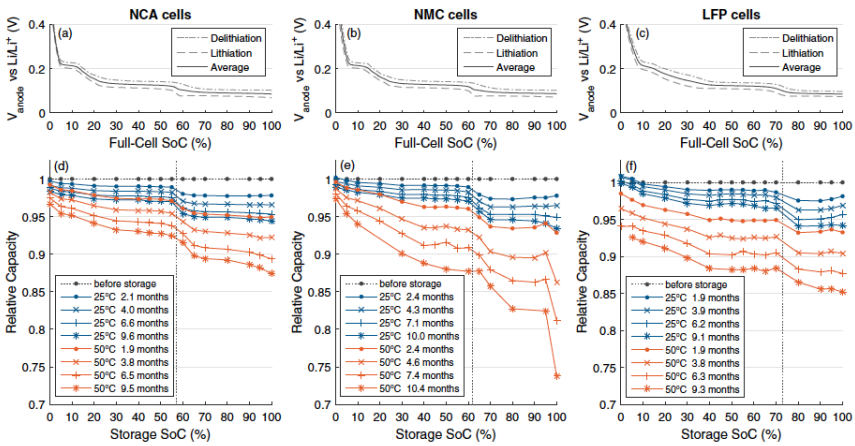


FIGURE 40: Graphite anode potential vs. SoC of three different half-cells. A strong correlation between anode potential and degradation rate is observed for all cells, especially the phase transformation around 60-70% marks a significant change in degradation rate. The figure is obtained from the publicly available material of P. Keil et al. in [97], under the Creative Commons Attribution 4.0 License CC-BY.

LIMITATIONS & CHALLENGES: SOC (CALENDAR)

Most reviewed studies only perform tests with three to four different SoC conditions due to practical constraints on testing capacity. This incorrectly leads to the belief that the rate of capacity and resistance deterioration for higher SoC's increases continuously. However, in [97, 154] calendar degradation was investigated with a higher resolution in SoC. Both these studies found a direct correlation between the graphite anode potential and capacity degradation.

In Figure 40 the results of [97] are shown for three different chemistries. As expected, an increase in storage temperature increases the capacity fading. However, more importantly, the results also show different plateaus with respect to storage SoC. There seems to be a direct correlation between the rate of capacity fading and the graphite anode stages for all three chemistries. These stages occur due to the different compositions of the lithium and carbon molecules, resulting in a different volume and potential. A schematic representation of the different stages, along with the anode potential during charge and discharge, is shown in Figure 41 [160].

The results of [97, 151] confirm that SEI growth results from electrochemical instability of the electrolyte-electrode interface. In both studies, these plateaus were not observed in the resistance increase. For the LFP cell this increased independently of SoC, whereas the rate of resistance increase for the NMC and NCA cells was found to be substantially larger at higher SoC, especially around 90-100%. The cathode surface film layer could be a possible explanation, which for LFP cells is much less SoC dependent due to the more stable crystal lattice and two-phase regime. Based on the results of [97, 154] it can be concluded that curve fitting the SoC dependency with only three test conditions is insufficient to accurately capture capacity fade as a function of SoC, as it will lead to significant under- and overestimations in certain SOC regions. The advantage, however, is that the anode potential can be determined prior to performing the degradation test. For example, the anode potential or differential voltage analysis (DVA) can be used. Once the anode potential is known, the choice of SoC testing conditions can be made strategically. Furthermore, knowing where the phase transition occurs during the operation of a LIB can help reduce calendar degradation.

Another observation on the results shown in Figure 40 is the drastically increased degradation at 100% SoC for the NMC chemistry. This was not observed in the other chemistries, and similar results have been found in other degradation studies of NMC cells [142, 144, 150, 154]. The increased degradation appears to be independent of anode potential. A possible explanation could be other degradation mechanisms driven by a high cell voltage, such as electrolyte oxidation, transition-metal dissolution, or structural damage to the cathode due to a high degree of lithiation [83, 161]. Due to the disproportionate increase in degradation at high temperature and very high SoC ($\geq 95\%$) it is not recommended to test NMC cells at 100% SoC, if the amount of testing conditions is limited as it will result in large overestimations for conditions below 95% SoC.

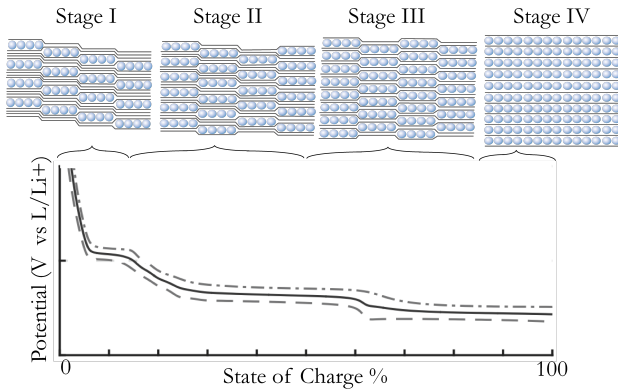


FIGURE 41: Schematic representation of the staging phenomena observed at the anode [160]. Because the arrangement of carbon and lithium molecules differs in each phase, each stage has a different potential and volume, and therefore a different degradation rate.

KEY INSIGHTS ON THE EFFECT OF SOC (CALENDAR DEGRADATION)

The effects of SoC on the calendar degradation of LIBs can be summarized as follows:

- The anode potential appears to be the main factor determining the rate of degradation in graphite-anode-based cells. This demonstrates that SEI layer growth is the dominant degradation mechanism for these cells.
- Modelers should be cautious when developing models based on a limited number of testing conditions. Because the degradation rate is determined by the anode potential, which is not a continuously changing potential but instead follows the stages determined by the anodes' phase transitions.
- A significant amount of studies testing NMC cells at 100% SoC, observed a disproportionate increase in degradation, for a slightly lower SoC. To this extent, higher accuracy over the entire SoC range can be achieved when the maximum SoC tested is 90-95%.

4.3.2 *Cyclic degradation*

Table 11 summarizes the cycling degradation studies and their testing conditions. The relevant part is discussed in the accompanying section for studies that discuss both calendar and cyclic degradation.

4.3.2.1 *Combining Cyclic and Calendar degradation*

Based on the reviewed studies, no single idea about the correlation between calendar and cyclic degradation can be derived. In [144], degradation is modelled using Dakin's approach. Here cyclic and calendar degradation are modelled to be multiplicative. The authors of [72, 80, 136, 143, 156] have mentioned that cycling results in additional (cyclic) degradation due to added mechanical stress and lithium plating. In most cases, such as [143], cyclic degradation is added on top of the previously calculated calendar degradation. Furthermore, various studies show that the SEI layer's growth and morphology alter according to the operating conditions. During cycling conditions, the SEI layer stays more porous, whereas a much denser layer is formed under storage conditions [104, 105, 154]. While cyclic and calendar degradation are mentioned to have a strong superposition for high temperatures or high SoC in [154, 166]. For milder conditions, especially at lower temperatures and increased C-rate, cycling degradation is probably dominant.

Note that studies that only discuss cyclic degradation have inherently incorporated calendar degradation as well. In this case, the superposition of calendar degradation is assumed to be non-existent [156, 183] or negligible compared to the cycling induced degradation. However, in these cases, the fast sequential cycling tests mask the effect of calendar degradation and, therefore, lead to estimation errors in applications with significantly more time between cycles. In practice, every modeller should determine the best practice for themselves, depending on their application and operating conditions.

4.3.2.2 *Addressing Irregular Cycles: Rainflow Counting Method*

Often, cyclic degradation studies are performed under fixed conditions. However, in reality, degradation is not as static as these test conditions. One way of dealing with highly irregular power profiles is using the rain flow counting method. Rainflow counting is a common fatigue analysis technique used to calculate the combined fatigue of a summation of different

Study	Chem.	Cap.	Res.	Factors	Conditions				
					Temp.	SoC	DoD	C-rate	Throughput
[152]	LFP	✓	x	SoC, DoD, C, Ah, T	25-40°C	30-70% (avg)	12.5-75%	1-1.82C	900 FEC
[131]	LFP	✓	✓	SoC, DoD, Ah, T	35-50°C	27.5-72.5% (avg)	10-60%	4C	1k-7k FEC
[162]	LFP	✓	x	DoD, C, T	-30-60°C	100% (start)	10-90%	0.5-10C	1k-6.5k FEC
[163]	LFP	✓	✓	DoD, T, C	-18-40°C	100% (start)	20-100%	1-15C	550-2900 FEC
[99]	LFP	✓	x	T, Ah, C	25°C	100% (start)	100%	0.5-5C	550 FEC
[155]	LFP	✓	x	T, Ah, C	25°C	100% (start)	100%	0.5-5C	1.2k-10k
[164]	LFP	✓	x	SoC, T, Ah, C	36-45°C	38.5-60% (avg)	100%	2.82-6C	4k-20k FEC
[165]	LFP	✓	✓	SoC, DoD, T, Ah	30, 45°C	1.25V-2V 3.65V-3.95V	100%	4C	200 FEC
[166]	LFP	✓	✓	DoD, Ah, C	30°C	100% (start)	5-100%	1-3.5C	2k-5.5k FEC
[167]	LFP	✓	x	SoC, Ah, C	55°C	0-30%	10-30%	4-8C	3.9k-12.5k
[168]	LFP	✓	x	C, T	25,45°C	100% (start)	100%	1C	4.5k FEC
[137]	LFP	✓	✓	SoC,DoD, T	35-50°C	10-90% (start)	10-80%	4C	8k
[136]	LFP	✓	✓	C, Ah,	25°C	40-80% (start)	3,6%	0.5-1C	-
[169]	LFP	✓	x	SoC,T,C,Ah	22.8°C - 51.6°C	100% (start)	60,100%	1-4C	654-4286 FEC
[170]	LFP	✓	✓	x	22.8°C - 51.6°C	100% (start)	60,100%	1-4C	654-4286 FEC
[159]	LFP	✓	x	T, C, Ah	40-50°C	60-85% (start)	20-65%	0.4-4C	4k
[100]	LFP	✓	x	SoC,DoD,T, Ah	20°C	75-100% (start)	50-75%	1C	4k-8k FEC
[171]	LFP	✓	✓	SoC, Ah,	5, 44°C	100% (start)	100%	1.5C	990 FEC
[100]	NMC	✓	x	SoC,DoD,T, Ah	20°C	75-100% (start)	50-75%	1C	4k-8k FEC
[171]	NMC	✓	✓	SoC, Ah,	5, 44°C	100% (start)	100%	1.5C	990 FEC
[72]	NMC	✓	✓	SoC, DoD, Ah, T	35°C	10-95% (avg.)	5-100%	1C	1.5-4.5k FEC
[144]	NMC	✓	✓	DoD, Ah, T, C	40,50°C	100% (start)	20-40%	10,20C	-
[142]	NMC	✓	x	SoC, DoD, C, T	-10-50°C	20-80% (avg.)	10-100%	1/3-2C	900-1k FEC
[172]	NMC	✓	x	SoC, T, Ah, C	10-45°C	100% (start)	55-75%	1/3-5C	800-1400 FEC
[151]	NMC	✓	✓	SoC, T, Ah, C	10-45°C	40-70% (avg)	20%	5-20C	-
[173]	NMC	✓	x	SoC, T, Ah, C	10-46°C	100% (start)	50%	0.5-6.5C	1.3k-1.7k FEC
[143]	NMC	✓	x	T, Ah, C	10-46°C	100% (start)	10-90%	0.5-6.5C	900-4.3k FEC
[150]	NMC	✓	✓	SoC, DoD, T, Ah, C	40°C	5-90% (avg)	10,60%	1C	2k FEC
[140]	NMC-LMO	✓	✓	SoC, T	30-50°C	100% (start)	10-70%	4C	-
[159]	NCA	✓	x	T, C, Ah	40-50°C	60-85% (start)	20-65%	18C	4k

Study	Chem.	Cap.	Res.	Factors	Conditions				
					Temp.	SoC	DoD	C-rate	Throughput
[144]	NCA	✓	✓	DoD, Ah, T, C	40,50°C	100% (start)	20-40%	9,16C	-
[174]	NCA	✓	✓	SoC, DoD, Ah, T	20°C	EOCV: 3.9V-4.1V	20-80%	9,16C	-
[175]	NCA	✓	x	SoC, DoD, T	20°C	80,100% (start)	60-80%	-	782 FEC
[176]	NCA	✓	x	DoD, T, Ah, C	0-50°C	EEODV: 2.4-2.5V EOCV: 4.1-4.3V	60-80%	0.2-1C	782 FEC
[100]	LMO	✓	x	SoC,DoD,T, Ah	20°C	75-100% (start)	50-75%	1C	4k-8k FEC
[171]	LMO	✓	✓	SoC, Ah,	5, 44°C	100% (start)	100%	1.5C	990 FEC
[158]	LMO	✓	x	SoC, T,	25°C	35-50% (avg.)	20-95%	1C	900 FEC
[177]	LMO	✓	x	Ah	25°C	100% (start)	100%	1C	700 FEC
[178]	LMO	✓	x	DoD, T, C	20-50°C	100% (start)	20-100%	1-5C	900 FEC
[179]	LCO	✓	x	SoC, DoD, T, C	25°C	EOCV: 4.1V-4.3V	100%	0.5-1.4C	900 FEC
[180]	LCO	✓	x	DoD, T, Ah, C	25-45°C	100% (start)	20-30%	0.6-1.2C	500-800 FEC
[147]	LCO	✓	x	SoC, DoD, T	0-60°C	0-100% (start)	3-80%	1/5C	10k FEC
[181]	LCO	✓	x	Ah, C	-	100% (start)	100%	0.5-1C	550 FEC
[182]	LCO	✓	x	SoC, C	25°C	EOCV: 4.2-4.35	100%	1C	250-500 FEC

TABLE 11: Overview of studies investigating empirical and semi-empirical cycle life models (Part 2).

stress cycles. Several studies have used the rain flow counting method to calculate the combined degradation of an irregular power profile [100, 131, 152, 184, 185]. An example of this is shown in Figure 42. Here the rainflow matrix is shown for a randomly generated load profile, which shows the amount of cycles of a particular current rate [A] and throughput [A*s]. Other output quantities could be DoD, average SoC, or idle time. Next, the degradation can be determined based on the number of cycles with a specific amount of stress. The advantage of this technique is that it allows assessing the degradation of irregular profiles more accurately. However, it assumes that the sequence of cycles does not influence the outcome, e.g. the degradation due to a high DoD cycle followed by a low DoD cycle is similar to a low DoD cycle followed by a high DoD cycle. Furthermore, it assumes that the effect of a particular cycle (or sum of cycles) is independent of the current age of the battery. Interested readers are directed to [186] for more information on the rain flow counting technique.

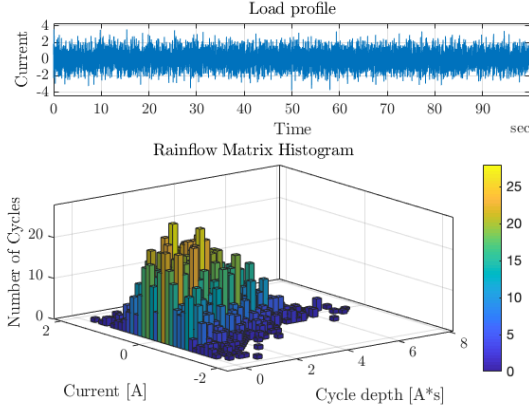


FIGURE 42: Example of a rainflow matrix histogram based on a randomly generated load profile. In this case, the rainflow matrix counts the number of cycles of a specific cycle-depth with a specific current load.

4.3.2.3 Throughput

Throughput describes the net Ah delivered by the battery over multiple cycles. As a result, it is one of the critical stress factors for cycling degradation.

MODELLING TECHNIQUES: THROUGHPUT

Similar to time for calendar degradation, the relationship for throughput is often modelled using a power-law relationship [72, 99, 159, 162, 164], as described in Eq.(21) or Eq.(22). Furthermore, throughput is also modelled in terms of number of cycles combined with depth-of-discharge. Often with similar power-law equations [131, 142].

$$Q_{cycl} = f(SoC, T, DoD, I) Ah^z \quad (21)$$

$$Q_{cycl} = f(SoC, T, DoD, I) N_{cycle}^z \quad (22)$$

Where,

- $f(SoC, T, DoD, I)$: degradation due other stress factors.
- Ah : the total cumulative throughput of the cell.
- N_{cycle} : the amount of performed cycles, sometimes expressed in terms of depth-of-discharge.

- z : power-law exponent.

The typical values of z are in the range of 0.5-0.8, which is generally associated with SEI layer growth. The authors of [72], found the best fit for z around 0.5, after subtracting calendar degradation. Meaning that as the battery ages, the SEI thickens, and the capacity fade due to cycling induced stress on the SEI decreases. In [180] values of z in the range of 0.8 have been reported, following a less logarithmic and more linear degradation rate. A possible explanation could be an increased share of cathode surface layer film growth [151]. In [167], the authors found the best curve fit using $z = 1.23$. Here the degradation due to the charge-sustaining (CS) mode of plug-in hybrid electric vehicles (PHEV) has been investigated. Here the CS mode of a PHEV was characterized by low SoC and very high C-rates. The resulting degradation showed an increasing degradation rate, resulting in an exponential factor $z > 1$. Because of the low SoC, combined with the high C-rate, this increasing degradation rate is potentially dominated by metallic lithium plating, which in contrast to SEI growth, is a self-reinforcing process.

However, not all studies have reported non-linear cyclic degradation characteristics. In [152, 155] the cyclic degradation is modelled as linearly increasing with throughput, even though the results show a very slight saturation. Furthermore, in [175] cycling degradation is assumed to be linearly dependent on the number of cycles. This is, however, not confirmed by the experimental data shown in the paper. Finally, the authors of [104] have found a linear correlation between cycling induced capacity fade and the number of cycles (on top of a $t^{0.5}$ time dependency). A destructive physical analysis showed that damage to the cathodes' active material was the leading cause for the cycle induced degradation. Additionally, the authors of [104] observed a linear increase in resistance, whereas the capacity fading showed a $t^{0.5}$ correlation. This indicates that the degradation mechanisms between capacity fade and resistance increase are different [72]. This difference between capacity and resistance deterioration was found in several studies [131, 154, 163, 172]. Unfortunately, no explicit explanation for this observation was given.

LIMITATIONS & CHALLENGES: THROUGHPUT

For studies investigating only cyclic degradation [131, 158, 162, 164, 172], it could be argued that the superposition of calendar degradation has a strong effect on their results, especially at higher temperatures and SoC. According to [162, 180], time is inherently incorporated in throughput, as

every charging instance with a particular C-rate is also a function of time. However, this is only valid if the cell is cycled continuously, which is rarely the case in practical applications.

Most of the above-described studies use some form of the Arrhenius equation, combined with a power-law relationship on throughput or number of cycles. This form of modelling is generally well suited to predict degradation due to long term storage or cycling during a post-process calculation. However, for online calculations over a shorter period, or fast-changing operating conditions, it is less suited as the current age of the battery is not taken into account at every new iteration/calculation. This has been resolved by the authors of [159] by differentiating the Arrhenius/Power-Law over time. Starting with Eq.(23), this results in the linearized form as shown in Eq.(23)-(25) [159].

$$Q_{loss} = B(I) \exp \frac{-E_a + \alpha|I|}{RT} Ah^z \quad (23)$$

$$\frac{Q_{loss}}{dt} = f(I, T) \left(\frac{Q_{loss}}{B(I) \exp \frac{-E_a + \alpha|I|}{RT}} \right)^{1-\frac{1}{z}} \quad (24)$$

$$f(I, T) = \frac{|I|}{3600} z B(I) \exp \frac{-E_a + \alpha|I|}{RT} \quad (25)$$

Another limitation of the Arrhenius/power law is that it only captures the degradation in the first stages of battery life, during which the degradation rate decreases as the battery ages. However, at a certain age, all LIBs experience an increase in degradation rate due to lithium plating, as shown in Figure 36. The authors of [142] model this inflexion point as a polynomial equation based on the number of cycles and DoD, according to Eq.(26). Figure 43 shows that this results in a good fit on their degradation data, and shows the inflexion points which start to occur around 3000 cycles. However, note that this is not observed in the data, and therefore the age at which plating starts to occur remains unknown.

$$RCD(x, y) = \sum_{i=0, j=0}^{n, m} a_i x^i + b_j y^j \quad (26)$$

Where:

- *RCD*: Relative capacity degradation (%)
- *x*: full equivalent cycle number

- y : DoD (%)
- a_i : constants for x
- b_j : constants for y
- n, m : order of x, y

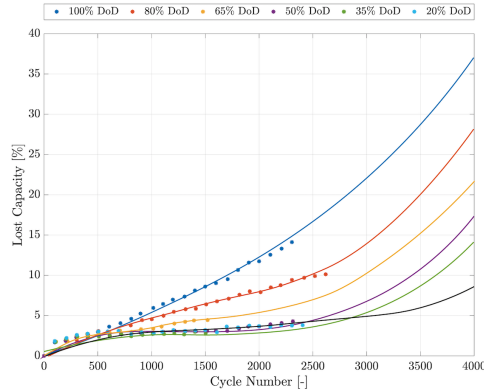


FIGURE 43: degradation and fitting result from [142]. In contrast to many exponential models this polynomial model takes into account the increasing degradation rate at later point in battery life, due to lithium plating.

Another option is to linearise the various stages seen in LIB life, such as done in [100]. Here the authors distinguish between four different stages, each modelled as linear functions dependent on various stress factors, see Figure 44.

KEY INSIGHTS ON THE EFFECT OF THROUGHPUT

The most important insights on the effect of throughput can be summarized as follows:

- Often an Ah^z relationship, with $0.5 \leq z \leq 1$, is found for studies modelling the effect of throughput on cyclic degradation. Even though this may result in good accuracy in the first stages of battery life, it fails to capture the degradation in later stages, where an increased degradation rate is generally observed after an inflexion point.
- Studies investigating only cyclic degradation inherently include the effects of calendar degradation in their models. Depending on the

application of the model, this can potentially lead to inaccurate results. Other studies have subtracted the expected amount of calendar degradation from their cyclic degradation test results to more accurately curve the degradation due to cycling.

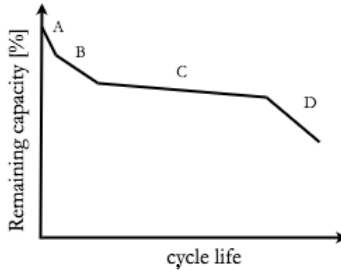


FIGURE 44: Modelling battery degradation based on four different linear stages (stages (A)-(D)), this allows to linearize the degradation model over the entire lifetime of the battery [100]

4.3.2.4 Temperature

MODELLING TECHNIQUES: TEMPERATURE (CYCLIC)

Also for cycling degradation the Arrhenius law [72, 99, 100, 142, 150, 162], or similar exponential relationships [131, 144, 155], are most often used to model the temperature dependent reaction rate. An example of an Arrhenius law model is given in Eq.(23). Also polynomial relationships, such as the example given in Eq.(27) and (28), are occasionally used [143].

$$Q_{loss} = B_1(T)e^{B_2(T)I_{rate}Ah} \quad (27)$$

with,

$$B_1(T) = aT^2 + bT + c, \quad \& \quad B_2(T) = dT + e \quad (28)$$

where:

- Q_{loss} : Lost capacity.
- T : Temperature.
- I_{rate} : C-rate.
- Ah : Throughput.
- a, b, c, d, e : curve fit parameters.

LIMITATIONS & CHALLENGES: TEMPERATURE (CYCLIC)

In the studies mentioned above, good accuracies are achieved when using the Arrhenius law to model the temperature dependency at temperatures above room temperature. However, different to calendar degradation, the Arrhenius law is not a good indicator for the temperature-dependent degradation rate at temperatures below room temperature [100, 144, 152] (and occasionally also at higher temperature rates [180]). Where for calendar degradation, lower temperatures reduce the reaction rate of parasitic side reactions, under cycling conditions, the lower temperatures also reduce the battery's ionic conductivity, leading to an increased impedance and reduced performance [187–189].

In [152, 190] a temperature around a 20 – 25°C was found to be the dividing limit at which the impedance starts increasing for lower temperatures, and above which the impedance decreases for lower temperatures. As a result, the least (cyclic) degradation is generally observed at around 20 – 25°C [142, 144, 152, 162, 163]. An example of this is shown in Figure 45, where the pre-exponential and exponential factors $B_1(T)$ and $B_2(T)$ from Eq.(27)((28)) are shown [143]. Therefore, cycling degradation models utilizing exponen-

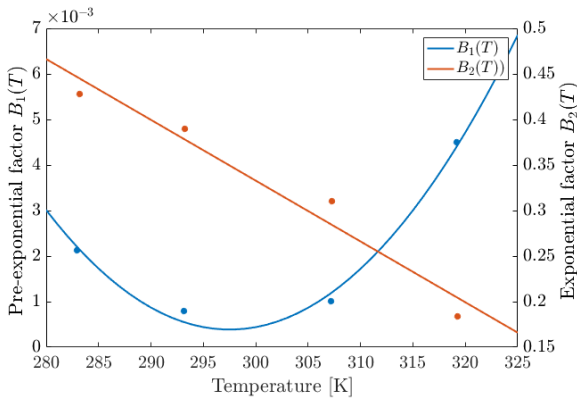


FIGURE 45: The pre-exponential and exponential factors $B_1(T)$ and $B_2(T)$ from Eq.(27) show that the lowest degradation rate is observed for temperatures around room temperature. Additionally, a decreasing $B_2(T)$ shows that the effect of current rate decreases at higher temperatures. The shown results are obtained for NMC-LMO cells cycled at 50% DoD and 1C.

tial relationships, fitted on test results above room temperature, can often not be used for conditions below a 20°C as this would result in severe un-

derestimations. Nevertheless, the Arrhenius law can also be used at lower temperatures if combined with positive activation energy. An example obtained from [176, 191] is shown in Eq.(29).

$$Q_{loss} = A_L e^{\frac{E_L}{RT}} + A_H e^{\frac{-E_H}{RT}} \quad (29)$$

Here, the letters H and L denote the found parameters for high and low temperatures.

In [190] the authors showed, using post-mortem analysis, that different degradation mechanisms are dominant above and below 20°C for an NMC-LMO blended cathode cell. Their results show that lithium plating is the dominant degradation mechanism at low temperatures, caused by an increasing polarization near the electrode due to the slow diffusion and low ionic conductivity [105]. Whereas at higher temperatures, transition metal dissolution and SEI growth are the dominant degradation mechanisms. Similar results have been found in [192] for LCO cells.

A couple of studies have even performed degradation tests at subzero temperatures. However, most of them have not included these results in their models due to the extremely short cycle life (below 100 equivalent full cycles) [105, 142, 152, 162]. [188] Showed that the anode's diffusion rate is the main limiting factor at temperatures below zero. At temperatures above 20°C, the intercalation potential of graphite anodes often prevents lithium plating [192], until a certain age. At higher temperatures, active material loss and SEI growth are dominant [120, 138]. Especially, cathode chemistries containing manganese are sensitive to higher temperatures (and higher SoC) due to Mn-dissolution.

Not only the effect of temperature changes around 20 – 25°C, also the interdependency of temperature with other stress factors such as C-rate. At higher temperatures, the impact of C-rates becomes less significant, as shown in Figure 45, and the effect of calendar degradation becomes more pronounced [144]. Whereas for lower temperatures, the detrimental effect of C-rate increases [143, 144]. More on this is discussed in the next section.

KEY INSIGHTS ON THE EFFECT OF TEMPERATURE (CYCLIC)

The most important insights on the effect of temperature can be summarized as follows:

- The majority of papers model the degradation rate to be exponentially dependent on temperature.

- Temperatures around 20 – 25°C are a tipping point below which a lower temperature increases the impedance and above which higher temperature increases the battery's impedance.
- As a result, models utilizing an exponential relationship to model the temperature dependency for cells cycled above room temperature might lead to significant underestimations when used for temperatures below room temperature. A possible solution could be to use both a positive and negative activation energy (or exponential factor).

4.3.2.5 C-rate

C-rate or the rate of (dis)charge is defined as the ratio of power (W) to energy capacity (Wh). Generally, higher C-rates are believed to be more detrimental to battery degradation. This has been confirmed in the majority of the reviewed studies, for C-rates above 2-3C. In [193] the authors cycled LCO cells with 1, 2, and 3C at room temperature. Using an electron microscope and impedance analysis, they showed that the increasing C-rates caused structural damage on the graphite anode of an LCO cell, resulting in the crack and repair of the SEI layer. The rate of capacity and resistance degradation was proportional to the C-rate. Similar results were found in [179, 180].

MODELLING TECHNIQUES: C-RATE

In [143, 144, 163, 164, 173], among other studies, the authors modelled an exponential increase in degradation with respect to C-rate, often combined with an Arrhenius like equation, where the activation energy (or in general the exponential component) is modelled as a linear function of C-rate as shown in Eq.(23) [159]. Others also included a linear dependency on C-rate in the pre-exponential factor [173, 180], as shown in Eq.(30).

$$Q_{loss} = A(C)e^{-\frac{E_a(C)}{RT}} n^{0.74} \quad (30)$$

with:

$$A(C) = e^{aC^2 + bC + c} \quad (31)$$

$$E_a(C) = xe^{yC} + z \quad (32)$$

where:

- Q_{loss} : Lost capacity.

- T : Temperature.
- C : C-rate.
- Ah : Number of cycles.
- a, b, c, x, y, z : curve fit parameters.

The authors of [152, 155] inherently incorporated C-rate by using the normalized standard deviation in SoC ($SoC_{dev}(t)$) per time unit, as shown in Eq.(33)(34)

$$Q_{loss} = k_1 SoC_{dev} \exp k_2 SoC_{avg} + k_3 \exp k_4 SoC_{dev} \quad (33)$$

Where,

$$SoC_{dev} = \sqrt{\frac{3}{\Delta Ah_m} \int_A h_{m-1}^{Ah_m} (SoC(Ah) - SoC_{avg})^2 dAh} \quad (34)$$

Where,

- SoC_{dev} : the normalized deviation in SoC
- SoC_{avg} : the average SoC of a cycle.
- ΔAh_m : the amount of charge processed in cycle m .
- k_{1-4} : curve fit constants.

A different approach was taken in [164] (LFP), for C-rates of 2, 20 and 28C at temperatures above 36°C. The authors model the effect of C-rate to be more detrimental than temperature and SOC. Furthermore, according to their model, the impact of C-rate increases at higher temperatures. However, no accompanying data is shown to verify this. Note that the effect of cell self-heating becomes very significant at these C-rates, leading to increased calendar degradation due to significantly elevated cell temperature. Some authors even neglect the effect of C-rate, as it is incorporated in the temperature dependency [100]. This might be a valid assumption for lower C-rates, but for very high C-rates, the effect of mechanical and kinetic stress might be non-negligible.

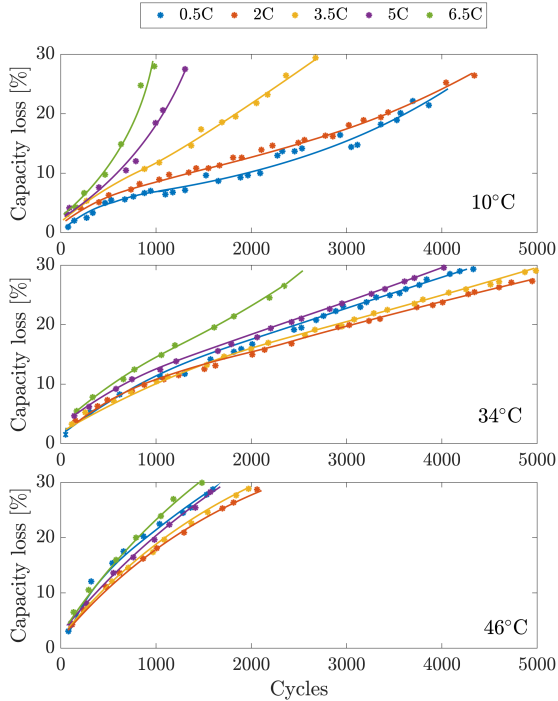


FIGURE 46: Cycling degradation results of the NMC studies in [143]. The results show the interdependency of C-rate and temperature. At temperatures of 34°C and 46°C the effect of C-rate decreases and the least degradation is observed for 2C and 3.5C.

LIMITATIONS & CHALLENGES: C-RATE

Before discussing any limitations and challenges regarding C-rate dependent degradation, the differences between chemistries should be pointed out. LFP cells, for example, are well-known for their ability to handle large amounts of power. Furthermore, LIBs using LTO anodes can sustain extremely high C-rates with negligible degradation. However, when conducting cyclic degradation tests, readers and modellers should be aware of the effect of energy density on C-rate. As for the same cell size, with each equal electrode surface area, higher current densities are experienced for cells with a higher energy density for the same C-rate, potentially leading to an unfair comparison between cell chemistries [97].

Although most of the reviewed studies found an exponentially increasing degradation rate at C-rates above 2C, a significant part found a negligible increase in degradation for C-rates below 2C and temperatures between 30 – 45°C, for both LFP and NMC chemistries [105, 142, 152, 162, 166, 172, 173, 178]. In [105] the increase in C-rate from 1C to 2C was found negligible at 45°, but non-negligible at 20°C. Showing the temperature dependency on C-rate. The authors report that the increased reaction rate and ion diffusion kinetics at these temperatures might reduce the stress caused by an increasing C-rate.

To this extend, to adequately explain the effect of C-rate, a distinction between above and below room temperature should be made. At lower temperatures, the ionic conductivity and intercalation rate decreases [162], whereas the higher current density as a result of higher C-rate requires faster diffusion kinetics [105]. As a result, lower temperatures accelerate the detrimental effects of increasing C-rate, resulting in increased mechanical and kinetic stress on the electrodes and an increasing polarization gradient, potentially leading to lithium plating [194]. Similarly, the effect of C-rate often decreases for increasing temperatures, as was found by the authors of [143]. Their results are shown in Figure 46. At 10°C it shows a clear dependency on C-rate, whereas for an ambient temperature of 34°C and 43°C the difference between C-rates decreased. Also, the capacity retention trajectory is distinctly different at 10°C and higher C-rates, pointing to an increasing rate of lithium plating. Finally, it is also noteworthy that the least degradation is not necessarily observed at the lowest C-rates.⁴ Nevertheless, also at higher temperatures, the effect of C-rate can cause detrimental effects such as crack propagation of the SEI layer, cathode overcharge (as a result of an increasing polarization gradient), or structural damage to the anode and cathode such as graphite exfoliation [90, 195–197].

Some authors have accounted for the interdependency between C-rate and temperature. In [144] NMC and NCA cells were cycled at temperatures of 40 – 50°C and C-rates of 10 and 20C. The authors found an exponentially increasing degradation rate for higher C-rates. However, decreasing at higher temperatures. Therefore the temperature-dependent C-rate effect

⁴ More studies report less degradation at higher C-rates. In [166] (NMC), at 60% DoD the least degradation was observed for 3.5C, followed by 1C than 2C. Whereas at 100% DoD no difference was observed between 1C and 2C, and only a small difference was observed for cells tested with 10% DoD. All cycling tests were performed at 30°C. A complex correlation between C-rate and DoD was found; the authors mention that further investigation is required to determine this correlation

was modelled as a linear function of temperature, as shown in Eq.(35). Similar methods have been used in [143].

$$k_C = \exp(a(T)I) \quad (35)$$

Where,

- k_C : C-rate induced cyclic degradation.
- $a(T)$: Linear expression to describe temperature dependency of C-rate.
- I : C-rate.

KEY INSIGHTS ON C-RATE

From the above-described results, several conclusions can be drawn:

- The effect of C-rate is often modelled to be exponentially dependent.
- A strong interdependency with temperature is observed. Therefore, models obtained using temperatures above 20° are likely not to be valid at temperatures below this threshold due to an increasing impedance.
- For temperatures above 20°, the effect of C-rate decreases. Some studies even report less degradation is observed at higher temperatures or higher C-rates. Modelling C-rate as a temperature-dependent function can therefore increase accuracy.
- When performing cycling tests at very high C-rates, cell self-heating should be taken into account.
- Readers and modellers should be cautious when using exponential relationships with respect to C-rate, at C-rates below 2. Several studies have shown that this relationship is not valid for C-rates below the 2C threshold.

4.3.2.6 State of Charge (Cyclic)

Table 11 demonstrates that a considerable amount of studies did not investigate the effect of SoC on cyclic degradation, but instead always start their cycle at 100%. These studies are likely to have a larger calendar degradation superposition. Additionally, users should check whether this is suitable for their application, as battery management systems do not always charge

the cells up to this point. The reviewed studies are divided into two categories: 1. Studies investigating the influence on End-of-Charge-Voltage and 2. Studies investigating the influence of average SoC.

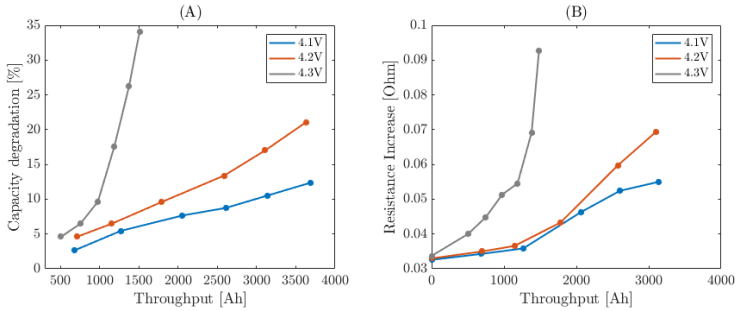


FIGURE 47: Comparison of the capacity degradation (A) and resistance increase (B) of LCO cells tested at 1C, 25°C and various EOCV. significant increase in degradation is observed for the cells cycled up to 4.3V, and therefore too high EOCV should be avoided. Based on data obtained from [179]

MODELLING TECHNIQUES: END-OF-CHARGE-VOLTAGE

The final voltage at which the battery is maintained during the constant voltage (CV) charging region is the End-Of-Charge-Voltage (EOCV). In [193] it was found that 90% of cycling losses resulted from the CV charging region. In [165, 174, 176, 179, 182] the effect of end-of-charge-voltage (EOCV), was investigated for LFP, LCO, and NCA chemistries. In these studies the EOCV ranged from 4.1V to 4.3V and all studies concluded that a higher EOCV lead to increased degradation. According to the authors of [176], a high cell voltage causes a higher potential in the cathode and a lower potential in the anode, which increases the electrolyte oxidation and reduction rates at the cathode and anode, respectively, resulting in surface film layer formation. Furthermore, in [179], a significant increase in degradation was found with an EOCV of 4.3V, compared to 4.1V and 4.2V, respectively. The results of [179] are shown in Figure 47. Based on a differential voltage analysis, the authors conclude that lithium plating is the cause of the increased degradation rate. At this very end of the charging process, the reduced diffusion capability of lithium into the graphite anode is said to cause lithium plating.

All of the above mentioned studies use different methods to model the degradation due the EOCV or EODV (End-Of-Discharge-Voltage). In [165], the authors develop an degradation model based on the addition of multiple single factor stress models. The total cycle life CL is calculated according to Eq.(36).

$$CL = \frac{1}{SSF_0} \left(\frac{1}{SSF_T} + \frac{1}{SSF_{I_d}} + \frac{1}{av_{EODV}^{-b}} + \frac{1}{SSF_{I_c}} + \frac{1}{cv_{EOCV}^{-d}} \right) \quad (36)$$

where:

- CL : total cycle life.
- SSF_x : Single stress factor model of x , where $x = I_d, I_c$; charge and discharge current rates.
- a, b, c, d : curve fit parameters

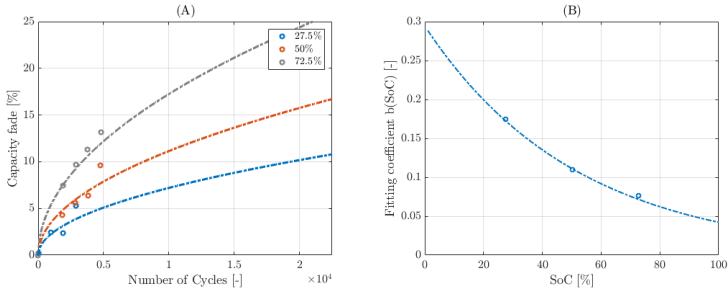


FIGURE 48: (A): degradation results for three different cells cycled with 35% DoD, 4C at 42.5°C around an average SoC of 27.5%, 50% and 72.5%. (B): Curve fitting coefficient $b(SoC)$ in eq.(37) for the three different degradation tests. Based on data obtained from [131].

MODELLING TECHNIQUES: AVERAGE SOC

Other studies have investigated the effect of different starting or average SoC. In [131] three different average SoCs were investigated, 27.5%, 50% and 72.5%, all cycled with 35% DoD, 4C. Their results shown in Figure 48, show an increasing degradation rate for lower SoC, modelled as inversely exponentially dependent on SoC, as given in Eq.(37).

$$b(SoC) = 0.2943 \exp(-0.01943SoC) \quad (37)$$

This increasing degradation rate at lower SoC can be explained by the fact that the impedance of the cell increases as the cell is discharged [xu59, 80, 193]. This results in reduced power capabilities and more self-heating. This is also temperature-dependent, and higher C-rates might aggravate its effect.

In [172] the effect of minimum SoC on various CS cycles for plug-in hybrid electric vehicles was tested on NMC-LMO cells at 30°C, 25-45% minimum SoC with varying C-rate. Their results show an exponentially increasing degradation at higher SoCs. Similar results are found in [152] for LFP cells cycled at 1-1.8C, 30°C. In both [152, 172] the calendar degradation was not subtracted, which might be a possible explanation for their results. In [164] a very slight increase in degradation was observed at higher SoC for cells cycled with a C-rate of 10C, whereas for lower temperatures and lower C-rates, the effect of SoC was found negligible. The authors followed an Arrhenius equation, where the degradation was linearly dependent on SoC, as shown in Eq.(38).

$$Q_{loss} = (\alpha SoC + \beta) \exp \frac{-E_a + \eta I}{R(273.15. + T)} Ah^z \quad (38)$$

The authors of [72] cycled NMC cells with various DoD at 1C, 35°C, and subtracted the expected calendar degradation results from their cycling degradation results. The resulting data showed the lowest degradation around an average SoC of 50%. Similar results were found in [142, 154].

LIMITATIONS & CHALLENGES: SOC (CYCLIC)

Concerning the effect of EOCV, a consensus exists that a higher EOCV leads to increased degradation. However, at these high SoC levels, battery chargers charge with a decreasing average current to maintain a constant voltage instead of constant current charging in the majority of the SoC range. Therefore, the effect of EOCV might be attributed primarily to calendar degradation mechanisms.

Less consensus on the effect of average SoC on LIB degradation is observed. Partially due to the influence of other parameters such as temperature, DoD, C-rate, and chemistry. But also due to the other mechanical and kinetic changes inside the cell. Such as an increased impedance at lower SoC, and volume changes due to the different electrode intercalation compounds [198, 199], as shown in Figure 41. In [198], the authors analyzed five NCA cells each cycled with 20% DoD around evenly distributed SoC intervals. The highest degradation was observed for the cells cycled in stage 2 (see Figure 41).

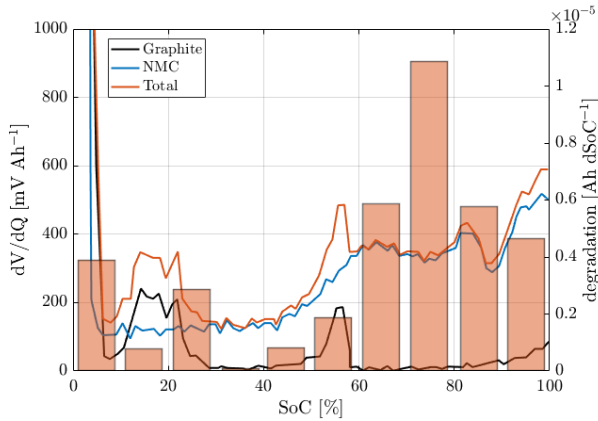


FIGURE 49: (left): Differential voltage analysis of an NMC cell, and (right): the degradation rate of cycles with 10% DoD for 10 different SoC intervals. The orange bars illustrate the strong SoC dependency on the effect of DoD. The most degradation is observed at the place where the anode potential is the lowest or where there is a phase transition at the anode. These cells are cycled with 10% DoD, 1C, 45°C, around 10 different SoC regions. Based on data obtained from [105]

A similar investigation was done in [105], where 10% DoD cycles are spread out evenly over the entire SoC range. The results are shown in Figure 49, and are in line with what was found in [198]. Here the bars show the total degradation per SoC range, whereas the lines show the DVA of both electrodes and the complete cell. However, the results of Figure 49 oppose their results for cells cycled with a DOD of 50%, which showed the least degradation with an average SoC 75%. This shows that SoC and DoD's effect have strong interdependencies that are hard to capture in empirical degradation models, as the effect will always be different depending on the starting point and cycle depth. Aside from a high interdependence, testing for only a limited amount of time or cycles may also lead to false conclusions on total lifetime, as was demonstrated in [105]. Here, NMC cells were tested around 25-75% SoC with 1C at 20°C. In the first 300 full equivalent cycles (FEC), the most degradation was observed at the highest SoC. Nevertheless, the highest cycle lifetime was observed at the highest average SoC as well. Further investigation showed that a more stable SEI is formed at higher cell voltages, whereas the SEI formed at lower cell voltages evolves to be more porous. Especially the SEI formed in the CV

region is said to better protect the anode material from the electrolyte. As a result, longer cycle life's were observed for higher cell voltages.

KEY INSIGHTS ON SOC (CYCLIC)

The following key insights can be summarized based on the above review:

- A higher EOCV results in increased degradation; due to the reduced current rate in the CV region, this is expected to be due to increased calendar degradation.
- The effect of SoC is strongly dependent on other operating conditions, such as C-rate, temperature and DoD. More specifically, cells tested at low C-rates, higher voltages, and higher temperatures are likely to have a significant calendar degradation superposition, resulting in less degradation at lower SoC. In contrast, cells cycled with higher C-rates or higher DoD appear to be more affected by the lower impedance at lower SoC. Probably having a higher cycle life when cycled around 50% SoC.
- A fast initial decrease in capacity due to high cell voltages does not necessarily have to result in a reduced lifetime, as higher cell voltages may lead to a more stable SEI layer.

4.3.2.7 *Depth-of-Discharge*

The final stress factor to be discussed is the DoD, sometimes also called cycle depth⁵. In this study, DoD is defined as the percentage of extracted charge with respect to the maximum available amount of charge. A usual rule of thumb is that an increasing DoD reduces the cycle lifetime [80, 137, 163]. However, as will be discussed, this is not valid for all reviewed studies. Generally, two different testing approaches exist to determine the detrimental effect of DoD: 1. starting from 100% SoC, or 2. cycling around a mean SoC. Both methods are limited because the starting point of the cycle determines the corresponding effect of DoD, as discussed in the previous section. Depending on the application of the model, one of the two methods can be preferred.

⁵ Existing DoD definitions in the literature are contradictory, and at least four conflicting definitions are used, namely 1) the inverse of the SoC, 2) the energy discharged from the battery compared to 100% SoC, 3) the full cycle consisting of one equal discharging and charging event or 4) the half-cycle consisting of one charging or discharging event [200]

MODELLING TECHNIQUES: DOD

An often found correlation between DoD and degradation follows the Wöhler curve, also known as the S-N curve or Palmgren-Miner rule [85]. Originating from mechanical stress in railway-engineering, this curve describes an objects lifetime, expressed in terms of the number of cycles (N) and cyclic stress (S) [151]. For LIB degradation, it is frequently used to describe the battery cycle-life as a function of DoD. Here the degradation rate decreases as the DoD increases. Various papers have found good correlation with this dependency [104, 131, 137, 155, 156, 163, 175]. Some of their results are shown in Figures 60(a)-(b).

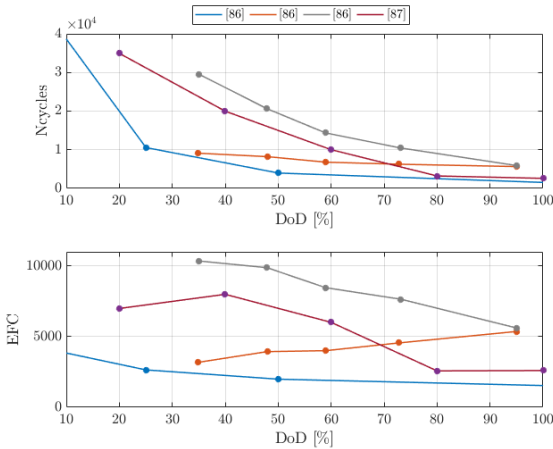


FIGURE 50: Comparison of the effect of DoD in two different studies. Top figure: DoD versus cycles (a), and bottom figure versus full equivalent cycles (b). Even though many studies find a good correlation with the Wöhler curve in terms of number of cycles, in terms of total charge throughput cycle life does not necessarily decrease for higher DoD.

When plotted as a function of number of cycles, a good correlation with the Wöhler curve is observed. However, when plotted as a function of full equivalent cycles, this behaviour is not always seen. Therefore in terms of total charge throughput, cycle life does not necessarily have to decrease for a higher DoD.

Based on the Wöhler curve, several studies have modelled the degradation to be exponentially dependent on DoD [152, 155, 163], an example from [163] is shown in Eq.(39).

$$CL(DoD) = ae^{b \cdot DoD} + ce^{d \cdot DoD} \quad (39)$$

Here,

- $CL(DoD)$: cycle life as function of DoD
- a, b, c, d : curve fit parameters

Others, such as [131], have modelled the DoD dependency using a power law relationship as shown in Eq.(40)

$$C_{fade} = 0.0123 \cdot cd^{0.07162} \cdot nc^{0.5} \quad (40)$$

here,

- C_{fade} : percentage capacity fade
- cd : cycle depth / depth of discharge
- nc : number of cycles

LIMITATIONS & CHALLENGES: DOD

Even though the Wöhler curve has shown a good correlation with degradation data in several studies, readers and modellers should be aware that these results are also dependent on other stress factors and therefore cannot be generalized or extrapolated to other operating conditions.

In fact, in [105, 151, 198] it is argued that one of the causes of degradation due to DoD is the traversing between different phases of the anode and cathode. As a result, the effect of DoD is heavily SoC dependent. Following this analysis, for a given DoD it could be possible that the battery stays in the same voltage plateau, resulting in negligible effects between various DoD. Or a slight change in SoC might lead to a considerable capacity decrease (or resistance increase), as shown in Figures 49 and 51. Two observations are made: 1. The most degradation is observed at higher SoC, where the anode is in its second stage according to Figure 41 and the largest change in anode volume is observed [198]. 2. Secondly, regions where phase transitions occur lead to additional degradation. In [201] it was confirmed for an NMC cell that traversing of the voltage plateaus resulted in more volume changes of the cell, whereas the volume change is low if the cycle stays within a particular plateau region. These volume changes can cause particle cracking,

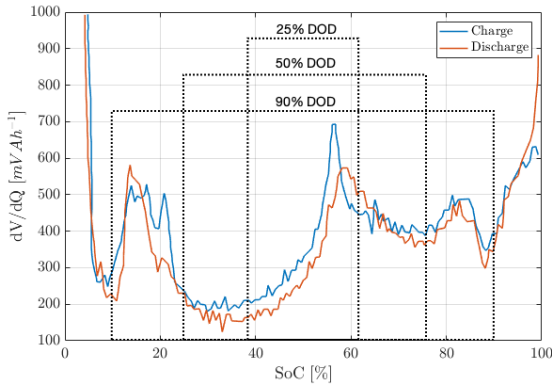


FIGURE 51: Differential voltage curve for an NMC cell under slow charge and discharge rates. The number of phase transitions depends on the DoD and the starting SoC, as indicated by the different intervals.

resulting in an accelerated growth of the SEI layer [105, 202]. Therefore, the authors of [201] conclude that the stresses per full equivalent cycle are dependent on the number of voltage plateaus traversed.

Similar conclusions for NMC cells were drawn in [151], where an increased DoD showed an increased degradation. For all cases resulting in an almost linear course of degradation for both resistance and capacity. DVA showed that cycles that cross anode voltage plateaus caused additional degradation due to mechanical stress. Over time the voltage peaks decreased. The authors conclude that the disordering of the anode lattice could be a possible explanation. Another explanation could be an in-homogeneous load over the electrode, as was shown in simulation in [64, 203]. Overall the lowest degradation was observed for cells cycled around an average SoC of 50%, probably caused by a strong superposition of other SoC-dependent mechanisms caused by cell voltage or impedance.

A similar linear course of degradation was observed in [104], where the cycle life of batteries for satellite applications was investigated by cycling NCA cells with only 1-4 cycles per day. The authors noticed that as the cycling frequency increased, a linear component on top of \sqrt{time} behaviour started to arise. This linear degradation of capacity and resistance increased as the DoD increased. Based on a destructive physical analysis, the authors argued that damage to the cathode's active material reduced lithium adsorption capability. Furthermore, Transmission Electron Microscopy showed

that, compared to calendar degradation, the amorphous⁶ layer was less thick and consisted of two layers of active material. A linear component as a result of cyclic degradation was observed in other studies as well [72, 104, 142, 163, 180]. An example of this is shown in Figure 43, where an increasing DoD results in an increasing linear degradation. Unfortunately, no further investigation on the root cause of DoD-dependent degradation was performed in [72, 104, 142, 163, 180].

Due to the complex correlations between SoC and DoD it is incredibly challenging to model their correlations. To this extend, none of the above described models can accurately model these effects outside the conditions at which these models are tested, which shows the importance of carefully selecting test conditions.

So far, all studies discussed have reported an increase in degradation for higher DOD, given that all other conditions are equal. However, in [105, 166] a higher DoD actually lead to less degradation. In [105] significantly less degradation was observed for cells cycled with 100% DoD compared to other DoDs, independent from C-rate and temperature. Using electrical impedance spectroscopy, the authors discovered that the resistance remained constant for a long time despite a fast initial increase. The cells cycled with a DoD of 50%, showed a more linear increase in resistance. As a result, it also reached the critical SEI layer resistance earlier, causing lithium plating and a reduced lifetime. Further investigation showed that the CV region played an important role in forming a stable SEI layer, indicating that its formation is strongly voltage-dependent and kinetically slow. Therefore, the cells cycled at 100% DoD might have a more stable SEI layer resulting in longer cycle life.

The effect of DOD on an LFP cell's cycle life was also tested in [166]. Their results are shown in Figure 52 and 53. The DoD-dependency on cycle life is shown in Figure 60(b), showing an increased cycle life for a $\text{DoD} \geq 50\%$ around an average SoC of 50%, at 1C 30°C. In contrast to some of the studies mentioned above, the authors did not find any clear correlation between the anode degradation phenomena and the DoD dependent degradation. Note, that these cells were tested at a starting SoC of 100%. Therefore, the reduced degradation at higher DoD's might result from a lower average cell voltage. Also, following the results of [105], it could be argued that a higher average voltage results in faster but more stable growth of the SEI layer. The total cycle life of these cells could therefore be improved on the long term. This is supported by the fact that only the cells cycled at 100%

6 without a clearly defined shape or form

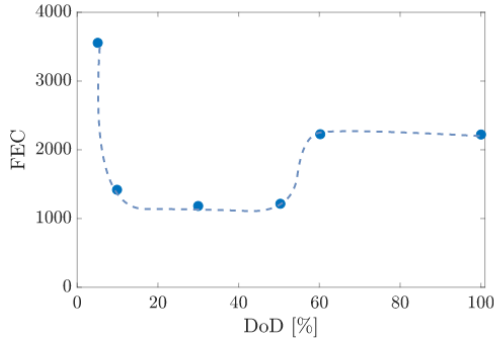


FIGURE 52: Number of full equivalent cycles for different DOD ranges obtained in [166], before reaching 90% remaining capacity. Remarkably, less degradation is observed for high DoD cycles. The cells have been cycled with 1C at 30° around 50% average SoC.

DoD showed an increase in degradation (both capacity and resistance) after 3000 FEC, possibly resulting from electrolyte depletion or lithium plating.

Figure 53 also shows that the cells with a moderate increase in resistance only experienced low structural damage due to cycling [120]. Another possible explanation for the discrepancy in the results of [166], can be that the lattice structure of LFP cells better allows for complete delithiation compared to NMC cells, resulting from higher stability. [204, 205]. Furthermore, manganese-containing chemistries, such as the cells studied in [105, 151, 201], are more prone to SoC induced degradation. Due to degradation mechanisms such as Jahn-Teller distortion, transition metal dissolution, structural damage due to complete delithiation, and electrolyte oxidation [80, 93, 111]. Of course, additional testing and analysis should be carried out to pinpoint the exact cause of degradation.

KEY INSIGHTS ON THE EFFECT OF DOD

Based on the section above, the following key insights on the effect of DoD on LIB degradation can be summarized:

- Most often, the cycle life decreases as DoD increases. However, in terms of total charge throughput, different optima are observed at various DoD's.
- DoD effect can also be perceived differently due to the coexistence of various degradation mechanisms and the interdependency with other

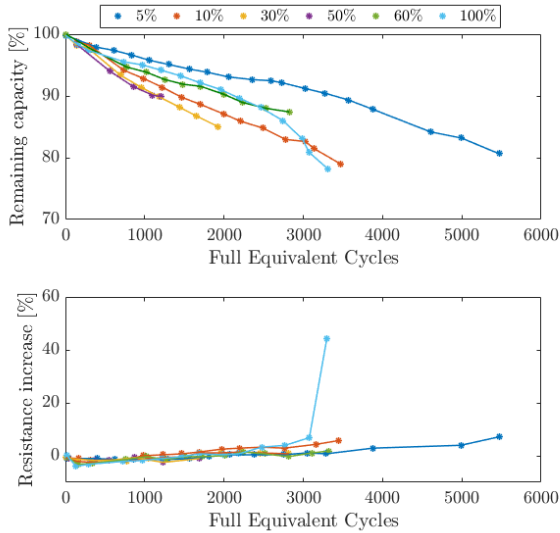


FIGURE 53: Degradation of LFP cells cycled with varying DoD, $1C$, 30° . The results show a reduced degradation for cells cycles with a DoD above 50% [166]. However, the increase in resistance for the cells cycled with 100% DoD around 3000 FEC could indicate the onset of lithium plating and therefore significantly reduce its lifetime.

stress factors, such as high and low cell voltage, different temperatures, or various current rates. As a result, assessing DoD-dependent degradation can be very difficult, especially for highly varying power profiles.

- The effect of DoD is strongly SoC dependent. More specifically, the traversing of voltage plateaus, or the transitioning between electrode phases, has increased mechanical stress due to volume changes. Often resulting in a linear component in degradation behaviour. Additionally, the CV region can play a significant role in providing a stable SEI layer and therefore affect the degradation due to DoD.

4.4 CURRENT CHALLENGES & FUTURE TRENDS

This section provides an overview of the current challenges and future trends with respect to LIB degradation, and degradation modelling.

4.4.1 *New Battery Chemistries*

For EV and RES applications, two of the most common cathode materials are Lithium-Nickel-Manganese-Cobalt-Oxide (NMC) and Lithium-Iron-Phosphate (LFP) [206], with graphite as anode material. The main objective in the development of new chemistries is to improve performance. However, also the environmental and societal footprint of the raw materials will start to play a more significant role as the LIB market increases. Therefore the use of rare and toxic elements, such as Cobalt and Nickel, should be avoided as much as possible [206–208]. In the future, some promising new anode materials could be based on LTO, Silicon (Si) or Tin (Sn), or other carbon-based structures such as graphene or carbon nanotubes [207]. The list of future cathode materials is smaller, and will probably involve new combinations of the existing materials mentioned in section II, page 7 of this paper [208]. Another possible improvement could be the use of nanostructures. Besides incremental changes to existing technology, other more disruptive chemistries include Li-Air and Li-Sulfur, which achieve very high energy densities. Modelling the degradation behaviour of these new chemistries will play an important role in quantifying their performance. Si-C based anode materials for example, provide exceptional energy density at the expense of a significantly reduced lifetime due to structural damage [92]. For more information, interested readers are directed to [92, 207, 208].

4.4.2 *Second-life Batteries*

Besides new battery chemistries, another way to reduce the cost and environmental impact of LIBs is to use second-life batteries (SLB). SLBs are repurposed EV batteries deemed unfit for EV applications but still have sufficient capacity for other stationary applications such as grid reinforcement. Reusing these batteries lowers the cost of LIBs while also lowering the environmental impact by reducing the demand for raw materials. In [209, 210], the authors showed that first-life battery performance is a critical parameter to assess the remaining value and state-of-health for second-life applications. As a result, modelling and optimizing battery degradation in both first- and second-life can reduce the environmental impact of LIBs. However, most of the studies currently only investigate degradation behaviour in the first part of LIB life. For example, studies that model the degradation behaviour as a function of $\sqrt{\text{time}}$ or \sqrt{Ah} , tend to miss out on

degradation effects in the later part of their life, such as lithium plating, and are therefore less or not suitable for second-life applications.

4.4.3 *Fast Charging*

Range anxiety and long charging times are two of the main challenges for electric vehicles at this moment [211]. Fast charging is an effective tool for relieving EV users' range anxiety. Currently, most EVs can withstand maximum charging powers in the range of 50-150kW. However, new top-end vehicles, such as the Porsche Taycan or Audi e-tron GT, can charge with powers up to 350kW [212]. These maximum charging rates and total charging time are currently limited by the battery's rate capability and the thermal management of the EV. Naturally, charging at these high rates is far more damaging to the battery and to mitigate this, more and more EVs have thermally managed battery packs. Therefore, correlating the effects of temperature, C-rate, and DoD is important to accurately calculate the deteriorating effect of fast charging.

4.4.4 *Thermally Managed Systems*

Thermal management is becoming more common as a way to improve the lifetime of LIB systems. Thermal management for fast charging is an example of this. However, thermal management is also used at lower charging rates to prevent lithium plating at low temperatures. Other applications include stationary applications, such as RES integration or ancillary services. These systems generally have climate control systems, that control the temperature to be around 20-25°C to have optimal cycling performance. To this extend, extensive testing of degradation behaviour around room temperature could be argued to be vital for good modelling accuracy.

4.4.5 *Artificial Intelligence for degradation Estimation*

As mentioned in the introduction, the different degradation estimation techniques such as PBMs, ECMs, or EMs all provide different trade-offs between modelling accuracy, complexity, and computational demand. Recently, various AI techniques have been investigated as ways to achieve high accuracy with low computational demand. These techniques can be differentiated into two groups. The first group train their AIs on model-fitted features, such as internal resistance and SoC, to estimate the SoH.

These models then require other models to extract these internal parameters. The second group uses external features, such as open-circuit voltage and incremental capacity curves, to estimate SoH [79]. The latter do not rely on other models to calculate the internal parameters and therefore have a lower computational complexity, and as a result are better suited for real-time applications.

4.5 SELECTION OF DEGRADATION MODEL

Based on the presented review of battery degradation models, the model presented in [143] has been selected as the best fitting model for the smart charging algorithm, because of the following reasons:

- The model has been designed for the NMC-LMO chemistry, a chemistry which is considered a viable candidate for both EV and stationary applications [213]. Similarly, the same model can thus be used for both the EV and BES.
- The test conditions described in [143] match with real-life conditions for both EV and BES applications. More specifically, most cells were cycled between 10°C and 34°C . Whereas, a lot of studies focus on accelerated testing conditions with temperatures above 35°C . Additionally, at every temperature a variety of different C-rates and DoDs were used. Again not only focussing on accelerated testing conditions, but also including low C-rates (0.5C-6.5C) and DoD (10%-90%). An additional advantage is that cells were tested with maximum 90% DoD. As seen in the review presented above, cycling up to 100% SoC can be far more detrimental, and as a result this operating point is often avoided. This DoD-dependence was not originally included in the model presented in [143]. However, based on their presented data, this dependency will be added in the next chapter.
- It is one of the few models which has modelled the temperature dependence of C-rate. As shown in Fig. 46, a strong correlation exists between C-rate and temperature. More specifically, the effect of C-rate is much more pronounced at lower temperatures. Unfortunately, as seen in Table 11, many models have not tested their cells at temperature below room temperature. Furthermore, even less studies have included this interdependency in their model.
- The model is part of the few models which separate calendar degradation and cyclic degradation, by subtracting the calendar degradation

results from their cyclic degradation results. The result is a more accurate model which can be used for both cyclic and calendar degradation studies. This is especially useful for smart charging studies, as it is expected that the charger will not be continuously charging.

The model is shown in Eq.27-28, and repeated here for clarity:

$$Q_{loss} = B_1(T)e^{B_2(T)I_{rate}} Ah \quad (41)$$

with,

$$B_1(T) = aT^2 + bT + c, \quad \& \quad B_2(T) = dT + e \quad (42)$$

where:

- Q_{loss} : Lost capacity.
- T : Temperature.
- I_{rate} : C-rate.
- Ah : Throughput.
- a, b, c, d, e : curve fit parameters.

4.6 CHAPTER CONCLUSIONS

In this chapter, a review on the behaviour and empirical modelling of LIB degradation was presented, focussing on the effect and interdependency of operational stress factors. The presented review concludes that it is very difficult to generalize degradation behaviour, with respect to the effect of operational conditions. Usually, the resulting degradation is caused by a combination of stress factors rather than attributable to a single stress factor. To this extent, users of empirical and semi-empirical battery degradation models should be cautious of their models' limitations and the correlations between the stress factors. To summarize some of the key findings:

- SEI growth is considered to be the most important degradation mechanism for both cycling and calendar degradation. A strong correlation with anode potential is observed during idle conditions: a higher SoC results in increased SEI layer growth. However, other kinetic effects during cycling can accelerate degradation at low SoC. SoC-dependent calendar degradation is often modelled to exponentially dependent, whereas its effect on cyclic degradation can have different forms depending on the operating conditions.

- Because of the passivation character of the SEI layer, the degradation behaviour is most commonly modelled using a t^z or Ah^z relationship, with $0.5 \leq z \leq 1$. Unfortunately, many cyclic degradation models do not differentiate between cyclic and calendar degradation, and therefore measure their combined effect. Others have subtracted calendar degradation from their cyclic degradation results to model the effect of cyclic degradation only, resulting in higher modelling accuracy.
- The Arrhenius law is an effective model for the temperature dependence of calendar degradation. However, during cycling, different degradation mechanisms are observed above and below room temperature. These should be considered when modelling cyclic degradation below room temperature. Since most studies are based on accelerated test conditions, this is frequently overlooked. Possible solutions include combining positive and negative activation energy in Arrhenius laws or including parabolic temperature dependencies.
- The effect of C-rate is often modelled to be exponentially dependent. Several studies, however, have found insignificant differences at C-rates less than 2. Furthermore, multiple studies have found a strong correlation between C-rate and temperature; as temperature rises, the impact of C-rate decreases significantly. Many models do not take this into account, which is in part due to accelerated testing conditions.
- Several studies modelled the DoD dependent degradation based on Wohler curves or other exponential curves. However, the effect of DoD is directly related to other SoC associated mechanisms and is therefore probably the most difficult stress factor to model. Additionally, the impact of DoD is affected by volume change due to electrode phase transitions and is thus also related to C-rate and temperature.
- The model presented in [143] was chosen for application in the smart charging model.

This chapter introduces the hierarchical smart charging control. The top level consists of a 24 hour ahead optimal scheduling algorithm, in the form of a non-linear programming (NLP) model, the second layer consists of a real-time controller used to deal with forecasting errors. Both the system sizing and smart charging are done by the same NLP model. This allows the system sizing to be determined based on its power management. The NLP model minimizes the total system cost and incorporates multiple business cases, such as energy trading, primary frequency control, and second-life battery value. The second-life value of the battery system is determined using the battery degradation model discussed in the previous chapter.

This chapter is based on:

- J3 W. Vermeer, M. Wolleswinkel, J. Schijfelen, G.R. Chandra Mouli, P. Bauer, *Design of a 10kW Multi-Port EV Smart Charging System Integrating EV, PV, and Battery, 2023, (under review for) IEEE Transactions on Transportation Electrification*
- J2 W. Vermeer, G.R. Chandra Mouli, P. Bauer, *Optimal Sizing & Control of a PV-EV-BES Charging System Including Primary Frequency Control and Component Degradation, 2022, IEEE Open Journal of Industrial Electronics*
- J1 W. Vermeer, G.R. Chandra Mouli, P. Bauer, *Real-time Building Smart Charging System Based on PV forecast and Li-ion Battery Degradation, 2019, Energies*

5.1 INTRODUCTION

The bidirectional EV-PV-BES charging system, discussed in chapters 2 and 3, is capable of a high variety of different power flows thanks to the bidirectional nature of the multi-port converter. However, the converter itself relies on external setpoints to determine when to charge and with what power. Current day EV-PV charging systems generally use one of the following two charging schemes:

1. Constant-current constant-voltage (CC-CV) charging: when plugged-in the EV is charged with the constant maximum current, until the maximum voltage limit of the battery is reached. Afterwards, the charging current is reduced to maintain a constant battery voltage.
2. PV charging: instead of charging with a constant current, the EV is charged with the available PV power, until the maximum voltage of the battery is reached.

Two simplified versions of these charging methods are shown in Fig. 54a and 54b. Here it is assumed that the EV is available between 08:00h-18:00h at an office building with load P_{load} and PV power P_{pv} . The BES is charged or discharged based on the net power in the system P_{net} calculated according to Eq. (43).

$$P_{BES} = P_{net} = P_{PV} - P_{EV} - P_{load} \tag{43}$$

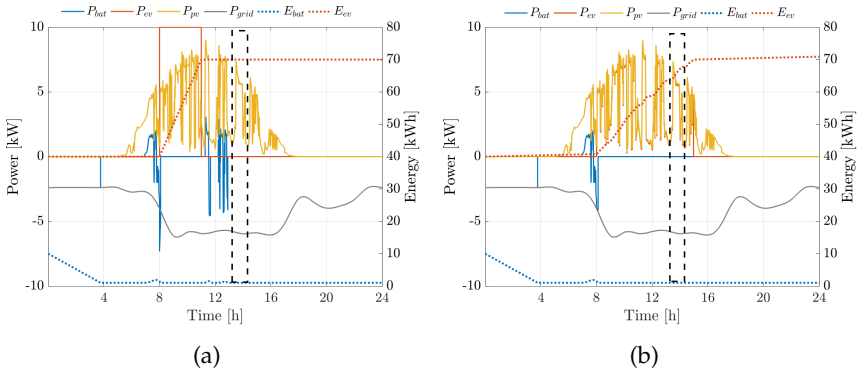


FIGURE 54: Two example days for (a): Fixed rate charging (assuming a constant battery voltage), and (b): PV charging. Assuming the 10kW EV-PV-BES integrated converter is installed at a building with load P_{load} .

Based on Fig. 54a and 54b, the following shortcomings of these charging schemes can be identified:

- For both direct PV charging and fixed rate charging it can be concluded that the BES is hardly used. Only during the night and early morning, the residual capacity in the BES is used to power the load. However, in both cases, the BES is barely charged after it is depleted, simply because there is no excess power. This points to the conclusions made in earlier studies [7], which state that stationary BES are not cost-effective for EV-PV charging applications when simple heuristic control schemes are used.
- Similarly, both charging schemes have no way of utilizing the energy capacity available in the EV. Using EVs as a movable energy storage is expected to play a major role in the energy transition, as they can be used to store renewable energy and provide energy to different loads when needed. This is called Vehicle-to-grid (V2G), or Vehicle-to-X. However, to utilize the benefits of V2g additional control is required.
- The PV charging scheme achieves a very high PV self-consumption rate. However, it has no knowledge of future PV power production. As a result, it has a high risk of not meeting the energy demand. On the other hand, fixed rate charging has a low risk of not meeting the energy demand, but charges partially from grid energy and causes a high amount of PV power to be fed in to the grid.

To summarize, existing charging schemes lack 'intelligence'. They are not able to fully utilize the synergies of combining EV, PV and BES. In recent years, smart charging has been investigated as a way to overcome these shortcomings. Smart charging is often implemented using optimal scheduling programs, which optimize the power flows inside the charging system.

This chapter presents a two-level smart charging system (SMS) that minimizes the total cost of energy by finding the optimal charging and discharging rate of the EV and BES, based on a forecast of energy prices, PV power, LIB degradation, and participating in the frequency containment reserve market. Additionally it also determines the optimal component ratings. A schematic representation of the proposed system is shown in Fig. 55.

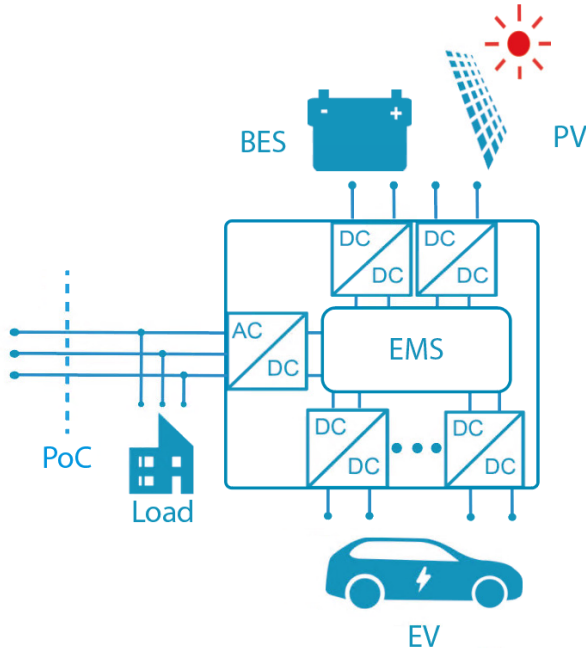


FIGURE 55: Schematic of the proposed smart charging system (SMS).

5.1.1 Chapter Organisation

The remainder of the chapter is organized as follows: Section 4.2 describes the proposed control structure. The two parts of this structure are explained in more detail in sections 4.3 (Non-linear Programming (NLP) model), and section 4.4 Real-time control. Next, the use cases will be specified in Section 4.5. After which the obtained results are discussed in Sections 4.6 and 4.7, followed by the Conclusion in Section 4.8.

5.1.2 Related Work

The related literature is divided into two different categories 1. Studies regarding the optimal power management of integrated SMSs and 2. Studies regarding the optimal sizing of integrated SMSs. An overview of all related studies and their features is shown in Table 12. The studies are compared based on whether or not they include the following features: optimal control, optimal component sizing, optimal energy arbitrage (λ_E), optimal integration of FCR markets (λ_{FCR}), optimal EV smart charging (EV s.c.), PV

Reference	Opt. control	Opt. sizing	Opt. λ_E	Opt. λ_{FCR}	EV s.c.	PV self.	BES/EV aging	SLB value	PV aging
[214–218]	✓		✓		✓				
[219]	✓		✓		✓	✓			
[220, 221]	✓		✓						
[218, 222–224]	✓					✓			
[225, 226]	✓		✓		✓		✓		
[227, 228]	✓		✓		✓	✓	✓		
[229]	✓		✓				✓		
[230]	✓		✓	✓			✓		
[231]	✓				✓	✓		✓	
[232]	✓				✓	✓	✓	✓	
[233, 234]	✓		✓	✓	✓	✓			
[235, 236]	✓		✓	✓	✓				
[234]	✓		✓	✓		✓			
[237]	✓			✓	✓		✓		
[238, 239]	✓		✓	✓					
[240]	✓		✓	✓		✓			
[241, 242]	✓		✓	✓			✓		
[243, 244]	✓		✓	✓	✓				
[245]	✓			✓			✓		
[246]		✓		✓					
[247, 248]		✓				✓			
[249–251]		✓					✓	✓	
[252–254]	✓	✓				✓			
[255]		✓				✓		✓	
[256]		✓			✓			✓	
Proposed	✓	✓	✓	✓	✓	✓	✓	✓	✓

TABLE 12: Summary of related studies

self-consumption, BES or EV degradation, second-life battery (SLB) value, and PV system degradation.

5.1.2.1 *Optimal power management*

SMSs or demand response systems are widely investigated in the literature [214, 215, 218–224, 257]. Among some of the common objectives is to optimize costs [215, 220, 221, 257], achieve net-zero energy [219, 222–224], or peak shaving [222]. Often using smart control of storages such as BES systems or EVs in combination with renewable energy resources to achieve these objectives [215–217, 219–222]. However, as seen from Table 12, many of these studies do not take into account the effects due to battery degradation, which can lead to nonoptimal results and false impressions on usable capacity, and total costs. Several studies have overcome this by including battery degradation model. For example, to minimize operational cost of a battery swapping EV charging station [225], optimize vehicle-to-grid (V2G)

charging aggregation [226], or minimizing the operational cost of an EV charging station integrated with PV and BES [227]. A different approach is used in [229] where a deep reinforced learning model is used to optimize battery energy arbitrage. Similar studies have been conducted in [228, 230].

Another effective way to reduce the total cost of energy are SLB [231, 232], which are repurposed batteries deemed unfit for their first application (generally EVs), but still have enough capacity left for other applications. In [232] a degradation model is used to assess the remaining lifetime of second-life batteries in EV charging stations. Their results show that using SLBs can reduce the total investments costs, and that degradation models are useful in prolonging battery life and maximizing their utilization.

Aside from optimized smart charging based on RES, prosumer participation in regulatory markets has recently been investigated as a way to increase revenue and overcome stability issues associated with a decentralized energy system. This is currently mainly done by utility scale BES systems or large factories. However, with the increasing amount of EVs also EV charging systems have shown to be very valuable assets for the FCR market [233, 243, 244]. Furthermore, a few studies have investigated combining the FCR market with other revenue streams. In [233] it is shown that the integration of EV smart charging, including V2G and the FCR market can save up to 317 percent on annual costs, compared to uncontrolled EV charging. Additionally, the authors of [240] show that FCR market integration can improve revenue streams by up to three times, compared to PV self-consumption alone. Similar results, on the integration and co-optimization of the FCR market and other business cases such as energy markets are obtained in [234–236, 239, 241].

5.1.2.2 *Optimal Sizing*

Because PV and BES systems are typically the most expensive components of integrated SMSs, optimizing their dimensions is critical for having a cost-effective system. [258]. In [249] the authors investigated the techno-economic feasibility of DC nano-grid by sizing the PV, EV and BES systems using a multi-objective particle swarm optimization. A similar approach was used in [247, 248]. Some studies used battery degradation models to determine BES lifetime and further optimize the BES system [249–251], and others have investigated the optimal size of SLBs to mitigate the intermittency of PV power in a PV-BES system [255], or for SLB assisted EV charging stations [256]. All of the above-mentioned studies use rule-based power-control schemes to determine the optimal DER dimensions. However, many

studies have shown that their revenue is significantly lower than optimal power control schemes, and as a result, will lead to suboptimal results when used for sizing of optimal SMSs. Unfortunately, due to daily and seasonal variations, sizing studies require large data sets, making them unsuitable for some deterministic optimization models. This could be a potential reason why only [252–254] have investigated the combined optimization of power management and component sizes using, as shown in Table 12. Furthermore, Table 12 also shows that although multiple studies have been conducted to investigate the optimal control based on energy markets, FCR markets, and DER-powered EV smart charging, no study has yet addressed the optimal sizing for any of these business cases based on optimal power management.

5.1.3 *Contribution*

From the literature review above, it is concluded that several studies have shown the effectiveness of EV-PV smart charging, optimal FCR market participation, or DER integration using EVs and BESs. Some studies have even looked into combining some business cases, as summarized in Table 12, and found that this can result in significantly higher gains. Next, battery degradation models have been found to be effective in prolonging lifetime and reducing the cost of ownership in both optimal control and sizing, while other studies have shown that even after batteries have degraded significantly, they still have value in second-life (SL) applications and can thus be used to reduce costs in both first- and second-life applications. Even though all these aspects have proven to reduce the total costs and help with DER integration, no study yet has integrated all of these into one optimal power management method. Furthermore, no study has yet addressed the sizing for a PV-EV-BES integrated SMS, for business cases based on optimal power management such as, smart charging, FCR market participation, PV self-consumption, or any combination of these.

Therefore, the main contributions of this chapter can be summarized as follows:

1. A comprehensive model for the simultaneous optimization of components ratings and their power management is proposed. Improving upon current literature, the proposed method integrates multiple business cases for smart charging such as local PV self-consumption, PV powered smart charging (including vehicle-to-grid), optimal sizing

- based on optimal power management, the FCR market, and second-life battery value.
2. By incorporating accurate energy storage models for both EVs and BES, and including the effects of degradation and the effect of SoC on power availability, current research regarding optimal sizing and control is extended. Due to the comprehensive model the degradation model serves multiple purposes: 1. Firstly, the degradation is minimized, and the effect of BES size on degradation is taken into account, 2. Secondly, the actual remaining capacity is known throughout the simulation time, resulting in a more accurate trade-off between energy arbitrage and balancing reserves, 3. The BES lifetime is estimated based on its operating conditions, 4. The second-life value of the BES is assessed based on its remaining capacity, resulting in a more accurate estimation of operational and investment costs.
 3. For the first time, a lifetime cost and performance analysis is performed, including the effect of component degradation on FCR market participation and total lifetime revenue. The results show that EV, BES, and PV degradation and BES second-life value are significant parts of the total costs in their lifetime. To this extent, this is the first optimal sizing/control study of a new PV-EV-BES system to address the importance of second-life BES value and optimize its value during the design of the energy management system.

5.2 CONTROL STRUCTURE

The bidirectional power capabilities of the four-port system allow for a high number of possible power flows. It, therefore, requires an adequate control structure to utilize its flexibility optimally. The DC/AC converter maintains the power balance on the DC link, which allows the design to be modular. Furthermore, the PV-port performs maximum power point tracking (MPPT) to maximize renewable energy production. The setpoints of the two remaining ports, the EV and BES, can then be calculated independently from each other as long as the power balance constraint on the DC link is satisfied.

The three-level control structure, as shown in Fig. 56, is proposed. At the highest level is the 24-hour ahead optimal scheduling algorithm operating. This non-linear programming (NLP) optimization problem is solved in a moving horizon window and is solved using ANTIGONE. The second level is the real-time error handler control, abbreviated as RTC. The main goal of the RTC is to re-calculate the setpoints within each 15-minute optimization

step by comparing the forecasted values with the actual, or measured, values. Finally, the lowest level are the control loops embedded on the power electronic hardware. These ensure closed-loop control, as well as protection, and were discussed in Chapter 2. Both the optimal scheduling and RTC are implemented on a PC, the final setpoints calculated by the RTC are send to the converters over a CAN-bus using a CAN-to-USB converter, as shown in Fig. 55. In the coming sections each control level will be discussed in more detail, starting with the optimal scheduling.

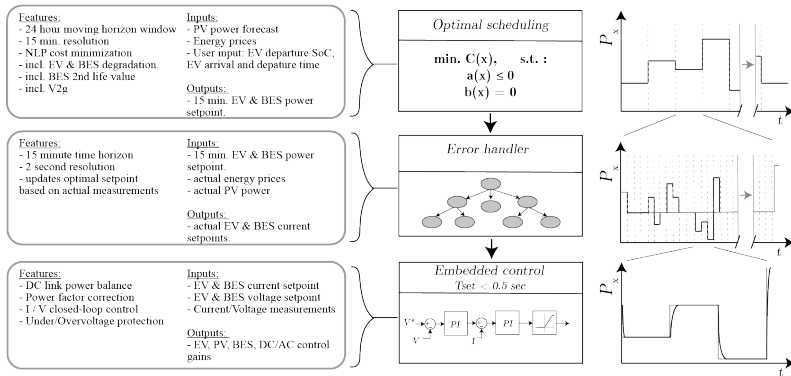


FIGURE 56: The three layers of the control hierarchy. The top level is an optimal scheduling algorithm, followed by a real-time error handler which sends the setpoints to the embedded V-I controllers.

5.3 OPTIMAL SCHEDULING

This section discusses the highest level of control structure; the optimal scheduling. This is done with a 24, or 48 hour ahead moving horizon window, with a 15 minute resolution. The same NLP model is also used for optimal system sizing. In that case, a one hour resolution is used in order to total problem size.

In the coming section C_X stands for the cost of X , V_X is the value per kW or kWh of X , P_X is the power of X , E_X is the energy of X , and λ_X is the price of X . Furthermore, superscripts *rated* declare the optimally determined rated value of X , superscript *min/max* declares the time (e.g. SoC) dependent minimum or maximum of X . $+/-$ Declares a positive or negative direction, Δt stands for the timestep and i indicates a particular EV instance.

5.3.1 Objective Function

The model's objective is to minimize the overall cost of energy to increase the attractiveness of integrated energy systems. The overall costs include the total PV and power converter costs $C_{PV+conv}$, BES degradation costs C_{BES} , grid electricity costs C_{grid} , interest costs C_{int} , and income from the primary frequency containment reserve (FCR) C_{FCR} market. A distinction for C_{BES} is made, as its performance cannot be presumed to be constant over their lifetime. The total objective function then results in:

$$\min(C_{total}) = \min(C_{PV+conv} + C_{BES} + C_{EV} + C_{grid} + C_{int} - C_{FCR}) \quad (44)$$

5.3.1.1 PV - Power Converter Costs

The optimization determines each multi-port converter component's rated power, denoted as P_X^{rated} , where X indicates the converter. In this study the converter performance is assumed to be constant over a 15 year lifetime T_{life} [259]. Therefore, the total PV and converter investment costs are denoted using (45). Here $\frac{1}{T_{sim}T_{life}}$ is used to annualize the cost, based on a half-year simulation period. Here T_{sim} is the number of simulation periods in a year (equal to two). The PV costs per kWp V_{PV} comprise the panel cost and converter costs. Additionally, it is assumed that all values also include all possible related costs such installation costs, maintenance, development, etc, as energy outlook reports [260, 261] often combine these. The total converter investment costs are then equal to:

$$C_{PV+conv} = \frac{1}{T_{sim}T_{life}} \left(\sum_{i=1}^n V_{EV}^{Ch}(i)P_{EV}^{rated} + V_{BES}^{Ch}P_{BES}^{rated} + V_{inv}P_{inv}^{rated} + V_{PV}P_{PV}^{rated} \right) \quad (45)$$

5.3.1.2 Energy Storage Degradation Costs

The costs of battery degradation are calculated to account for the loss of capacity and loss of value, for both the BES and every i th EV. The same method is applied to all, hence the subscript $X = EV, BES$ is used for conciseness. The degradation cost C_X consider:

- The cost due to the reduction of energy capacity in kWh, calculated based on a cycle- and calendar life degradation model described in Section II.B.3.

- The cost due to the reduction of value per kWh, calculated according to the model presented in [260]. Here the remaining value per kWh is calculated based on the remaining capacity of the battery.

Based on the model presented in [260] it is assumed that the remaining value per kWh value decreases linearly with remaining capacity, the battery is in its first life, ending at 70% remaining capacity: $E_X^{2nd} = 0.7$, at 50% remaining value per kWh: $V_X^{2nd} = 50\%V_X^{new}$ [210, 260] as shown in Fig. 57. The total degradation costs are then calculated according to (46)-(47).

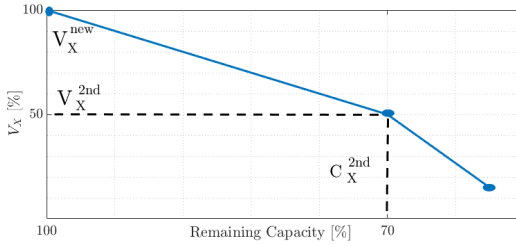


FIGURE 57: Decay of value per kWh according to the model presented in [260]

ΔE_{BES}^{tot} and E_{BES}^{max} indicate the total degraded capacity and maximum initial capacity, respectively, and will be calculated in section II.B.3.

$$V_X(i, t) = \frac{(V_X^{2nd} - V_X^{new})}{1 - E_X^{2nd}(i, t)} \Delta E_X^{tot}(i, t) + V_X^{new} \quad (46)$$

$$C_X = \sum_{i=1}^n \left((V_X^{new} - V_X(i, t)) (E_X^{rated}(i, t) - \Delta E_X^{tot}(i, t)) \right) \quad (47)$$

5.3.1.3 Grid Energy Costs

Besides cost due to degradation, another part of the operational expenditure are the grid electricity costs. A distinction between $P_{grid}^+(t)$ and $P_{grid}^-(t)$ is made in order to account for the difference in price. The resulting cost are given in (48).

$$C_{grid} = \sum_t^T P_{grid}^+(t) \Delta t \lambda_{buy} - \sum_t^T P_{grid}^-(t) \Delta t \lambda_{sell} \quad \forall t \quad (48)$$

5.3.1.4 Interest Cost

The cost of interest is equal to the potential income received if no expenditure had been made. Here the EVs are not taken into account, as they are assumed to be bought independently from the proposed SMS. An annual interest $p\%$ of 1% is taken into account, the resulting interest cost is then calculated according to (49)-(50). If the simulation period covers multiple years, Eq((50)) can be multiplied with an amortization rate A as shown in (51)

$$C_{invest} = V_{BES}^{new} E_{BES}^{rated} + C_{PV+conv} \quad (49)$$

$$C_{int}(t) = C_{invest} p\% \frac{1}{T_{sim}} \quad \forall t \quad (50)$$

$$A = \frac{p\%(p\% + 1)^n}{(p\% + 1)^n - 1} \quad (51)$$

5.3.1.5 Frequency Containment Reserve

The last part of the objective function is the revenue obtained from the primary frequency containment reserve (FCR) market. Based on a pilot study regarding prosumer FCR market participation in the Netherlands [262], it is assumed that a third party acts as an aggregator, combining several systems to reach the minimum bidding power requirement for FCR market participation. Revenue is then generated by reserving a part of the available power capacity for up/down-regulation [263], here denoted as P_{reg}^{up} and P_{reg}^{down} , respectively. The up/down-regulation prices are: $\lambda_{up}, \lambda_{dn}$ (obtained from [264]), respectively, and ϵ_{agg} is a margin between 0 and 1, used to denote the cost of aggregation. Based on regulation prices, the operational costs, and the current demand, the optimization will determine how much of the available power capacity to reserve for regulation. Calculated in the constraints below. The total obtained revenue is then equal to:

$$C_{FCR} = (1 - \epsilon_{agg}) \eta_{inv} \eta_{ch} \sum_{t=1}^T \left(P_{up}(t) \lambda_{up}(t) + P_{dn}(t) \lambda_{dn}(t) \right) \forall t \quad (52)$$

Note that only the revenue obtained from acting as reserve is taken into account as the net energy delivered is assumed zero. This concludes the objective part of the model. The next section discusses the model constraints.

5.3.2 Constraints

5.3.2.1 Power Balance & Limitations

Fig. 55 shows a schematic representation of the proposed system. In this study, positive BES/EV power denotes charging operation, and positive grid power is equal to feeding power to the grid. For the given system, two power balances exist: 1. The first power balance is on the DC link of the multi-port converter:

$$P_{inv}(t) = P_{PV}(t) - P_{BES}(t) - P_{EV}(t) \quad \forall t \quad (53)$$

(54)-(55) model the maximum power point tracking of the PV converter. The model becomes more flexible by allowing PV power curtailment during negative electricity prices or oversized PV systems. Here the symbol η_{mppt} is used to model converter efficiency, which equals 98% [63]. $\Delta_{PV}(t)$ represents the degradation of the PV panels, which is included as a linear decay of 1% a year [265].

$$P_{PV}(t) \leq \eta_{mppt}(1 - \Delta_{PV}(t))P_{PV}^{irradiance}(t)P_{PV}^{rated} \quad \forall t \quad (54)$$

$$P_{PV}(t) \geq 0 \quad \forall t \quad (55)$$

Next, for all bidirectional converters, a distinction is made between positive and negative powers to account for the converter's efficiency. This is described using (56)-(58). Here η_{BES}, η_{EV} , and η_{inv} are equal to 97.5% (initially), 97.5%, and 97% for the BES charger, EV charger, and inverter, respectively. For the EV and BES it also includes the battery losses of a single charging or discharging instance [266]. Furthermore, the BES and EV's internal resistance increases due to degradation. This is accounted for by making it dependent on $E_X^{lim}(t)$, according to 58). It is assumed that the internal resistance is doubled, when the battery reaches 70% of its nominal capacity [144, 150].

$$P_X(i, t) = \eta_X P_X^+(i, t) - \frac{1}{\eta_X} P_X^-(i, t) \quad \forall t \quad (56)$$

$$P_{inv}(i, t) = \eta_{inv} P_{inv}^+(i, t) - \frac{1}{\eta_{inv}} P_{inv}^-(i, t) \quad \forall t \quad (57)$$

where,

$$\eta_X(i, t) = \eta_{ch} - 0.025 \frac{E_X^{rated}(i) - E_X^{lim}(i, t)}{0.3 * E_X^{rated}(i)} \quad \forall t \quad (58)$$

with X equal to EV or BES .

Besides being limited by the converter's rated power, the EV and BES are also limited by the maximum amount of power that can be drawn from their batteries. This is dependent on the size of the battery combined with its maximum C-rate. For stationary applications, this is often limited to $1C$ (or lower) [266]. Apart from ultra-fast charging applications, EV charging is usually below $1C$ as well. Therefore, a maximum C-rate of 2 is considered and modeled using (59). Additionally, the maximum charging powers P_X^{max} and maximum discharging power P_X^{min} are dependent on the State-of-charge (SoC) of the battery. This dependency divides the (dis)charging regions into the regions known as precharge region (very low SoC), constant-current (CC) region, and constant-voltage (CV) region. Because the maximum C-rate is $2C$, the maximum power in the CC-region is restricted by the converter's operational power limit P_X^{OP} rather than the battery's, and is thus a constant power. These are often neglected in battery sizing and smart charging studies, but impacts the available power. The charging regions are modelled using (60)-(65). Here $D_{ch/dis}$ denote the upper and lower SoC limit of the CC-region.

$$P_X^{rated} \leq 2E_X^{rated} \quad (59)$$

$$P_X^+(i,t) \leq P_X^{max}(i,t) \quad \forall t \quad (60)$$

$$P_X^{max}(i,t) \leq P_X^{op}(i) \quad \forall t \quad (61)$$

$$P_X^{max}(i,t) \leq \frac{P_X^{op}}{(1 - D_{ch})} \left(\frac{E_X(i,t)}{E_X^{rated}} - 1 \right) \quad \forall t \quad (62)$$

$$P_X^-(i,t) \leq P_X^{min}(i,t) \quad \forall t \quad (63)$$

$$P_X^{min}(i,t) \leq P_X^{op}(i) \quad \forall t \quad (64)$$

$$P_X^{min}(i,t) \leq \frac{P_X^{op}(i)}{D_{dis}} \frac{E_X(t)}{E_X^{rated}} \quad \forall t \quad (65)$$

Here P_X^{op} is used to divide the rated power of P_X^{rated} into an operational part P_X^{op} , and a reserve capacity (FCR) part P_X^{FCR} . P_X^{op} is then the power available for the operational scheduling of X , where is P_X^{FCR} is reserved for FCR capacity. This ensures that there is always enough power available for FCR provision and SoC-management. During FCR provision, both regions are available depending on the frequency deviation. The distinction is made according to (66).

$$P_X^{rated}(i) = P_X^{op}(i) + P_X^{FCR}(i) \quad (66)$$

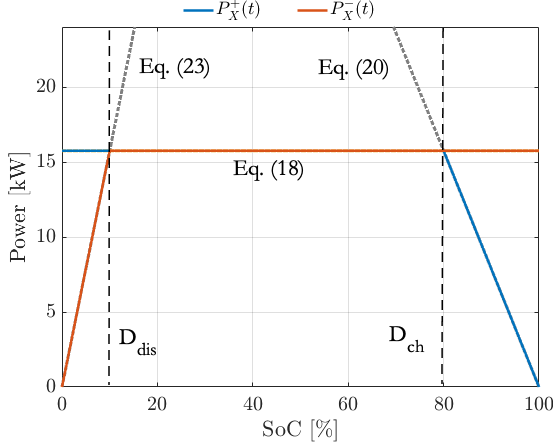


FIGURE 58: Graphical representation of $P_X^+(t)$ and $P_X^-(t)$, where $D_{dis} = 0.1$, $D_{ch} = 0.8$, and $P_X^{rated} = 15.75$

The second power balance in the system is on the AC side between the inverter and the meter. Here the appliance load $P_{load}(t)$ and heating load P_{heat} are connected, as modelled using (67).

$$P_{grid}(t) = P_{inv}(t) - P_{appl.}(t) - P_{heat}(t) \quad \forall t \quad (67)$$

In this case, both the appliance load and heating load are considered inflexible and therefore do not require any additional constraints. Using (68)-(70) the grid power is constrained by $P_{grid}^{+/-,max}$, which can be allocated dynamically allowing for power curtailment.

$$P_{grid}^-(t) \leq P_{grid}^{-,max}(t) \quad \forall t \quad (68)$$

$$P_{grid}^+(t) \leq P_{grid}^{+,max}(t) \quad \forall t \quad (69)$$

$$P_{grid}(t) = \eta_{cable} P_{grid}^+(t) - \frac{1}{\eta_{cable}} P_{grid}^-(t) \quad \forall t \quad (70)$$

Due to the difference between retail electricity price and feed-in tariff (FIT), it is important to distinguish between positive and negative grid power. Often this is done using binary variables [233, 267]. However, the use of binary variables, especially in combination with nonlinear constraints, drastically increases the solving time of any deterministic optimization problem. In order to solve this problem the efficiency η_{cable} is introduced as

a soft constraint to let the optimization recognizes the efficiency loss and prevents simultaneous nonzero values for $P_{grid}^+(t)$ and $P_{grid}^-(t)$. This is valid on the condition that the FIT is always below the retail price. However, in any practical scenario, this will be true.

5.3.2.2 Energy balance & limitations

The degradation model used in this study is developed for a single Li-ion cell. Therefore it is assumed that $N_{cell}^{parallel}$ by N_{cell}^{series} of these cells make up the total battery pack of the BES. The energy capacity of the battery pack is then determined by the variable $N_{cell}^{parallel}$, and $N_{cell}^{series} = 100$ cells are used to produce the required battery voltage, as modeled by (71). The equation is divided by a thousand in order to obtain a kWh unit. Here V_{cell}^{nom} and Q_{cell}^{nom} are the nominal open-circuit voltage and charge of a single 18650 NMC cell, in this case 3.7V and 1.5Ah, respectively.

$$E_{BES}^{rated} = \frac{N_{cell}^{series} N_{cell}^{parallel}}{1000} V_{cell}^{nom} Q_{cell,nom} \quad (71)$$

(71) describes the initial maximum energy capacity. However, over time this maximum capacity will decrease by $\Delta E_{BES}(t)$, which is determined by the battery degradation model discussed in Section II.B.3. Updating the maximum available capacity is modelled using (72)-(73).

$$E_{BES}^{lim}(t) = \begin{cases} E_{BES}^{rated}, & \text{for } t = 1 \\ E_{BES}^{lim}(t-1) - \Delta E_{BES}(t), & \text{for } t > 1 \end{cases} \quad (72)$$

$$E_{BES}(t) \leq E_{BES}^{lim}(t) \quad \forall t \quad (73)$$

Next, to calculate the degradation and power limitations, the SoC needs to be calculated based on the newly found maximum capacity, for the EVs $E_X^{lim} = E_{EV}^{max}$. This is done using (74). It is assumed that the all SoC_X are allowed to range from 10-100%, see (75). Furthermore, (76) is used to equate the beginning and endpoint SoC to have a fair comparison of energy costs. Again the subscript X is used to denote the BES, or any i th EV.

$$SoC_X(i,t) = \frac{E_X(i,t)}{E_X^{lim}(i,t)} \quad \forall t \quad (74)$$

$$0.1 \leq SoC_X(i,t) \leq 1 \quad \forall t \quad (75)$$

$$E_X(i, t) = \begin{cases} E_X^{init}(i), & \text{for } t = 1 \\ E_X^{end}(i), & \text{for } t = T \end{cases} \quad (76)$$

Finally, the amount of energy inside the BES and EV at each timestep is calculated according to (77) and (78), respectively.

$$E_{BES}(t) = E_{BES}(t - 1) + P_{BES}(t)\Delta t \quad \text{for } t > 1 \quad (77)$$

$$E_{EV}(i, t) = E_{EV}(i, t - 1) + (\gamma(i, t)P_{EV}(i, t) - P_{drive}(i, t))\Delta t \quad \text{for } t > 1 \quad (78)$$

in (78) parameter $\gamma(i, t)$ is used to set $P_{EV}(t)$ to zero when the EV is not available and $P_{drive}(i, t)$ is used to model the reduction of energy due to driving when the EV is not available. Additionally, $P_{drive}(i, t)$ helps by ensuring that (78) is valid over the entire simulation period, therefore preventing the use for conditional statements in case the EV is unavailable. Finally, a minimum departure charge can be set by the user using (79).

$$E_{EV}(i, t) = E_{EV}^{depart} \quad \text{for } t > t_{depart} \quad (79)$$

5.3.2.3 Energy Storage Degradation Model

The remaining capacity of the BES and every i th EV is required to determine the cost of degradation and to accurately optimize power management. The used model is based on the one presented in [268]. However, a depth of discharge dependency is added based on data presented in the same study. Fig. 60 shows the improved accuracy. The model is based on a single NMC cell; therefore, the power $P_X(i, t)$ is translated into the voltages and currents of a single cell using (80)-(81), assuming perfect cell balancing. In order to reduce the solving time, (80) is the linearized form of the open-circuit voltage of an NMC cell [269], as shown in Fig. 59. Next, the cyclic and calendar aging are calculated according to (83)-(85). Here a calendar degradation rate of 2% per year at 20°C is assumed [270]. This is linearized to a fixed percentage per time step c_6 . For every EV, the degradation due to driving is calculated based on the WLTC profile, assuming 2 trips of 23km on every weekday. The resulting degradation is averaged per time step and added to c_6 . Since the power rating of the EV and BES chargers is limited to 1C, which is far below the maximum C-rate of the cells, the power handling capability of the BES/EV will not be affected in its lifetime. However, to account for the increase in internal resistance, the efficiency is modelled as a function of remaining capacity, using (58). Here it is assumed that the

internal resistance is doubled when it reaches 70% remaining capacity [144, 150].

$$V_{oc}^{linear}(i, t) = N_{cell}^{series}(i) \left(3.42 + 0.7 \text{SoC}_X(i, t) \right) \quad \forall i, t \quad (80)$$

$$i_X^{cell}(i, t) = \frac{P_X(i, t)}{N_{cell}^{parallel}(i) V_{oc}^{linear}(i, t)} \quad \forall i, t \quad (81)$$

$$\Delta E_X^{\%}(i, t) = c_1 e^{c_2 |I_X^{cell}(i, t)|} \frac{c_3 D_X(i, t)}{c_4} |I_X^{cell}(i, t)| \Delta t \quad \forall i, t \quad (82)$$

$$\Delta E_X^{cycle}(i, t) = \left(\Delta E_X^{\%}(i, t) \right) \frac{E_X^{rated}(i)}{100}, \quad \forall i, t \quad (83)$$

$$\Delta E_X^{cal}(i, t) = \left(c_5 \sqrt{t} e^{-24kJ/RT} \right) \frac{E_X^{rated}(i)}{100} = \left(c_6 \Delta t \right) \frac{E_X^{rated}(i)}{100} \quad \forall i, t \quad (84)$$

$$\Delta E_X^{tot}(i) = \sum_{t=0}^T \left(\Delta E_X^{cycle}(i, t) + \Delta E_X^{cal}(i, t) \right) \quad \forall i, t \quad (85)$$

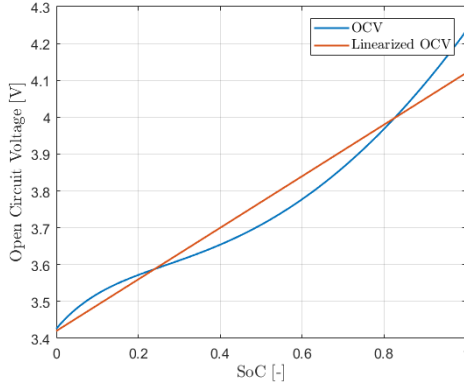


FIGURE 59: Open circuit voltage for a NMC battery cell [269] and its linearized variant

5.3.2.4 Frequency Containment Reserve Constraints

Finally, the primary frequency containment reserve (FCR) constraints. The available reserve capacity is determined as the difference between the components' maximum positive, negative or rated power (P_X^{max} , P_X^{min} , and P_X^{rated}) and the current/scheduled power $P_X(t)$. Taking into account power ratings, SoC limitations, both AC and DC power balances in the system,

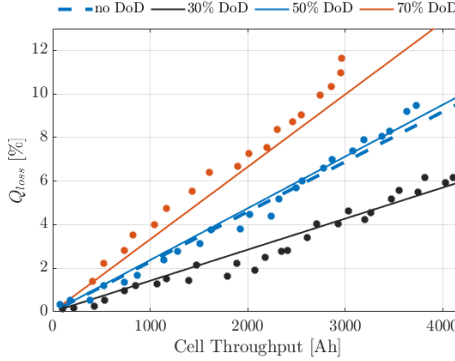


FIGURE 60: The dots indicate the results of the cell aging tests presented in [268]. The cells are tested at a C-rate of 3,5C, $T = 34^{\circ}\text{C}$ and with a DoD equal to 30, 50 and 70%.

and the total appliance and heating load. This concept per component is shown in Fig. 6 and is calculated analogously for up- and down regulation using (86)-(93) and (94)-(102), respectively.

$$P_{up}^{EV}(t) \leq \gamma(i, t) \sum_{i=1}^n \left(P_{EV}^{FCR}(i) \right) \forall t \quad (86)$$

$$P_{up}^{EV}(t) \leq \gamma(i, t) \sum_{i=1}^n \left(\frac{E_{EV}^{rated}(i) - E_{EV}(i, t)}{\Delta t} \right) \quad (87)$$

$$P_{up}^{BES}(t) \leq P_{BES}^{FCR} \quad \forall t \quad (88)$$

$$P_{up}^{BES}(i, t) \leq \frac{E_{BES}(i, t) - E_{BES}^{rated}}{\Delta t} \quad (89)$$

$$P_{up}^{BES}(t) \geq 0, \quad P_{up}^{EV}(t) \geq 0, \quad P_{up}(t) \geq 0 \quad \forall t \quad (90)$$

$$P_{up}(t) \leq \eta_{inv} \left(P_{up}^{EV}(t) + P_{up}^{BES}(t) \right) \quad \forall t \quad (91)$$

$$P_{up}(t) \leq P_{inv}^{rated}(t) - P_{inv}(t) \quad \forall t \quad (92)$$

$$P_{up}(t) \leq P_{grid}^{max}(t) - P_{inv}(t) + P_{appl}(t) + P_{heat}(t) \forall t \quad (93)$$

$$P_{dwn}^{EV}(t) \leq \gamma(i, t) \sum_{i=1}^n \left(P_{EV}^{FCR}(i) \right) \quad \forall t \quad (94)$$

$$P_{dwn}^{EV}(t) \leq \gamma(i, t) \sum_{i=1}^n \left(\frac{E_{EV}(i, t) - E_{EV}^{min}(i, t)}{\Delta t} \right) \quad (95)$$

$$P_{dwn}^{BES}(t) \leq P_{BES}^{FCR} \quad \forall t \quad (96)$$

$$P_{dwn}^{BES}(t) \leq \frac{E_{BES}(t) - E_{BES}^{min}(t)}{\Delta t} \quad (97)$$

$$P_{dwn}^{PV}(t) \leq P_{PV}(t) \quad \forall t \quad (98)$$

$$P_{dwn}^{PV}(t) \geq 0, P_{dwn}^{BES}(t) \geq 0, P_{dwn}^{EV}(t) \geq 0, P_{dwn}(t) \geq 0 \quad \forall t \quad (99)$$

$$P_{dwn}(t) \leq \eta_{inv} \left(P_{dwn}^{EV}(t) + P_{dwn}^{BES}(t) + P_{dwn}^{PV}(t) \right) \quad \forall t \quad (100)$$

$$P_{dwn}(t) \leq P_{inv}^{rated}(t) + P_{inv}(t) \quad \forall t \quad (101)$$

$$P_{dwn}(t) \leq P_{grid}^{max}(t) + P_{inv}(t) - P_{appl}(t) - P_{heat}(t) \quad \forall t \quad (102)$$

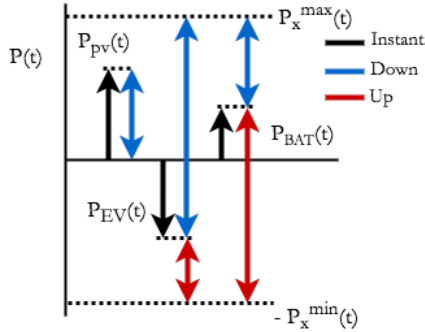


FIGURE 61: Concept of available reserve capacity shown per component (EV, PV, BES). The black arrows indicate the instantaneous powers, whereas the blue and red arrows represent the down- and up-regulation, respectively

In some countries FCR should be contracted symmetrically, in those cases (103) should be included. Finally, in order for the model to work in a moving horizon context, Eq(104),(105) are added to ensure that the power reserved in the day-ahead is actually available. Here $t + t_1 : t + t_2$ indicates the time frame in which the powers are reserved.

$$P_{up}(t) = P_{dwn}(t) \quad (103)$$

$$P_{FCR}^{up}(t + t_1 : t + t_2) = P_{FCR,sched}^{up}(t_1 : t_2) \quad (104)$$

$$P_{FCR}^{down}(t + t_1 : t + t_2) = P_{FCR,sched}^{down}(t_1 : t_2) \quad (105)$$

This concludes all constraints of the NLP model, and that concludes the section on optimal scheduling. In the next section the real-time control is used.

5.4 REAL-TIME CONTROL

Two different real-time control schemes have been developed, for the case with, and without, FCR. Both cases will be discussed separately in the following subsections.

5.4.1 without FCR

In case FCR is not included in the optimal scheduling, the main goal of the real-time control (RTC) error handling heuristics is to re-calculate the setpoints within each optimization step based on forecasting errors. This prevents drawing too much grid energy at high prices or feeding at low prices. Additionally, it prevents overloading the DC/AC converter by the optimal scheduling algorithm, which often tends to maximize inverter utilization based on forecasted average PV power. Fig. 62 shows the heuristics used in case no FCR capacity is reserved. The RTC inputs are the optimal

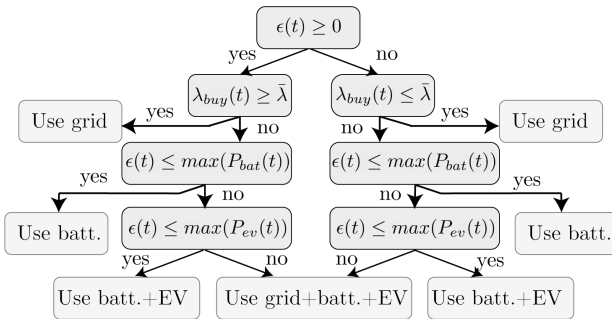


FIGURE 62: Flowchart of the real-time control scheme. Based on the forecasting error, the electricity price, and the available power from the EV and BES, the setpoints are recalculated.

setpoints of the current timestep, the predicted PV power and energy prices.

Next, based on the actual measurements and updated data, the real-time controller will update the EV and BES setpoints to account for the differences. This must be done as fast as possible to achieve the best results. Therefore, the simple but effective heuristics, shown in Fig. 62, are used. First, it checks whether the error $\epsilon(t)$ is positive, i.e. an excess of energy, according to Eq.(106).

$$\epsilon(t) = (P_{PV}^{act} - P_{PV}^{act}(t)) + (P_{load}^{fc} - P_{load}^{act}(t)) \quad (106)$$

Next, the current energy tariff $\lambda_{sell}(t)$ is compared to the expected average tariff $\hat{\lambda}$ of that day. Depending on the outcome, and the maximum available power from the BES or EV, the error is compensated using the BES, EV, or grid power. If the error exceeds the maximum available power of the BES (or EV), the total available power is used, and the remainder is compensated with the EV or grid.

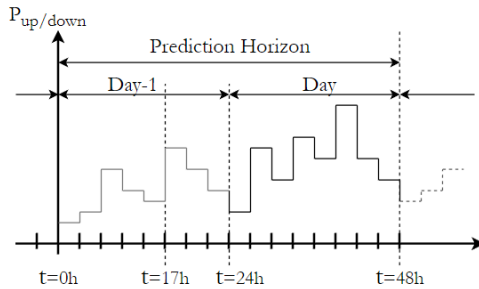


FIGURE 63: Moving horizon control window, with a prediction horizon equal to 48h. The FCR is procured every day at 17:00h the day ahead.

5.4.2 with FCR

When FCR is included in the optimal scheduling, a certain amount of reserve capacity is procured at 17:00h the day-ahead: 'day-1' in Fig. 63. Please note, if FCR is included, a minimum moving horizon window of 48 hours is required. The reserved FCR capacity has to be available during the contracted time ('day' in Fig. 63). Therefore, the EV and BES power are not recalculated based on forecasting errors. Instead, based on the grid frequency and the contracted reserve power, the total power provided for FCR is calculated based using a linear droop curve. Here the maximum contracted power is provided in case of a frequency deviation of $\pm 200\text{mHz}$.

The resulting additional FCR power is shared between both the EV and BES, and added to the optimal power setpoint. The additional power provided for FCR, causes the EV and BES energy capacities to deviate from the optimally calculated value. To prevent infeasibilities, and maintain the desired reserve capacity, a linear SOC management is added. The flowchart describing this is shown in Fig 64.

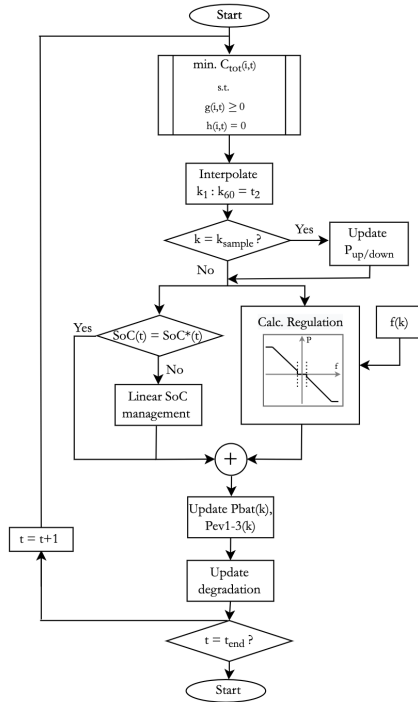


FIGURE 64: Flowchart representing the moving horizon control scheme incorporating optimal scheduling and FCR provision based on droop control

5.5 CASE STUDIES

The effectiveness of the proposed methodology is demonstrated using an office building with three EV chargers. Due to its fixed working hours and multiple EV charging spots, an office building is well suited for integrating regulatory services. The results will be compared using three use cases.

- **case 1:** The proposed model, assuming asymmetrical reserves.
- **case 2:** The proposed model, assuming symmetrical reserves.
- **case 3:** The proposed model, without FCR constraints (Eqs.(86)-(102).
- **case 4:** A particle swarm optimization (PSO) based component size optimization, combined with a rule-based power control algorithm based on the algorithm described in [249].

The simulations are run for a half year, based on data from January to June 2018, to capture all diurnal and seasonal variations. Here, we assume that the seasonal fluctuations in the first half of the year are similar to those in the second half of the year to reduce the solving time. Further examination shows that this does not affect the component sizes and therefore is a reasonable assumption. The electrical and heating demand profiles ($P_{load}(t)$ and $P_{heat}(t)$, respectively) are considered non-flexible and are obtained from [271], see Fig. 65 for two exemplary days. The EV charging patterns are obtained from [272] [273] and are summarized in Table 13. The PV irradiance data is obtained from the Dutch Meteorology Institute [274].

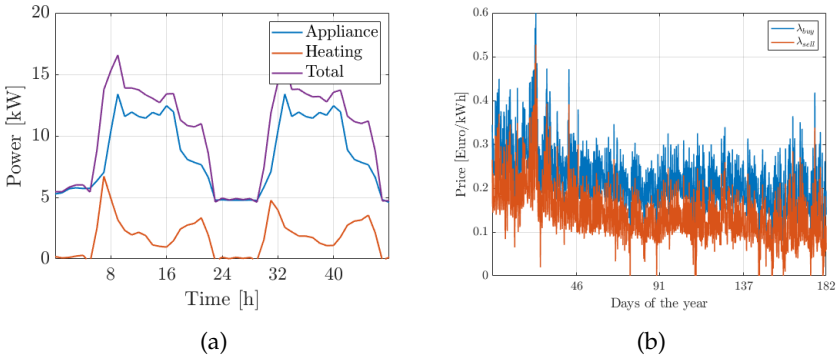


FIGURE 65: (a) Two exemplary days of the appliance and heating load ($P_{appl}(t), P_{heat}(t)$) obtained from [271]. (b): Energy buying price λ_{buy} , and selling price λ_{sell}

The electricity prices ($\lambda_{buy}, \lambda_{sell}$) are based on the Amsterdam Power Exchange (APX) day-ahead market, though yearly averaged around 20 cents/kWh to be comparable with current retail electricity prices. For the same reason, the FIT is chosen such that its average lies at 50% of the average retail price tariffs [249], see Fig. 8. Finally, the regulation prices are obtained from the Dutch frequency regulation market [264].

Quantity	Value
availability weekday	08:00h-18:00h
availability weekend	-
number of EVs	3
energy demand weekday (EV1-3)	15,30,5kWh

TABLE 13: EV demand [272] [273]

Type	Bounds	Price
PV system	0-50kWp	1500 €/kWp [275]
Battery system	0-200kWh	500 €/kWh [261]
BES charger	0-200kW	300 €/kW [276]
EV charger	0-200kW	350 €/kW [276]
Inverter	0-200kW	300 €/kW [259]

TABLE 14: Sizing variable prices and bounds

5.6 RESULTS: OPTIMAL SCHEDULING

In this section, the results will be discussed based on the three use cases described above. Besides the optimal power management, the optimization will determine the:

- Battery energy capacity E_{bat}^{max} [kWh]
- Battery charger power rating P_{bat}^{max} [kW]
- PV system power rating P_{pV}^{max} [kW]
- EV charger power rating P_{EV}^{max} [kW]
- Inverter power rating P_{inv}^{max} [kW]

The variable bounds are given in Table 14. The model has been solved with the CONOPT4 solver on the Generic Algebraic Modeling System (GAMS) on a desktop computer with a 3.6GHz Intel Xeon 4 core and 16GB RAM.

5.6.1 Optimal Power Management & Component Size

The power flows for the four cases are shown in Fig. 66-69, the optimal component sizes are given Table 16, and the optimal cost components are given in Table 15. The ratio's of operational capacity (P_X^{op}) to rated capacity (P_X^{rated}) for the BES and EV1-3 equal are also given in Table 16. The PV size

Variable	case 1	case 2	case 3	case 4
C_{grid}	€2280	€3233	€2808	€4131
C_{BES}	€1224	€1545	€334	€0
C_{EV}	€975	€972	€1060	€1037
$C_{PV+conv}$	€4620	€4065	€3218	€3060
C_{FCR}	€-4337	€-4710	€0	€0
C_{int}	€1002	€997.5	€567	€461
C_{total}	€5764	€6102.5	€7987	€8689

TABLE 15: Cost component for each use case

Variable	case 1	case 2	case 3	case 4
P_{PV}^{max}	50 kWp	44 kWp	50 kWp	50 kWp
E_{BES}^{max}	123.6 kWh	156 kWh	33.7 kWh	0 kWh
P_{BES}^{rated}	100 kW	91 kW	10 kW	0 kW
P_{BES}^{Op}	25 kW	18.8 kW	10. kW	0 kW
P_{EV}^{rated}	10 kW	5 kW	7.2 kW	2.8 kW
P_{EV1}^{Op}	6 kW	5 kW	7.2 kW	0 kW
P_{EV2}^{Op}	2.5 kW	3 kW	7.2 kW	0 kW
P_{EV3}^{Op}	5.7 kW	5 kW	7.2 kW	0 kW
P_{inv}^{max}	77 kW	78 kW	36.6 kW	46 kW

TABLE 16: Optimal component sizes for each use case

is equal to the maximum 50 kWp for all cases. This can be explained by the levelized cost of energy (LCOE) of PV, as calculated according to (107). Since the LCOE is lower than the FIT for 82% of the time, the PV system is a profitable investment and the optimization maximizes its size.

$$LCOE = \frac{V_{PV} P_{PV}^{max}}{\sum_{t=0}^T (P_{PV} \Delta t) T_{life} T_{sim}} = 0.0931 \text{€}/\text{kWh} \quad (107)$$

Notice that the PV-inverter power ratio is greater than one for cases 3 and 4. This is a result of the often low irradiance of the Dutch environment. By having a smaller inverter it better utilizes its entire power range. Another reason is that the EV, BES, and PV are all connected on the inverter's DC side and can therefore absorb part of its power. Contrary to the PV system, the BES is not a profitable investment for case 4. This is a result of the fact that there is already a good simultaneity between supply (PV) and demand (load, heating & EV). In combination with the fact that the

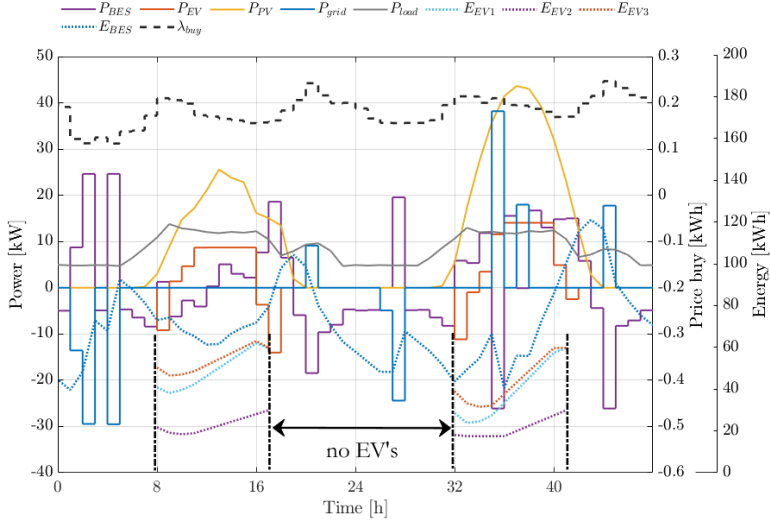


FIGURE 66: Optimally scheduled power flows for Case 1

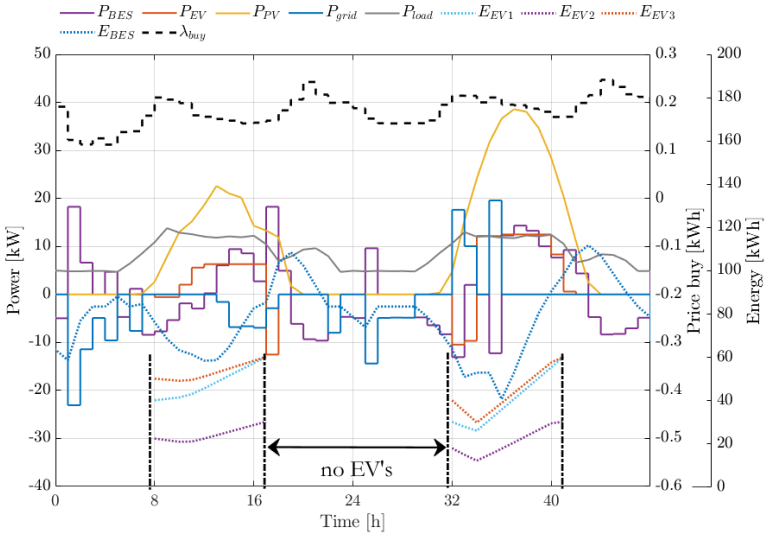


FIGURE 67: Optimally scheduled power flows for Case 2

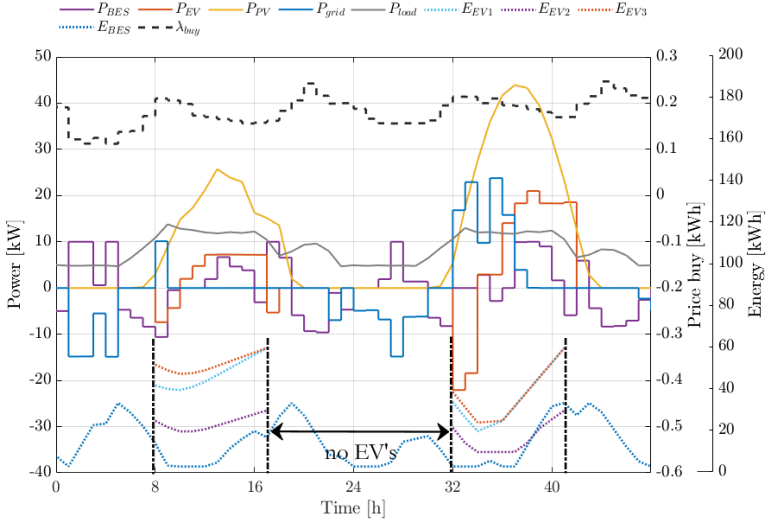


FIGURE 68: Optimally scheduled power flows for Case 3

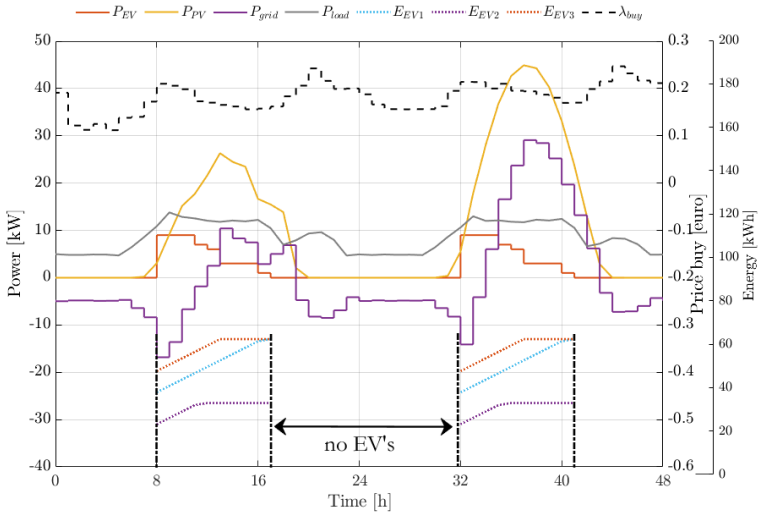


FIGURE 69: Optimally scheduled power flows for Case 4

BES is operated based on the net power in the system. Consequently, the BES is seldom used in winter; when heating demand is higher and solar irradiance is lower. This is different for cases 1-3, as the control anticipates on future supply and demand, it optimizes the BES's (dis)charging to take advantage of differences in electricity price. Similarly, the charging of the EVs is also optimized, and vehicle-to-grid (V2G) is used to minimize operational costs. As a result, the cost of grid energy for cases 1-3 is 44.8%, 21.7% and 32% lower compared to in case 4, respectively. The benefit of optimal power management is even higher for use cases with lower supply-demand simultaneity and/or lower PV output, such as residential buildings. Table III also shows the effect of the FCR market constraints; the power- and energy ratings of cases 1 and 2 are significantly higher than case 3, especially for case 1. Obviously, higher component ratings result in more reserve power available to be exchanged on the FCR market and more energy available to be arbitrated. Due to this increased revenue, the total costs were reduced by 27.8% and 23.6%, compared to case 3. The difference in power ratings demonstrates the importance of including the FCR constraints when optimizing component sizes. Note that optimal power management at the same time further lowers costs, as it calculates the optimum trade-off between operating capacity, reserve capacity, and degradation. The BES SoC profiles in Fig. 66-67 and the SoC histograms in Fig. 70 are an example of this.

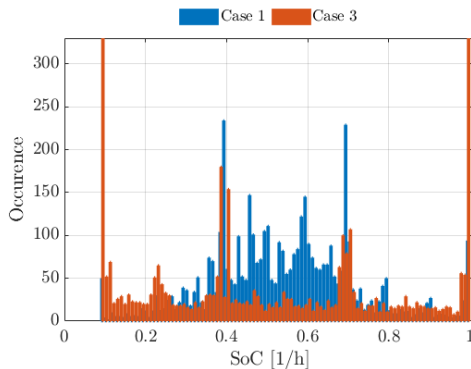


FIGURE 70: Occurrence of BES SoC [%] for cases 1 and 3. The case 1 BES operates mostly in the 30-80% region, to ensure that it always has reserve capacity available for FCR market participation.

These figures show that the case 1 BES is seldom completely charged or discharged, but remains mostly in the 30-80% SoC area. As a consequence, the BES always has up/down-regulation power available. Whereas the BES in case 3 generally uses its entire allowable SoC range. Based on the results presented so far it is concluded that FCR market participation can significantly increase the scheduled revenue. However, so far the effects of FCR provision, in terms of grid electricity costs and degradation, have not been taken into account. To analyze these additional costs, the optimal scheduling has to be performed in a moving horizon window, including the real-time control. This is discussed in the next section.

5.7 RESULTS: REAL-TIME CONTROL

In the following sections the real-time control (with FCR) is used to analyze the effect of FCR and component degradation on lifetime system costs.

5.7.1 Lifetime Net Present Costs

To consider the additional costs due to FCR provision and PV forecast uncertainty, the total lifetime Net Present Costs C_{NPC} and Return On Investment (ROI) periods are calculated using the proposed model in a moving horizon context as shown in Fig. 64. Here, the rules from a pilot study on prosumer FCR market participation in the Netherlands [262] are adopted, assuming asymmetrical aggregation and day-ahead procurement (as shown in Fig. 63) are used. The FCR power is bid hourly but provided in a one-minute resolution. In this analysis, 1-minute resolution PV data accounts for the PV forecasting errors. Consequently, the resulting power flows are all in a 1-minute resolution. Furthermore, the EV degradation is minimized, but the related costs are not factored in as the EVs are privately owned. The moving horizon window is simulated for a 15 year period. After which, C_{NPC} is calculated using (108).

$$C_{NPC} = C_{invest} - (C_{base} - C_{total}) \quad (108)$$

Here C_{base} is the demand only expense (appliance, heating and EV), and thus $(C_{base} - C_{total})$ are the energy management system's savings. Fig. 71b(a) shows that the ROI period equals 11.7 years, 12.3 years, 10.2 years, and 12.5 years for cases 1-4, respectively. Therefore all cases are profitable investments, achieving total lifetime profits of €22.7k, €-7.5k, €42.7k, €17.4k, respectively. However, after including the remaining second-life values of the BESs, as calculated according to (46)(47), the profits of cases 1-3 increase

further to €80k, €68.8k, €58.7k, respectively. The total savings, ROI, and lifetimes of cases 1-3 are summarized in Table 17. Different to the results obtained in Table 15 these results include the additional costs (or reduction in revenue) due to component degradation, PV forecasting errors, and FCR power provision. An example of the difference between optimal scheduled grid power and actual grid power is shown in Fig. 71a, which shows that power provided for FCR significantly deviates the grid power from its optimal schedule. As a result, the total grid energy cost increases by 29.4% and 22.2% for cases 1 and 2, respectively. As shown in Fig. 72b. This difference in grid power is provided by the BES and EVs, and this additional cycling can also increase the degradation of their batteries. As summarized in Fig. 72b, the BES degradation has increased by 2-4.5%, compared to the same case without FCR provision. Since the mean frequency deviation is close to zero, the additional degradation of the battery is less significant than the increase in grid energy costs. Nonetheless, despite these increased costs, it can be concluded that the FCR market can be effectively integrated with other revenue streams such as energy arbitrage and PV self-consumption and is an effective method for lowering overall costs. Furthermore, our results show that BES and EV 2nd-life value is a significant part of the overall lifetime profit. The effect of component degradation and 2nd-life value is discussed in more detail in the next section.

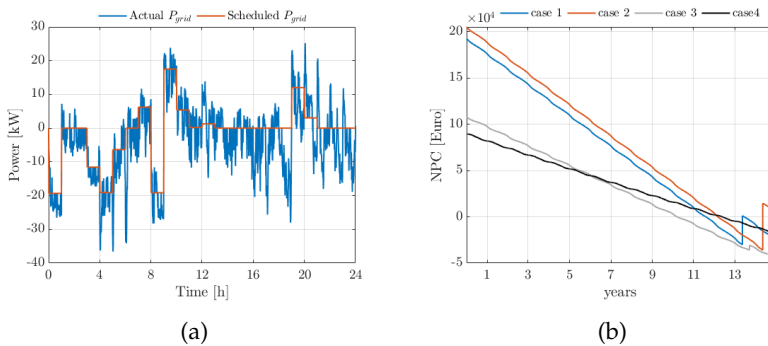


FIGURE 71: (a): Actual grid power including FCR power provision, versus optimally scheduled grid power. (b): Net Present Cost of the four analyzed cases (excluding second-life BES values).

	case 1	case 2	case 3	case 4
Cost savings[%]	460%	395%	337%	0
ROI [years]	11.7	12.3	10.2	12.5
Lifetime BES [years]	13.5	14.5	13.8	n.a.
Lifetime EV ₁ [years]	10.6	10.7	10.2	11.9
Lifetime EV ₂ [years]	8.2	8.6	8.6	9.5
Lifetime EV ₃ [years]	10.6	10.7	10.2	11.9

TABLE 17: Summary of results for cases 1-4. The percentage cost savings are calculated by comparing them with case 4.

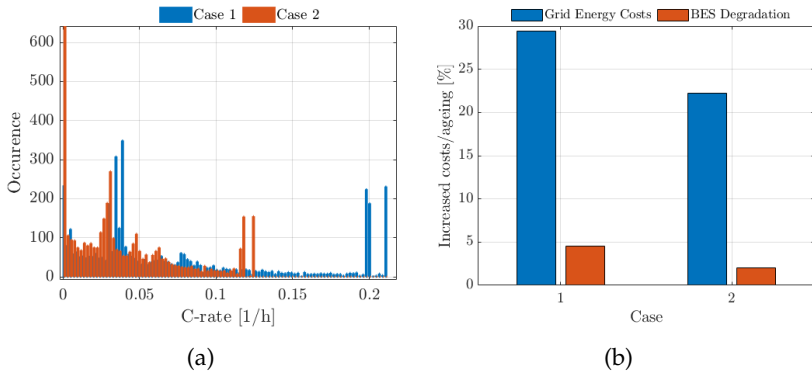


FIGURE 72: (a): Scheduled charging rate occurrence for the case 1-2 BES. The reduced charging rate of the case 2 BES is a reason for the reduced degradation. (b): Grid energy costs C_{grid} and FCR revenue C_{FCR} of the case 1 model in the first half year, versus the C_{grid} and C_{FCR} in the first half of year 13, just before BES replacement.

5.7.2 Effect of Component Degradation

The degradation of the EV, BES, and PV systems are calculated over the entire moving horizon period (15 years), and once these reach their end-of-life criteria of 70% remaining capacity, they are replaced and sold for their second-life value. This is observed in Fig. 71b(a) as the stepwise increase in cost. The resulting lifetimes of the EVs and BES are summarized in Table 17. The reduced degradation of case 2 with respect to case 1 can be explained by the fact that the case 2 BES operates at a lower C-rate, as shown in Fig. 72a. Additionally, the normalized throughput per cell of the case 2 BES is almost 52% lower compared to case 1. This is because the model

tries to maximize the FCR revenue, and due to the symmetrical bidding constraint, has less capacity available for other revenue streams such as energy arbitrage. Finally, please note that for both cases, the C-rates are much lower than the maximum allowable $2C$, due to the BES degradation model.

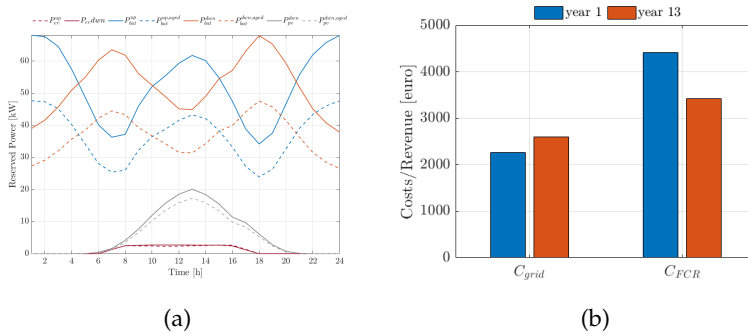


FIGURE 73: (a): Average scheduled reserve powers per hour in a day. The striped lines indicate the reserved powers of an aged system. (b): Grid energy costs C_{grid} and FCR revenue C_{FCR} of the case 1 model in the first half year, versus the C_{grid} and C_{FCR} in the first half of year 13, just before BES replacement.

To analyze the effectiveness of the degradation model, the case 1 model has been run without BES degradation model assuming a fixed 15 year lifetime over which the costs are annualized. The optimal BES size now became 97kWh with a rated power of 113kW, and since the 2nd-life value was not considered C_{BES} increased by 32%. When the degradation of the resulting BES profile was calculated, it was 17% higher than the case 1 BES, which would result in a 2 year and 4 month reduction of lifetime. Another important feature of the degradation model is calculating the available energy capacity. To examine the effect of component degradation on revenue, we examine the differences in revenue for case 1 in the first half year versus the first half of year 13, just before BES replacement. The resulting difference in grid energy costs and FCR revenue are shown in Fig. 73b, the regulation revenue decreased by 27.7% an almost one-to-one ratio with the degradation of the battery. Whereas C_{grid} increased by 14.9%. This shows the importance of calculating the degradation of components and the actual costs over their lifetime. Finally, the effect of PV and BES degradation on reserved capacity is shown in Fig. 73a. Here the dashed lines indicate the daily average, reserved capacities in the last half-year

before BES replacement. The degradation results in an almost one-to-one equivalent decrease of 29% and 14.5% of the reserved power for the BES and PV systems, respectively. Reducing total FCR revenue by 27.7%.

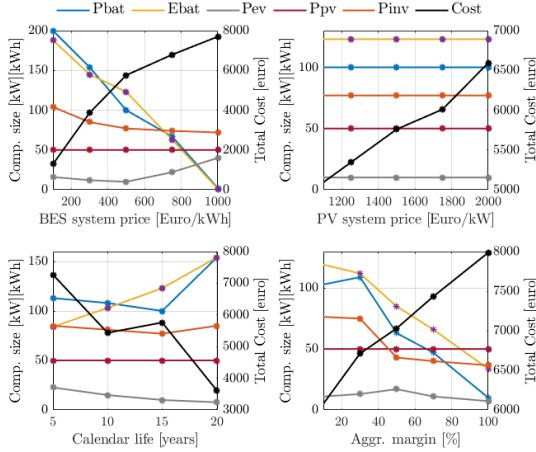


FIGURE 74: Sensitivity on input parameters and assumptions. The units on the y-axis or [kW] for all power related component sizes, [kWh] for energy related component size (Ebat), and [Euro] for the Cost.

5.7.3 Sensitivity Analysis

The last part of the results include a sensitivity analysis on the effect of the following input parameters and assumptions.

1. BES price per kWh: V_{BES}^{new}
2. PV system price per kWp: V_{PV}
3. BES Calendar life assumption: c_4
4. Aggregator profit margin: ϵ_{agg}

Fig. 74 shows the result of varying these input parameters on the optimal component sizes. It is concluded that the PV system price does not affect the result, apart from costs. Furthermore, if the battery prices fall in the future, the BES becomes even more profitable and also higher lifetime revenues can be obtained. Finally, the aggregator profit margin is concluded to be a very important parameter. Up to 30% it does not affect the component sizes much, apart from the revenue. However, for higher profit margins

the component ratings decrease, up to the point that they are equal to the values obtained for case 3.

5.8 CHAPTER CONCLUSIONS

This chapter presents the proposed two-level smart charging structure. The first level optimizes the power flows in a moving horizon window. Additionally, it finds the optimal component sizes based on the power management. The model includes constraints that allow it to reserve power for the FCR market. Based on our results, it is concluded that the highest revenue can be obtained when all aspects are optimally integrated. Additionally, our results show that the return on investment for BES systems is still too high for the simulated case without proper control. However, optimal power management adds additional business cases for the BES, such as energy arbitrage and FCR market participation, making the BES very profitable. The second level recalculates the EV and BES setpoints based on grid frequency deviation or PV forecasting errors, inside the optimization time steps. By implementing both levels in a moving horizon window, the significance of PV and BES degradation on total lifetime revenue has been investigated. It is concluded that including the FCR market increases lifetime cost-saving by 36% and 460% compared to optimal power management without FCR market participation and nonoptimal power management, respectively. Furthermore, our results showed the importance of including component degradation and FCR power provision on lifetime revenue. Investigating the effect of degradation on the reserved powers showed an almost one-to-one correlation, resulting in a total decrease in FCR market participation of 27.7% at the end of the BES lifetime.

Part III
INTEGRATION & VALIDATION

This chapter, the final part of this thesis, discusses the integration of the two preceding parts: the power electronics and the smart charging algorithm. The result is a three-level smart charging algorithm that includes the optimal scheduling algorithm and real-time error handler proposed in Chapter 5, and the embedded control layer presented in Chapter 3. The results show the importance of the proposed three-level control structure, and its protections. Finally, the proposed smart charging scheme is compared to two other charging schemes: direct PV charging and fixed-rate charging. The results show that the proposed charging scheme reduces the total cost of energy, and solves the problem of poor BES utilization of existing charging methods.

This chapter is based on:

- J₃ W. Vermeer, M. Wolleswinkel, J. Schijfelen, G.R. Chandra Mouli, P. Bauer, *Design of a 10kW Multi-Port EV Smart Charging System Integrating EV, PV, and Battery*, 2023, (under review for) *IEEE Transactions on Transportation Electrification*
- J₂ W. Vermeer, M. Wolleswinkel, J. Schijfelen, G.R. Chandra Mouli, P. Bauer, *Three-Mode Variable-Frequency Modulation for the Four-Switch Buck-Boost Converter: a QR-BCM vs. TCM Case Study and Control Implementation*, 2022, (under review at) *IEEE Transactions on Industrial Electronics*
- J₁ W. Vermeer, G.R. Chandra Mouli, P. Bauer, *Optimal Sizing & Control of a PV-EV-BES Charging System Including Primary Frequency Control and Component Degradation*, 2022, *IEEE Open Journal of Industrial Electronics*

6.1 INTRODUCTION

This chapter comprises the final part of this thesis: the integration of part I: the multi-port converter, and part II: the smart charging algorithm, to develop the proposed EV-PV-BES integrated smart charging system. First the integration of the algorithm, communication and converter are discussed. After which, the smart charging results are discussed, and compared to two other charging schemes.

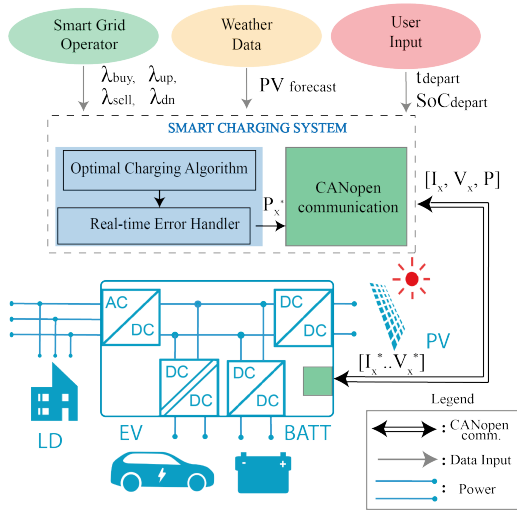


FIGURE 75: The three layers of the control hierarchy. The top level is an optimal scheduling algorithm, followed by a real-time error handler which sends the setpoints to the embedded V-I controllers.

6.2 INTEGRATING SMART CHARGING CONTROL

Fig. 75 shows the schematic of the proposed smart charging system. The final setup used for the smart charging experiments is shown in Fig. 76. The first two layers of the control scheme are implemented on a lab computer. Here a Python script is used to implement the moving horizon window, including the CANopen implementation for communication with the converter. In this moving horizon window GAMS is called to solve the NLP problem discussed in Chapter 5. In this case, the component sizes are fixed

to 10kW, with a 20kWh BES and assuming EVs with 80kWh energy capacity. The output of the NLP model includes the optimal power setpoints of the EV and BES, the forecasted PV power, and forecasted energy price of the current optimization timestep. These are recalculated using the real-time controller. Finally, the control loops presented in Chapter 3 ensure closed loop control. In this chapter, FCR market participation and component sizing are not included, hence the objective function of the smart charging algorithm is reduced to Eq.(109).

$$C_{total} = C_{grid} + C_{EV}^{\delta} + C_{BES}^{\delta} \quad (109)$$

here,

- C_{total} is the total cost to be minimized
- C_{EV}^{δ} represents the operational cost due to EV battery degradation
- C_{BES}^{δ} represents the operational cost due to BES battery degradation

Next, in the RTC, these power setpoints are converted to current setpoints, by measuring the voltages of the EV and BES. Additionally, the actual PV power is measured and compared to the forecasted power. Then, the flowchart, shown in Fig. 62 in Chapter 5, is used to recalculate the EV and BES setpoints based on the forecasting error and current energy price. Finally, the resulting setpoints are send over the CAN bus, to the corresponding converter.

To ensure continuous control, the real-time controller is implemented in a separate Python thread in parallel to the MHW. This way, the real-time controller is always running, even when the optimization is still solving. This is especially useful for problems with long solving times, such as mixed-integer or stochastic optimization problems. The timestep of the real-time controller is set to the lowest possible value. Still, it has to include the round-trip delay of measurement reading, calculation, setpoint writing, and setpoint settling time. For this reason, the timestep is set to two seconds. After the RTC has sent the setpoints, the embedded control ensures fast and safe control of the converter currents and voltages.

6.3 RESULTS: SMART CHARGING

Fig. 76 shows the experimental setup with the proposed power electronic converter. The smart charging script runs on a PC with python and GAMS.

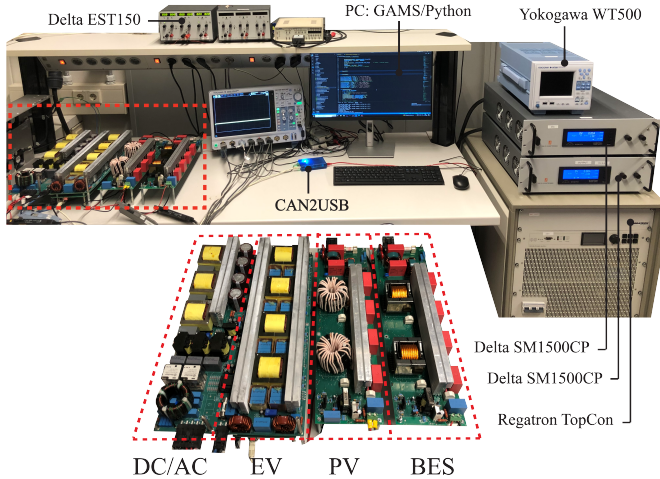


FIGURE 76: Experimental setup consisting of the proposed multi-port converter, a PC running the smart charging algorithm, power supplies emulating the EV, PV and BES, a CAN2USB converter for communication, and an auxiliary supply.

Here the optimal setpoints are calculated in a 24-hour ahead moving horizon window. Next, the real-time control updates the optimal setpoints based on the measurement of actual PV power. The updated setpoints are then sent using a CAN-to-USB converter to the power electronic hardware, which uses the embedded control to the current and voltage. The PV, EV, and BES ports are emulated using the power supplies. To account for PV forecasting errors, a pseudo-random forecasting error is added on top of the measurement. This error is randomly sampled every optimization step, with the minimum and maximum error percentage converging from $\pm 40\%$ to $\pm 10\%$ as the forecasts approaches the current time. Fig. 77(a) shows the EV, PV, and BES output currents as controlled by the proposed smart charging system. Additionally, the horizontal bars show the calculated (and forecasted in case of PV) optimal charging powers in 7.5 minutes resolution, for optimization steps $k = 1..4$. The experimental waveforms are a part of the full-day simulation shown in 77(b), as indicated by the striped box. To explain the operation, the results shown in Fig. 77(a), are discussed per optimization timestep k :

- During $k = 1$, the forecasted PV power is significantly higher than the actual power. As a result, the power balance on the DC-link ($P_{dc} = P_{pv} - P_{ev} - P_{bes}$) is significantly exceeded in the majority of the period. However, the real-time control continuously updates the BES and EV setpoints, based on the PV power measurement. If the power balance then still is exceeded within the real-time control time step, the BES power is further curtailed using the cascaded DC-bus voltage control loop. At the end of $k = 1$, the PV power exceeds its forecast, but since the energy price is lower than the 24-hour mean, the real-time control prevents feeding in power and therefore first increases the charging power of the BES, followed by increasing the EV setpoint.
- In the next optimization step $k = 2$, the PV forecast was more accurate. In the first half, the excess PV power increases both the EV and BES charging power. In the second half, the PV power drops below its forecast and the BES power is again curtailed to prevent overloading the DC/AC converter.
- During $k = 3$, the BES setpoint is reduced. In this case, the PV power exceeds its forecast. This excess power is used to increase the BES power since the energy prices are still below average, and the BES still has plenty of capacity available. The BES power is increased based on the excess PV power, resulting in a net DC-link power of 10kW.
- The same holds during $k = 4$ when the forecasted PV is lower than its actual value and the control is tracking the available PV power.

Throughout $k = 1..4$, the energy price is low and to optimally utilize this temporal advantage all three control layers are required to keep the inverter operating at its maximum capacity, but not exceed it. In this example, the maximum BES charging power was artificially limited at 7kW to show the heuristic steps of the real-time control (at the end of $k = 1$). Furthermore, the results show that the EV setpoint is relatively constant, as the real-time control first tries to use the BES for error handling. This helps to ensure that the EV departure charge setpoint is met.

Finally, Fig. 77(a) shows a couple of communication failures, indicated by the asterisks. These were caused by a failing CAN-to-USB converter, the cause of which is out of the scope of this paper. These failures, however, can result in a time-out of a CAN node and temporarily stop the operation of the corresponding converter. Such failures can lead to under and overvoltages

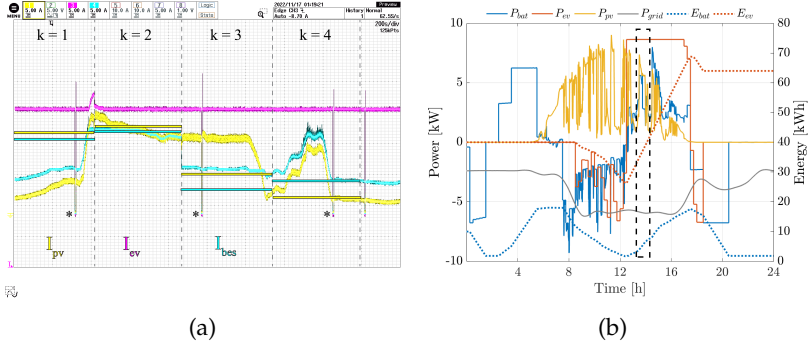


FIGURE 77: (a): Experimental waveform and (b): theoretical simulation based on the proposed optimal charging scheme including real-time control and protection.

on the DC link, resulting in semiconductor failure. However, thanks to the cascaded control loops all modules shut down when the failure occurs.

6.3.1 Charging Scheme Comparison

The effectiveness of the proposed charging scheme is analyzed by comparing it to two other charging schemes: Firstly, direct PV charging, shown in Fig. 78(a) and (b). Here the EV is charged directly based on PV power and the battery power is determined based on the net power, as calculated according to Eq.(110).

$$P_{BES} = P_{net} = P_{PV} - P_{EV} - P_{load} \quad (110)$$

Secondly, with fixed rate charging the EV is charged with a fixed charging power and the battery is charged based on the net power P_{net} , as shown in Fig. 78(c) and (d). For all three cases, it is assumed that the EV is available between 08:00-18:00h [277].

For both direct PV charging and fixed rate charging it can be concluded that the BES is hardly used. Only during the night and early morning, the residual capacity in the BES is used to power the load. However, in both cases, the BES is barely charged after it is depleted, simply because there is no excess power. This points to the conclusions made in section I.A, which states that stationary battery storage is not cost-effective for EV-PV charging applications when simple heuristic control schemes are used. Using the proposed control scheme the BES power is optimized to

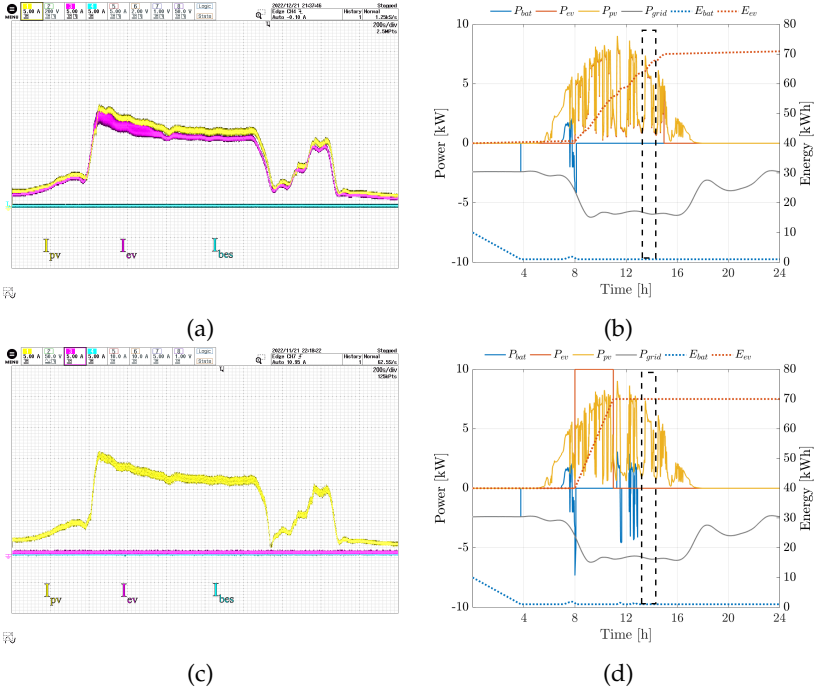


FIGURE 78: (a): experimental waveform of constant charging. (b): full day simulation of the proposed control, (c): full day simulation of direct PV charging, (d): full day simulation of constant charging. In the experiments, the EV and BES voltages are constant at 475V, and 450V respectively. The PV voltage is determined by the MPPT algorithm and varies between 375 and 420V.

utilize energy price differences, resulting in better utilization of the available energy storage capacity. To compare, the BES is idle for 6.6%, 65.5%, and 72.8% for the proposed charging, PV charging, and fixed rate charging, respectively. This increased utilization, however, reduces the lifetime of the battery. Therefore, a battery degradation model is included in the optimal scheduling algorithm to calculate the trade-off between operational costs such as energy trading, battery lifetime, and battery second-life value. [278]. The degradation model often reduces the charging power, to find the trade-off between temporal advantages in energy price and battery degradation. The final costs, as calculated according to eq.(109), are summarized in Table 18. Using the proposed smart charging method, it was possible to reduce

the total costs by 44.7% and 48.7% compared to PV- and fixed-rate charging, respectively, despite an increase in battery degradation. This cost reduction was achieved by trading energy between high and low prices. This, however, also reduced load autonomy γ by 66% and 28%, with respect to PV- and fixed-rate charging respectively, as calculated according to eq.(111).

$$\gamma = \frac{\sum_{t=0}^{t=24h} P_{load}dt + E_{ev}}{\sum_{t=0}^{t=24h} |P_{grid}dt|} \tag{111}$$

Here dt represents the timestep in hour, P_{grid} the grid power in kW, and E_{ev} is the charging requirement of the EV in kWh.

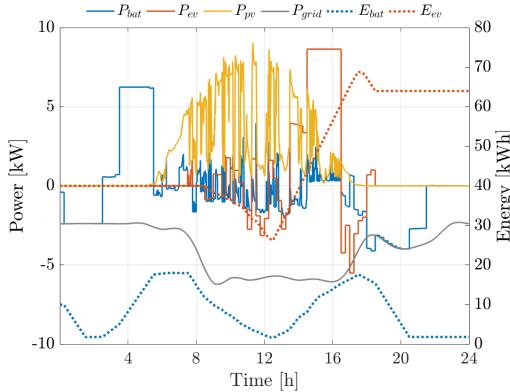


FIGURE 79: Full day simulation of the proposed control with reduced FIT.

Cost	Prop. high FIT	Prop. low FIT	PV	Fixed
C_{grid}	€11.9619	€12.55	€18.9	€20.47
C_{EV}^{δ}	€1.43	€1.32	€1.30	€1.307
C_{BES}^{δ}	€2.33	€1.85	€1.37	€1.32
C_{total}	€15.73	€15.73	€21.6	€23.2

TABLE 18: Cost comparison for the three charging schemes under high FIT.

Note that the reduced load autonomy is a direct result of the high feed-in tariff (FIT). When the FIT drops below the energy buying tariff, as is the case for the low FIT, the objective of the proposed smart charging method shifts

from energy trading towards energy preserving, i.e. it tries to minimize grid energy intake and maximize PV-self consumption to reduce the cost, and as a result also automatically increases the load autonomy. The results for the proposed charging method are shown in Fig. 79 and Table 18. Despite slightly larger grid energy costs, the total costs are approximately equal due to the lower cost of degradation. Additionally, in case of lower FIT the load autonomy is increased by 15% and 17% compared to PV- and fixed-rate charging. It is therefore concluded that the smart charging can significantly lower the total cost of energy in solar-powered smart charging systems, especially, when the FIT and solar production are low.

6.4 CHAPTER CONCLUSIONS

This chapter discussed the integration the two-level smart charging algorithm onto the solar-powered EV-BES charger. It is concluded that the cascaded V-I control loops are especially important for smart charging applications as our results indicate that the optimal scheduling often tends to maximize inverter utilization, based on a forecast of PV power. As a result, forecasting errors can lead to overloading, if not dealt with accordingly. The results show that inverter overloading can be prevented using the proposed cascaded control loops.

Finally, the proposed smart charging scheme is compared to direct PV charging and fixed rate charging. The results show, that despite a slightly higher battery degradation, the total cost (including the cost of degradation) can be reduced by 44.7% and 48.7% compared to PV and fixed charging, respectively. Furthermore, it was shown that without smart charging the energy storage utilization is poor. Previous studies have already shown that, as a result of poor utilization, the return on investment period of stationary energy storage combined with rooftop PV and EV charging can be too long. The proposed smart charging system can improve the business case of stationary storage, by reducing the total cost. As a result, it also helps by increasing load independence, especially in the case of low FIT.

CONCLUSION

It was concluded in Chapter 1 that, due to congestion and the inability to reinforce the entire electricity grid, a smart and local solution was required to help with the increasing electrification of the energy demand, while also increasing the penetration of RESs. More specifically, the solution should promote the supply of local demands by locally generated renewable energy. It was also argued that due the intermittent and temporal variability of RES, energy storage, both vehicular (EV) and stationary (BES), is required to reduce energy feed-in and increase PV self-consumption. However, currently, PV-BES systems are often less cost-effective for small-scale prosumers due to the poor utilization of the available flexibility in the system.

The goal of this thesis was to incentivize small-scale prosumer EV-PV-BES integration through their intelligent operation using a multi-port power converter. This goal was divided into three parts. First, the power electronic hardware was discussed in part I. Next, part II discussed the smart charging control system. Finally, the integration of parts I and II, and their experimental results, were discussed in Part III. In the following sections, the main findings obtained from all proceeding chapters are summarized for each research question.

7.1 REGARDING RESEARCH QUESTIONS

How to design a highly-efficient 10kW converter suitable for both PV and BES applications?

Both PV and BES voltages are specified from 300 to 900V, this wide voltage range increases the operating range of the proposed multi-port converter. Additionally, since both PV and BES do not require galvanic isolation, it allows the same buck-boost converter to be used for both the PV and BES ports, in both single-phase and three-phase converters. This reduces the design effort and can therefore help in reducing the overall system cost.

7.1.1 Multi-mode QR-BCM modulation

The FSBBC was chosen for this application because of its bidirectional buck and boost capabilities, relatively low component count, and relatively low component stress due to its non-inverting nature. In Chapter 3, the different modulation strategies for the FSBBC were summarized. It was concluded that the highest efficiencies reported in the literature were achieved with variable-frequency operation. Additionally, it was concluded that the constant-frequency operation has an inherent disadvantage in terms of higher peak and RMS currents. For this reason, the focus of Chapter 2 was on deriving a variable-frequency modulation scheme that maximizes efficiency. Based on a loss analysis, multi-mode QR-BCM operation was chosen. The multi-mode operation resulted in power control discontinuities at the borders of each operating mode. To overcome this, a feed forward mode transition control scheme was implemented. This control scheme utilized the drain-source voltage of the switches to generate a trigger that allowed each interleaved phase to transition towards the new operating mode, at the inductor current zero crossing of the corresponding phase.

7.1.2 Modulation comparison

The experimental results of Chapter 2 showed that it was possible to transition between operating modes at full power, without a loss of output power, no output voltage swing, and limited output current ripple. Furthermore, our results show that the proposed prototype matches the highest reported efficiency of the FSBBC in the literature, despite of a higher power per phase and input voltage range. To further test the proposed modulation, it was benchmarked with three other soft-switching modulation schemes; TCM, B-QR-BCM, and QCM. The results show that the adoption of QR-BCM allows to simplify the converter control without a loss of efficiency. Additionally, it achieved higher efficiency compared to B-QR-BCM and QCM in the entire operating range, apart from unity voltage gain, where QCM achieved the highest efficiency. In terms of power density, QCM required a slightly smaller input capacitor and inductor, and B-QR-BCM required the largest passive component volume.

How to design a multi-port converter for a 10kW EV, PV, BES, and AC grid-integrated smart charging system?

7.1.3 *Topology selection*

The DC-integrated multi-port topology was chosen in this thesis. The advantage of the DC bus is the modularity and scalability of the DC link capacitor bank, that allows to easily scale up the power rating of each port without completely redesigning the system. Additionally, it requires the least amount of conversion steps, four in total, one for each port. Whereas, the high-frequency transformer and AC-grid integration require 5 and 6 conversion steps, respectively. The modular design allows each port to be designed independently. This simplifies the design, but increases the design effort required.

In this work, a two level DC-AC converter controlled using sinusoidal PWM is used for the bidirectional AC grid connection. Next, a 4-phase interleaved flyback converter is used for isolated EV charging. Finally, two interleaved four-switch buck-boost converters are used for both the PV and BES ports. To achieve a high power density and high efficiency, QR-BCM modulation is applied to all DC-DC converters in the system. Furthermore, all power semiconductors are made from silicon carbide, and koolmu powder iron cores are used.

7.1.4 *Closed-loop control*

A crucial aspect of a multi-port converter is to maintain power balance in the coupling link. For the DC-integrated topology this means a power balance on the DC bus. In the proposed converter, this is done by controlling the DC bus voltage, primarily using the DC-AC converter. This is significantly easier to control than preventing magnetic core saturation using a MAB converter. As long as the DC-AC converter can maintain the DC bus voltage, the control of the other ports is completely decoupled and they can be designed independently. This allows the PV port to have an independent control loop that performs maximum power point tracking, to maximize renewable energy generation. Additionally, it allows the setpoints of the EV and BES points to be optimized by the smart charging algorithm. However, in the proposed converter all ports are made up of 10kW modules. Therefore, the combined power of the PV and bidirectional EV and BES ports exceeds the power rating of the DC-AC converter. It is therefore vital that power balance is always ensured, especially because of the intermittent nature of PV. To achieve this, all ports are equipped with cascaded I-V control loops that can curtail their current based on the DC-link voltage, and output voltages. This is done sequentially. Primarily, the DC-AC converter maintains balance by

controlling the grid current. If the nominal power of the DC-AC converter is exceeded the DC-bus voltage will start to deviate. When the DC bus voltage deviates more than 20V from its nominal setpoint, the BES converter starts curtailing its current. If it deviates any further the PV and EV will start to curtail and if necessary shutdown. This sequential cascaded control ensures stability, safety and modularity. This modularity enables the converter's design to be divided per port. The experimental results of Chapter 3 validate the operation of the proposed control loops and its protections.

How to model Li-ion battery degradation and how to mitigate it?

In Chapter 1, LIB degradation was identified as a crucial characteristic that could hold back the integration of BES and V2x. Therefore, to properly assess the operational cost of energy storage, it is required to model how LIBs age over time and how this is affected by the operating conditions. In Chapter 4, four different methods for ageing estimation were introduced. It was concluded that empirical and semi-empirical models are the most relevant for the use in smart charging applications, as their relative simplicity makes them applicable in optimization problems. However, they require large test matrices in order to accurately fit the model onto the data. Since test conditions are usually limited and based on accelerated testing conditions, EMs are prone to oversimplifying the ageing behaviour. The goal of Chapter 4 was to review EMs and obtain a good understanding of ageing behaviour, and empirical modelling techniques for LIB ageing. Focusing on operational stress factors and their interdependence, modelling techniques, limitations, and challenge.

For smart charging applications it is important to make a distinction between calendar and cycle life, as charging is often not a continuous operation. For calendar ageing temperature, SoC and time are the main stress factors. Whereas for cyclic ageing also C-rate, DoD, and throughput have to be taken into account. The role and interdependence of these operational stress factors was reviewed, to better understand the potential modelling limitations and the effect operating conditions have on battery lifetime.

First, the main ageing mechanisms were identified. In most studies, SEI growth is identified as the largest contributor to degradation in the first part of a battery's lifetime. Later, when the SEI layer has passivated the rate of ageing reduces, until other processes such as lithium plating start to occur. In contrast to the SEI layer, lithium plating has a non-passivation

character and often becomes the dominant aging factor later in the battery's lifetime. In this thesis, the focus was on the first part of the battery life. Therefore, the main ageing mechanisms to focus on was SEI growth.

It was concluded that SEI growth is most often modelled using a power-law relationship with respect to time for calendar ageing, and with respect to throughput for cyclic ageing. Here an exponential factor, in the range of 0.5-1, is generally used to model the passivating character of SEI layer growth. For temperatures above 20-25°C, the Arrhenius law is most often used. Generally, the rate of ageing increases for higher temperatures. However, for cyclic ageing low temperatures induce other ageing effects such as lithium plating, and ageing again increases when temperatures drop under room temperature. Since many studies used accelerated ageing conditions, such as high temperatures, this was often not modelled. Furthermore, temperature showed a strong correlation with C-rate. In general, higher C-rates result in more degradation. However, multiple studies showed that the effect of C-rate reduced as the temperature increased. Similarly, the effect of C-rate increases for low temperatures. This was again not modelled in most studies. Finally, it was demonstrated that the effect of SoC on calendar ageing is frequently oversimplified to an exponentially increasing curve with respect to SoC, due to the limited number of testing conditions. In reality, the rate of ageing is strongly related to the anode voltage, which rather increases in discrete steps. This is further complicated during cycling as low SoCs result in increased impedance, which aggravates ageing. Additionally, during cycling, the effect of SoC was closely related to the DoD. Often an increasing DoD is presumed to increase ageing. However, in reality, the effect of DoD seemed closely related to the traversing of the electrode phase changes, or plateaus.

To conclude the model presented in [143] has been selected as the best fitting model for the smart charging algorithm, because of the following reasons:

- The model has been designed for the NMC-LMO chemistry, a chemistry which is considered a viable candidate for both EV and stationary applications [213]. Similarly, the same model can thus be used for both the EV and BES.
- The test conditions described in [143] match with real-life conditions for both EV and BES applications. More specifically, most cells were cycled between 10°C and 34°C. Additionally, at every temperature a variety of different C-rates and DoDs were tested. Not only focussing

on accelerated testing conditions, but also including low C-rates (0.5C-6.5C) and DoD (10%-90%). This DoD-dependence was not originally included in the model presented in [143]. However, based on their presented data, this dependency has been added in the next chapter.

- It is one of the few models which has modelled the temperature dependence of C-rate.
- The model is part of the few models which separate calendar ageing and cyclic ageing, by subtracting the calendar ageing results from their cyclic ageing results.

How to optimally size and control the integrated EV, PV, BES smart charging system to reduce the cost of energy and provide ancillary services?

To achieve intelligent operation, and obtain a cost-effective system, it is important to have a control structure that optimally utilizes the flexibility obtained from the multi-directional smart charging system. Similarly, it is important that the component ratings are properly sized based on each use case. A tool is therefore required that utilizes the modular, and multi-directional, nature of the multi-port system, and adapts it based on specific use cases. The smart charging algorithm proposed in Chapter 5 achieves this, by being able to simultaneously optimize the component ratings based on the optimal power management of the components. When used for sizing the components, only the NLP model is required. For optimal power management, and implementation on the converter a three-level control structure is used. The first two-layers are discussed in Chapter 5, whereas the third embedded layer is discussed in Chapter 2.

7.1.5 *Optimal sizing*

The optimal sizing results of Chapter 5 show that for all four cases the PV system was sized to its maximum. This is due to the fact that the LCOE of the PV installation is lower than the cost of grid electricity, resulting in a profitable investment. The sensitivity of the PV system costs was analyzed, but showed almost no variability in component ratings when varying from 1000 euro/kWp to 2000 euro/kWp.

Next, it was concluded that the highest revenue can be obtained when all aspects are optimally integrated. Furthermore, the simulation results showed that the return on investment for BES systems is still too high for the case without optimal power management. This supports the argument

of Chapter 1, which mentioned that the low LCOE of PV-BES systems discourages the use of BES for prosumer PV applications. When optimal power management is included into the optimal sizing algorithm the components ratings were increased to increase the flexibility of the system. Despite higher investment costs and increased battery degradation, the optimal power management resulted in a 44.8%, 21.7% and 32% reduction in total cost, for cases 1-3 with respect to case 4 respectively. The highest cost savings were obtained for case 1, which included asymmetrical FCR reserve. In this case, the algorithm finds an optimal battery power and size of 100kW and 123.6kWh, a 371% increase in battery capacity compared to case 3. The algorithm uses 75% of its power rating and a significant part of its battery capacity for FCR scheduling. The optimal scheduling algorithm operates the battery mostly in 30-80% SoC region, to have both up- and down regulation capacity available.

7.1.6 *Smart Charging Control*

The first level of the proposed smart charging control system consists of the NLP model, which is being solved in a 48-hour-ahead moving horizon window to continuously recalculate the setpoints based on changing conditions and forecasts.

The second layer consists of a real-time controller that recalculates the NLP model setpoints, in between the 15-minute optimization timesteps. The RTC can fill two primary tasks. When FCR market participation is included, the main tasks of the RTC is to adapt the EV and BES setpoints to ensure that the correct amount of FCR power is provided. Without FCR market participation, the RTC adapts the setpoints of the EV and BES based on a comparison of the actual and forecasted conditions of the energy prices and PV power.

Finally, the third layer is the embedded control layer. As mentioned above, and in Chapter 2, the embedded control layer is used to provide closed-loop control of the smart charging setpoints. Additionally, the cascaded control loops are also used to protect the inverter from overloading.

It is concluded in Chapter 5 that the optimal power management significantly increases the cost-effectiveness of the integrated system compared to non-optimal power management. This is achieved by adding additional business cases, such as energy arbitrage and FCR market participation, making the system very profitable. For the simulated case including FCR market participation, the lifetime cost-savings were increased by 36% and 460% compared to optimal power management without FCR market partic-

ipation and nonoptimal power management, respectively. If the second-life value of the BES system is taken into account. Furthermore, by using the moving horizon window combined with the proposed real-time control over a 15 year simulation period, the significance of PV and BES degradation on total lifetime revenue has been investigated. The results showed an almost one-to-one correlation, resulting in a total decrease in FCR market participation of 27.7% at the end of the BES lifetime (70% remaining energy capacity).

In Chapter 6, the implementation of the proposed control structure on the multi-port converter is discussed, and the experimental results are shown. The experimental results prove the necessity of all three levels of control. First, the optimal layer optimally utilizes the flexibility gained from the energy storages, and provides the smart charging of the EV and BES. Next, the RTC recalculates the setpoints based on forecasting errors. However, occasionally the embedded control still had to curtail the BES power to account for the fast changing PV power.

What are the benefits of the proposed smart charging system compared to conventional AC-integrated charging systems?

7.1.7 Modular DC-integrated multi-port converter

To begin, the DC-integrated multi-port converter reduces the amount of DC-AC power converters required. Additionally, the modular design of the power electronic hardware allows to easily scale up the system up to above 100kW. This modularity allows the optimal sizing algorithm to customize the design based on different applications, without redesigning the system. Based on the lifetime cost reductions achieved in Chapter 5, it is concluded that this can significantly lower the cost of the system. Furthermore, by designing a FSBBC that can be used for both PV and BES applications, the flexibility gained from similar specifications is utilized to reduce the total design effort and hereby reduce the cost of the system. Additionally, a novel modulation scheme is proposed for achieving high efficiencies over a wide voltage and power range. The large operating range increases the flexibility of PV, BES, and DC/AC converter configurations.

7.1.8 *Integrated Hierarchical Smart Charging Control*

As indicated by in Chapter 1, and supported by the optimal sizing results of Chapter 5, power electronic integration alone does not fully utilize the flexibility obtained from energy storage. Therefore, the most significant advantage is obtained by integrating the smart charging algorithm on the multi-port power converter. As shown in Chapter 5 and 6, the proposed smart charging algorithm significantly reduces the lifetime system cost by optimally utilizing the flexibility from the components. Additionally, as shown in Chapter 6, the proposed smart charging control increases the energy independence of the local loads.

In this thesis, a cost minimization objective was chosen for the smart charging system. This objective was chosen to increase the incentivize for prosumers to install the proposed system, and hereby indirectly promote RES integration and sustainable transportation. Additionally, the advantage of cost minimization is that it allows for the autonomous integration of multiple business cases, all previously inaccessible by conventional charging systems. A summary of these business cases integrated in the smart charging algorithm is included below:

1. Energy Arbitrage.
2. FCR market participation.
3. Peak shaving.
4. Battery lifetime optimization.

The capability to find the trade-off between multiple business cases increases the employability of the system, and gives the prosumer the flexibility for a wider variety of applications. However, most of all, it significantly increases the revenue obtained by the system, which show that smart charging can significantly reduce the operational cost by increasing the utilization of energy storage and optimizing its performance over the entire lifetime of the EV and BES. It herewith overcomes the short comings of conventional PV-BES systems, which often show a very poor utilization of the energy storage capacity. This is confirmed by the results of Chapters 5 and 6 Finally, the integration of peak shaving and FCR market participation supports the decentralized energy grid.

To conclude, the flexibility gained by the proposed smart charging systems begins with the power electronic hardware, which offer great potential flexibility in terms of configuration and by allowing vehicular energy storage using V2x. Next, this potential flexibility is optimally utilized by the

smart charging algorithms which not only adapts based on current conditions, but also includes the optimization of future operation, and even battery lifetime, as well.

7.2 FUTURE WORK

Smart charging has become increasingly popular in recent years. However, existing studies generally focused on either hardware or algorithms. This thesis tried to bridge that gap by improving both power electronic hardware and smart charging technology, followed by integrating them. Now that this is done, future work can focus more on practical integration and improvements.

7.2.1 *Ancillary service control for DC-AC converter*

To begin, some of the features included in the smart charging algorithm were not yet possible to implement in the hardware. Peak shaving, for example, was integrated in the optimal scheduling and real-time control. However, to provide a hard constraint on the metered grid power, the embedded control requires fast and accurate metering of the local load and PV power. Furthermore, appropriate control needs to be integrated to deal with the intermittency of the local load and PV generation, to be able to provide a hard cap on grid power.

7.2.2 *Stand alone off-grid operation*

Additionally, the converter can be adapted for stand-alone off-grid operation. To achieve this, the DC/AC converter controls should be updated to include islanded operation, including the ability to transition between grid-connected operation and grid-forming operation, for both balanced and balanced three-phase loads. Additionally, the cascaded control of the BES system should be updated to be able to maintain power balance on the DC link, whenever the DC/AC converter is in grid-forming mode.

7.2.3 *Benchmarking smart charging algorithms*

Now that the smart charging is not only in the theoretical realm anymore, it is important to benchmark different smart charging approaches using hardware. One of the current trends in optimal scheduling problems is the use

of stochastic optimization. Stochastic smart charging problems calculate the charging powers taking into account the stochastic probability of different variables. The solving time of stochastic problems is usually longer than deterministic problems, but might provide a higher accuracy.

7.2.4 *Artificial Intelligence for parameter estimation*

In this thesis, many input parameters such as EV arrival and departure time were considered known. This is a fair assumption, considering that it could be provided by the user. However, the flexibility and autonomy of the system could be improved by estimating similar parameters, using artificial intelligence for example.

APPENDIX

8.0.1 Loss modelling

Total losses are comprised of the conduction losses P_{cond} , core losses P_{core} , switching losses (under ZCS) P_{switch}^{ZCS} , capacitor losses P_{cap} , and auxiliary losses (only for experimental measurements: PCB and fuse conduction losses). These are calculated according to Eq.(112)-(114).

$$P_{cond}^x = I_{rms,x}^2 R_{on}(T, I) \quad \& \quad P_{core} = c_1 f_{eq}^{\alpha-1} \hat{B}^\beta f_s V \quad (112)$$

Here x denotes switch S_x . The core losses are calculated according to [279], using:

$$f_{eq} = \frac{2}{\Delta B^2 \pi^2} \int_0^T \frac{dB^2}{dt} dt, \quad \text{with} \quad \hat{B} = \frac{\Delta B}{2} \quad (113)$$

Finally, the switching and capacitor losses are calculated by:

$$P_{switch}^{ZCS} = \frac{1}{2} C_{ds} V_{ds}^2 \quad \& \quad P_{cap} = RMS(I_{Cx})^2 ESR(f_s) \quad (114)$$

Here V_{ds} is the turn-off voltage under quasi resonance, and $ESR(f_s)$ denotes the electric series resistance of a capacitor as a function of switching frequency f_s .

8.0.2 Passive component sizing

The inductor power density is based on the energy they process per period, according to Eq.(115). Here I_{pk} is the peak inductor current. Next, the capacitors are sized to achieve a maximum voltage ripple of $dV = 10V$. Their capacitance C_x is then determined according to Eq.(115), here Q_x is the total charge stored during one cycle, of side x .

$$W_L = \frac{1}{2} \max(i_L(t))^2 \quad \& \quad C_x = Q_x / dV \quad (115)$$

BIBLIOGRAPHY

1. Netbeheer NL. *Capaciteitskaart elektriciteitsnet* <https://capaciteitskaart.netbeheernederland.nl>.
2. European Commission Eurostat. *SHARES (Renewables)* <https://ec.europa.eu/eurostat/web/energy/data/shares>.
3. Netherlands Enterprise Agency. *Electric Vehicles Statistics in the Netherlands* <https://www.rvo.nl/onderwerpen/duurzaam-ondernemen/energie-en-milieu-innovaties/elektrisch-rijden/stand-van-zaken/cijfers>.
4. Resch, M., Bühler, J., Schachler, B. & Sumper, A. Techno-Economic Assessment of Flexibility Options Versus Grid Expansion in Distribution Grids. *IEEE Transactions on Power Systems* **36**, 3830 (2021).
5. Kost, C., Shammugam, S., Fluri, V., Peper, D., Davoodi Memar, A. & Schlegl, T. Techno-Economic Assessment of Flexibility Options Versus Grid Expansion in Distribution Grids. *IEEE Transactions on Power Systems* **36**, 3830 (2021).
6. Smith, K. *Battery Lifespan* <https://www.nrel.gov/transportation/battery-lifespan.html>.
7. Chandra Mouli, G. R. *System design for a solar powered electric vehicle charging station for workplaces* PhD thesis (2016).
8. Rijksoverheid. *Afbouw salderingsregeling* <https://www.rijksoverheid.nl/documenten/kamerstukken/2022/07/01/afbouw-salderingsregeling>.
9. Yilmaz, M. & Krein, P. T. Review of the Impact of Vehicle-to-Grid Technologies on Distribution Systems and Utility Interfaces. *IEEE Transactions on Power Electronics* **28**, 5673 (2013).
10. Lee, Y.-J., Khaligh, A. & Emadi, A. A Compensation Technique for Smooth Transitions in a Noninverting Buck–Boost Converter. *IEEE Transactions on Power Electronics* **24**, 1002 (2009).
11. Jia, L., Sun, X., Zheng, Z., Ma, X. & Dai, L. Multimode Smooth Switching Strategy for Eliminating the Operational Dead Zone in Noninverting Buck–Boost Converter. *IEEE Transactions on Power Electronics* **35**, 3106 (2020).

12. Zhang, N., Zhang, G. & See, K. W. Systematic Derivation of Dead-Zone Elimination Strategies for the Noninverting Synchronous Buck–Boost Converter. *IEEE Transactions on Power Electronics* **33**, 3497 (2018).
13. Urkin, T. & Peretz, M. M. Digital CPM Controller for a Non-Inverting Buck–Boost Converter With Unified Hardware for Steady-State and Optimized Transient Conditions. *IEEE Transactions on Power Electronics* **35**, 8794 (2020).
14. Qin, Y., Li, S. & Hui, S. Y. Topology-Transition Control For Wide-Input-Voltage-Range Efficiency Improvement and Fast Current Regulation in Automotive LED Applications. *IEEE Transactions on Industrial Electronics* **64**, 5883 (2017).
15. Huang, P.-C., Wu, W.-Q., Ho, H.-H. & Chen, K.-H. Hybrid Buck–Boost Feedforward and Reduced Average Inductor Current Techniques in Fast Line Transient and High-Efficiency Buck–Boost Converter. *IEEE Transactions on Power Electronics* **25**, 719 (2010).
16. Chen, X., Pise, A. A., Elmes, J. & Batarseh, I. Ultra-Highly Efficient Low-Power Bidirectional Cascaded Buck-Boost Converter for Portable PV-Battery-Devices Applications. *IEEE Transactions on Industry Applications* **55**, 3989 (2019).
17. Li, X., Liu, Y. & Xue, Y. Four-Switch Buck–Boost Converter Based on Model Predictive Control With Smooth Mode Transition Capability. *IEEE Transactions on Industrial Electronics* **68**, 9058 (2021).
18. Ren, X., Ruan, X., Qian, H., Li, M. & Chen, Q. Three-Mode Dual-Frequency Two-Edge Modulation Scheme for Four-Switch Buck–Boost Converter. *IEEE Transactions on Power Electronics* **24**, 499 (2009).
19. Muro, K., Nabeshima, T., Sato, T., Nishijima, K. & Yoshida, S. *H-bridge buck-boost converter with dual feedforward control* in 2009 International Conference on Power Electronics and Drive Systems (PEDS) (2009), 1002.
20. Redl, R., Sokal, N. & Balogh, L. A novel soft-switching full-bridge DC/DC converter: analysis, design considerations, and experimental results at 1.5 kW, 100 kHz. *IEEE Transactions on Power Electronics* **6**, 408 (1991).
21. Yu, Z., Kapels, H. & Hoffmann, K. F. *Extreme High Efficiency Non-Inverting Buck-Boost Converter for Energy Storage Systems* in PCIM Europe 2016; International Exhibition and Conference for Power Electronics, Intelligent Motion, Renewable Energy and Energy Management (2016), 1.

22. Waffler, S. & Kolar, J. W. A Novel Low-Loss Modulation Strategy for High-Power Bidirectional Buck + Boost Converters. *IEEE Transactions on Power Electronics* **24**, 1589 (2009).
23. Zhou, Z., Li, H. & Wu, X. A Constant Frequency ZVS Control System for the Four-Switch Buck–Boost DC–DC Converter With Reduced Inductor Current. *IEEE Transactions on Power Electronics* **34**, 5996 (2019).
24. Liu, Q., Qian, Q., Ren, B., Xu, S., Sun, W. & Li, H. A New Modulation Strategy for Four-switch Buck-boost Converter with Reduced Freewheeling Current in 2020 *IEEE Applied Power Electronics Conference and Exposition (APEC)* (2020), 2104.
25. Tian, L., Wu, X., Jiang, C. & Yang, J. A Simplified Real-Time Digital Control Scheme for ZVS Four-Switch Buck-Boost With Low Inductor Current. *IEEE Transactions on Industrial Electronics* **69**, 7920 (2022).
26. Yu, J., Liu, M., Song, D., Yang, J. & Su, M. A Soft-Switching Control for Cascaded Buck-Boost Converters Without Zero-Crossing Detection. *IEEE Access* **7**, 32522 (2019).
27. Yu, Z., Kapels, H. & Hoffmann, K. F. A novel control concept for high-efficiency power conversion with the bidirectional non-inverting buck-boost converter in 2016 *18th European Conference on Power Electronics and Applications (EPE'16 ECCE Europe)* (2016), 1.
28. Xia, K., Li, Z., Qin, Y., Yuan, Y. & Yuan, Q. Minimising peak current in boundary conduction mode for the four-switch buck–boost DC/DC converter with soft switching. *IET Power Electronics* **12**, 944 (2019).
29. Fang, J., Ruan, X., Huang, X., Dong, R., Wu, X. & Lan, J. A PWM Plus Phase-Shift Control for Four-Switch Buck-Boost Converter to Achieve ZVS in Full Input Voltage and Load Range. *IEEE Transactions on Industrial Electronics* **69**, 12698 (2022).
30. Liu, Q., Qian, Q., Zheng, M., Xu, S., Sun, W. & Wang, T. An Improved Quadrangle Control Method for Four-Switch Buck-Boost Converter With Reduced Loss and Decoupling Strategy. *IEEE Transactions on Power Electronics* **36**, 10827 (2021).
31. Yu, Z., Kapels, H. & Hoffmann, K. F. High Efficiency Bidirectional DC-DC Converter with Wide Input and Output Voltage Ranges for Battery Systems in *Proceedings of PCIM Europe 2015; International Exhibition and Conference for Power Electronics, Intelligent Motion, Renewable Energy and Energy Management* (2015), 1.

32. Stahl, G., Rodriguez, M. & Maksimovic, D. *A high-efficiency bidirectional buck-boost DC-DC converter in 2012 Twenty-Seventh Annual IEEE Applied Power Electronics Conference and Exposition (APEC) (2012)*, 1362.
33. Yeh, C.-S., Zhao, X. & Lai, J.-S. *An investigation on zero-voltage-switching condition in synchronous-conduction-mode buck converter in 2017 IEEE Energy Conversion Congress and Exposition (ECCE) (2017)*, 1728.
34. Guo, F., Inoa, E., Choi, W. & Wang, J. Study on Global Optimization and Control Strategy Development for a PHEV Charging Facility. *IEEE Transactions on Vehicular Technology* **61**, 2431 (2012).
35. Krishnaswami, H. & Mohan, N. Three-Port Series-Resonant DC-DC Converter to Interface Renewable Energy Sources With Bidirectional Load and Energy Storage Ports. *IEEE Transactions on Power Electronics* **24**, 2289 (2009).
36. Bandyopadhyay, S., Purgat, P., Qin, Z. & Bauer, P. A Multiactive Bridge Converter With Inherently Decoupled Power Flows. *IEEE Transactions on Power Electronics* **36**, 2231 (2021).
37. Di Benedetto, M., Lidozzi, A., Solero, L., Crescimbin, F. & Bifaretti, S. *Hardware design of SiC-based Four-Port DAB Converter for Fast Charging Station in 2020 IEEE Energy Conversion Congress and Exposition (ECCE) (2020)*, 1231.
38. Qian, Z., Abdel-Rahman, O., Hu, H. & Batarseh, I. *An integrated three-port inverter for stand-alone PV applications in 2010 IEEE Energy Conversion Congress and Exposition (2010)*, 1471.
39. Waltrich, G., Duarte, J. L. & Hendrix, M. A. M. *Multiport converter for fast charging of electrical vehicle battery: Focus on DC/AC converter in IECON 2011 - 37th Annual Conference of the IEEE Industrial Electronics Society (2011)*, 3626.
40. Bhattacharjee, A. K., Kutkut, N. & Batarseh, I. Review of Multiport Converters for Solar and Energy Storage Integration. *IEEE Transactions on Power Electronics* **34**, 1431 (2019).
41. Nasir, M., Khan, H. A., Hussain, A., Mateen, L. & Zaffar, N. A. Solar PV-Based Scalable DC Microgrid for Rural Electrification in Developing Regions. *IEEE Transactions on Sustainable Energy* **9**, 390 (2018).
42. Askarian, I., Pahlevani, M. & Knight, A. M. Three-Port Bidirectional DC/DC Converter for DC Nanogrids. *IEEE Transactions on Power Electronics* **36**, 8000 (2021).

43. Restrepo, M., Morris, J., Kazerani, M. & Cañizares, C. A. Modeling and Testing of a Bidirectional Smart Charger for Distribution System EV Integration. *IEEE Transactions on Smart Grid* **9**, 152 (2018).
44. Kisacikoglu, M. C., Kesler, M. & Tolbert, L. M. Single-Phase On-Board Bidirectional PEV Charger for V2G Reactive Power Operation. *IEEE Transactions on Smart Grid* **6**, 767 (2015).
45. Gurkaynak, Y., Li, Z. & Khaligh, A. A novel grid-tied, solar powered residential home with plug-in hybrid electric vehicle (PHEV) loads in 2009 *IEEE Vehicle Power and Propulsion Conference* (2009), 813.
46. Singh, B., Verma, A., Chandra, A. & Al-Haddad, K. Implementation of Solar PV-Battery and Diesel Generator Based Electric Vehicle Charging Station. *IEEE Transactions on Industry Applications* **56**, 4007 (2020).
47. Saeed, J., Niakinezhad, M., Wang, L. & Fetnando, N. An Integrated Charger with Hybrid Power Source Using PV Array for EV Application in 2019 *IEEE 13th International Conference on Compatibility, Power Electronics and Power Engineering (CPE-POWERENG)* (2019), 1.
48. Gamboa, G., Hamilton, C., Kerley, R., Elmes, S., Arias, A., Shen, J. & Batarseh, I. Control strategy of a multi-port, grid connected, direct-DC PV charging station for plug-in electric vehicles in 2010 *IEEE Energy Conversion Congress and Exposition* (2010), 1173.
49. Singh, S. A., Carli, G., Azeez, N. A. & Williamson, S. S. Modeling, Design, Control, and Implementation of a Modified Z-Source Integrated PV/Grid/EV DC Charger/Inverter. *IEEE Transactions on Industrial Electronics* **65**, 5213 (2018).
50. Goli, P. & Shireen, W. PV Integrated Smart Charging of PHEVs Based on DC Link Voltage Sensing. *IEEE Transactions on Smart Grid* **5**, 1421 (2014).
51. Kim, D.-H., Cheo, G.-Y. & Lee, B.-K. Design and Control of an Optimized Battery Charger for an xEV Based on Photovoltaic Power Systems. *Journal of Electrical Engineering and Technology* **9**, 1602 (2014).
52. Verma, A., Singh, B., Chandra, A. & Al-Haddad, K. An Implementation of Solar PV Array Based Multifunctional EV Charger. *IEEE Transactions on Industry Applications* **56**, 4166 (2020).
53. Monteiro, V., Pinto, J. G. & Afonso, J. L. Operation Modes for the Electric Vehicle in Smart Grids and Smart Homes: Present and Proposed Modes. *IEEE Transactions on Vehicular Technology* **65**, 1007 (2016).

54. Khan, O., Hredzak, B. & Fletcher, J. E. *A Reconfigurable Multiport Converter for Grid Integrated Hybrid PV/EV/Battery System* in 2022 IEEE 16th International Conference on Compatibility, Power Electronics, and Power Engineering (CPE-POWERENG) (2022), 1.
55. Acharige, S. S. G., Haque, M. E., Arif, M. T., Hosseinzadeh, N. & Saha, S. *A Solar PV Based Smart EV Charging System with V2G Operation for Grid Support* in 2021 31st Australasian Universities Power Engineering Conference (AUPEC) (2021), 1.
56. Verma, A. & Singh, B. *Multi-Objective Reconfigurable Three-Phase Off-Board Charger for EV*. *IEEE Transactions on Industry Applications* **55**, 4192 (2019).
57. Lenka, R. K., Panda, A. K., Patel, R. & Guerrero, J. M. *PV Integrated Multifunctional Off-Board EV Charger With Improved Grid Power Quality*. *IEEE Transactions on Industry Applications* **58**, 5520 (2022).
58. Honarmand, M., Zakariazadeh, A. & Jadid, S. *Integrated scheduling of renewable generation and electric vehicles parking lot in a smart microgrid*. *Energy Conversion and Management* **86**, 745 (2014).
59. Chandra Mouli, G. R. *Charging electric vehicles from solar energy: Power converter, charging algorithm and system design* (2014).
60. Hava, A., Kerkman, R. & Lipo, T. *Simple analytical and graphical methods for carrier-based PWM-VSI drives*. *IEEE Transactions on Power Electronics* **14**, 49 (1999).
61. Liserre, M., Blaabjerg, F. & Hansen, S. *Design and control of an LCL-filter-based three-phase active rectifier*. *IEEE Transactions on Industry Applications* **41**, 1281 (2005).
62. Mozos, A., Chandra Mouli, G. R. & Bauer, P. *Evaluation of Topologies for a Solar Powered Bidirectional Electric Vehicle Charger*. *IET Power Electronics* **12** (2019).
63. Chandra Mouli, G. R., Schijffelen, J. H., Bauer, P. & Zeman, M. *Design and Comparison of a 10-kW Interleaved Boost Converter for PV Application Using Si and SiC Devices*. *IEEE Journal of Emerging and Selected Topics in Power articles* **5**, 610 (2017).
64. Doyle, M., Fuller, T. F. & Newman, J. *Modeling of Galvanostatic Charge and Discharge of the Lithium/Polymer/Insertion Cell*. **140**, 1526 (1993).

65. Jafari, M., Khan, K. & Gauchia, L. Deterministic models of Li-ion battery aging: It is a matter of scale. *Journal of Energy Storage* **20**, 67 (2018).
66. Northrop, P. W. C., Pathak, M., Rife, D., De, S., Santhanagopalan, S. & Subramanian, V. R. Efficient Simulation and Model Reformulation of Two-Dimensional Electrochemical Thermal Behavior of Lithium-Ion Batteries. **162**, A940 (2015).
67. Darling, R. & Newman, J. Modeling Side Reactions in Composite Li y Mn₂O₄ Electrodes. **145**, 990 (1998).
68. Ramadass, P., Haran, B., Gomadam, P. M., White, R. & Popov, B. N. Development of First Principles Capacity Fade Model for Li-Ion Cells. **151**, A196 (2004).
69. Christensen, J. & Newman, J. A Mathematical Model for the Lithium-Ion Negative Electrode Solid Electrolyte Interphase. **151**, A1977 (2004).
70. Randall, A. V., Perkins, R. D., Zhang, X. & Plett, G. L. Controls oriented reduced order modeling of solid-electrolyte interphase layer growth. *Journal of Power Sources* **209**, 282 (2012).
71. Barré, A., Deguilhem, B., Grolleau, S., Gérard, M., Suard, F. & Riu, D. A review on lithium-ion battery ageing mechanisms and estimations for automotive applications. *Journal of Power Sources* **241**, 680 (2013).
72. Schmalstieg, J., Käbitz, S., Ecker, M. & Sauer, D. U. A holistic aging model for Li(NiMnCo)O₂ based 18650 lithium-ion batteries. *Journal of Power Sources* **257**, 325 (2014).
73. Nejad, S., Gladwin, D. & Stone, D. A systematic review of lumped-parameter equivalent circuit models for real-time estimation of lithium-ion battery states. *Journal of Power Sources* **316**, 183 (2016).
74. Wang, Z., Ma, J. & Zhang, L. State-of-Health Estimation for Lithium-Ion Batteries Based on the Multi-Island Genetic Algorithm and the Gaussian Process Regression. *IEEE Access* **5**, 21286 (2017).
75. Berecibar, M., Devriendt, F., Dubarry, M., Villarreal, I., Omar, N., Verbeke, W. & Van Mierlo, J. Online state of health estimation on NMC cells based on predictive analytics. *Journal of Power Sources* **320**, 239 (2016).
76. Pan, H., Lü, Z., Wang, H., Wei, H. & Chen, L. Novel battery state-of-health online estimation method using multiple health indicators and an extreme learning machine. *Energy* **160**, 466 (2018).

77. Yang, D., Wang, Y., Pan, R., Chen, R. & Chen, Z. State-of-health estimation for the lithium-ion battery based on support vector regression. *Applied Energy* **227**. Transformative Innovations for a Sustainable Future – Part III, 273 (2018).
78. Liu, K., Hu, X., Wei, Z., Li, Y. & Jiang, Y. Modified Gaussian Process Regression Models for Cyclic Capacity Prediction of Lithium-Ion Batteries. *IEEE Transactions on Transportation Electrification* **5**, 1225 (2019).
79. Li, Y., Liu, K., Foley, A. M., Zülke, A., Berecibar, M., Nanini-Maury, E., Van Mierlo, J. & Hoster, H. E. Data-driven health estimation and lifetime prediction of lithium-ion batteries: A review. *Renewable and Sustainable Energy Reviews* **113**, 109254 (2019).
80. Vetter, J., Novák, P., Wagner, M., Veit, C., Möller, K.-C., Besenhard, J., Winter, M., Wohlfahrt-Mehrens, M., Vogler, C. & Hammouche, A. Ageing mechanisms in lithium-ion batteries. *Journal of Power Sources* **147**, 269 (2005).
81. Broussely, M., Biensan, P., Bonhomme, F., Blanchard, P., Herreyre, S., Nechev, K. & Staniewicz, R. Main aging mechanisms in Li ion batteries. *Journal of Power Sources* **146**. Selected papers presented at the 12th International Meeting on Lithium Batteries, 90 (2005).
82. Han, X., Lu, L., Zheng, Y., Feng, X., Li, Z., Li, J. & Ouyang, M. A review on the key issues of the lithium ion battery degradation among the whole life cycle. *eTransportation* **1**, 100005 (2019).
83. Han, X., Ouyang, M., Lu, L., Jianqiu, L., Zheng, Y. & Li, Z. A Comparative Study of Commercial Lithium Ion Battery Cycle Life in Electrical Vehicle: Aging Mechanism Identification. *Journal of Power Sources* **251**, 38 (2014).
84. Scarfogliero, M., Carmeli, S., Castelli-Dezza, F., Mauri, M., Rossi, M., Marchegiani, G. & Rovelli, E. Lithium-ion batteries for electric vehicles: A review on aging models for vehicle-to-grid services, 1 (2018).
85. Ahmadian, A., Sedghi, M., Elkamel, A., Fowler, M. & Aliakbar Golkar, M. Plug-in electric vehicle batteries degradation modeling for smart grid studies: Review, assessment and conceptual framework. *Renewable and Sustainable Energy Reviews* **81**, 2609 (2018).

86. R. Xiong L. Li, J. Towards a smarter battery management system: A critical review on battery state of health monitoring methods. *Journal of Power Sources* **405**, 18 (2018).
87. Berecibar, M., Gandiaga, I., Villarreal, I., Omar, N., Van Mierlo, J. & Van den Bossche, P. Critical review of state of health estimation methods of Li-ion batteries for real applications. *Renewable and Sustainable Energy Reviews* **56**, 572 (2016).
88. Lucu, M., Martinez-Laserna, E., Gandiaga, I. & Camblong, H. A critical review on self-adaptive Li-ion battery ageing models. *Journal of Power Sources* **401**, 85 (2018).
89. Lipu, M. H., Hannan, M., Hussain, A., Hoque, M., Ker, P. J., Saad, M. & Ayob, A. A review of state of health and remaining useful life estimation methods for lithium-ion battery in electric vehicles: Challenges and recommendations. *Journal of Cleaner Production* **205**, 115 (2018).
90. Birkl, C. R., Roberts, M. R., McTurk, E., Bruce, P. G. & Howey, D. A. Degradation diagnostics for lithium ion cells. *Journal of Power Sources* **341**, 373 (2017).
91. Barré, A., Deguilhem, B., Grolleau, S., Gérard, M., Suard, F. & Riu, D. A review on lithium-ion battery ageing mechanisms and estimations for automotive applications. *Journal of Power Sources* **241**, 680 (2013).
92. Kalaga, K., Rodrigues, M.-T. F., Trask, S. E., Shkrob, I. A. & Abraham, D. P. Calendar-life versus cycle-life aging of lithium-ion cells with silicon-graphite composite electrodes. *Electrochimica Acta* **280**, 221 (2018).
93. Han, X., Lu, L., Zheng, Y., Feng, X., Li, Z., Li, J. & Ouyang, M. A review on the key issues of the lithium ion battery degradation among the whole life cycle. *eTransportation* **1**, 100005 (2019).
94. Sarasketa-Zabala, E., Aguesse, F., Villarreal, I., Rodríguez-Martínez, L., López, C. & Kubiak, P. Understanding Lithium Inventory Loss and Sudden Performance Fade in Cylindrical Cells during Cycling with Deep-Discharge Steps. *The Journal of Physical Chemistry C* **119**, 896 (2015).
95. Pastor-Fernández, C., Yu, T. F., Widanage, W. D. & Marco, J. Critical review of non-invasive diagnosis techniques for quantification of degradation modes in lithium-ion batteries. *Renewable and Sustainable Energy Reviews* **109**, 138 (2019).

96. Delacourt, C. & Safari, M. in *Physical Multiscale Modeling and Numerical Simulation of Electrochemical Devices for Energy Conversion and Storage: From Theory to Engineering to Practice* (eds Franco, A. A., Doublet, M. L. & Bessler, W. G.) 151 (Springer London, London, 2016).
97. Keil, P., Schuster, S. F., Wilhelm, J., Travi, J., Hauser, A., Karl, R. C. & Jossen, A. Calendar Aging of Lithium-Ion Batteries. *Journal of The Electrochemical Society* **163**, A1872 (2016).
98. Arora, P., White, R. E. & Doyle, M. Capacity Fade Mechanisms and Side Reactions in Lithium-Ion Batteries. *Journal of The Electrochemical Society* **145**, 3647 (1998).
99. Park, J., Appiah, W. A., Byun, S., Jin, D., Ryou, M.-H. & Lee, Y. M. Semi-empirical long-term cycle life model coupled with an electrolyte depletion function for large-format graphite/LiFePO₄ lithium-ion batteries. *Journal of Power Sources* **365**, 257 (2017).
100. Xu, B., Oudalov, A., Ulbig, A., Andersson, G. & Kirschen, D. S. Modeling of Lithium-Ion Battery Degradation for Cell Life Assessment. *IEEE Transactions on Smart Grid* **9**, 1131 (2018).
101. Peled, E., Bar Tow, D., Merson, A., Gladkikh, A., Burstein, L. & Golodnitsky, D. Composition, depth profiles and lateral distribution of materials in the SEI built on HOPG-TOF SIMS and XPS studies. *Journal of Power Sources* **97-98**. Proceedings of the 10th International Meeting on Lithium Batteries, 52 (2001).
102. Han, X., Ouyang, M., Lu, L., Li, J., Zheng, Y. & Li, Z. A comparative study of commercial lithium ion battery cycle life in electrical vehicle: Aging mechanism identification. *Journal of Power Sources* **251**, 38 (2014).
103. Scrosati, B. & Garche, J. Lithium batteries: Status, prospects and future. *Journal of Power Sources* **195**, 2419 (2010).
104. Hall, J., Lin, T., Brown, G., Biensan, P. & Bonhomme, F. Decay Processes and Life Predictions for Lithium Ion Satellite Cells (2006).
105. Maheshwari, A. *Modelling, aging and optimal operation of lithium-ion batteries* Proefschrift. PhD thesis (Department of Electrical Engineering, 2018).

106. Lin, N., Jia, Z., Wang, Z., Zhao, H., Ai, G., Song, X., Bai, Y., Battaglia, V., Sun, C., Qiao, J., Wu, K. & Liu, G. Understanding the crack formation of graphite particles in cycled commercial lithium-ion batteries by focused ion beam - scanning electron microscopy. *Journal of Power Sources* **365**, 235 (2017).
107. Koltypin, M., Cohen, Y. S., Markovsky, B., Cohen, Y. & Aurbach, D. The study of lithium insertion–deinsertion processes into composite graphite electrodes by in situ atomic force microscopy (AFM). *Electrochemistry Communications* **4**, 17 (2002).
108. Ekstrom, H. *Electrode Balancing of a Lithium-Ion Battery with COMSOL* <https://www.comsol.com/blogs/electrode-balancing-of-a-lithium-ion-battery-with-comsol/>.
109. Ploehn, H. J., Ramadass, P. & White, R. E. Solvent Diffusion Model for Aging of Lithium-Ion Battery Cells. *Journal of The Electrochemical Society* **151**, A456 (2004).
110. Ecker, M., Gerschler, J. B., Vogel, J., Käbitz, S., Hust, F., Dechent, P. & Sauer, D. U. Development of a lifetime prediction model for lithium-ion batteries based on extended accelerated aging test data. *Journal of Power Sources* **215**, 248 (2012).
111. Wohlfahrt-Mehrens, M., Vogler, C. & Garche, J. Aging mechanisms of lithium cathode materials. *Journal of Power Sources* **127**. Eighth Ulmer Electrochemische Tage, 58 (2004).
112. Liao, X., Huang, Q., Mai, S., Wang, X., Xu, M., Xing, L., Liao, Y. & Li, W. Understanding self-discharge mechanism of layered nickel cobalt manganese oxide at high potential. *Journal of Power Sources* **286**, 551 (2015).
113. Joshi, T., Eom, K., Yushin, G. & Fuller, T. F. Effects of Dissolved Transition Metals on the Electrochemical Performance and SEI Growth in Lithium-Ion Batteries. *Journal of The Electrochemical Society* **161**, A1915 (2014).
114. Li, W. Review—An Unpredictable Hazard in Lithium-ion Batteries from Transition Metal Ions: Dissolution from Cathodes, Deposition on Anodes and Elimination Strategies. *Journal of The Electrochemical Society* **167**, 090514 (2020).

115. Yi, T.-F., Jiang, L.-J., Shu, J., Yue, C.-B., Zhu, R.-S. & Qiao, H.-B. Recent development and application of $\text{Li}_4\text{Ti}_5\text{O}_{12}$ as anode material of lithium ion battery. *Journal of Physics and Chemistry of Solids* **71**, 1236 (2010).
116. Lu, W., Liu, J., Sun, Y. & Amine, K. Electrochemical performance of $\text{Li}_{4/3}\text{Ti}_5/3\text{O}_4/\text{Li}_{1+x}(\text{Ni}_{1/3}\text{Co}_{1/3}\text{Mn}_{1/3})_{1-x}\text{O}_2$ cell for high power applications. *Journal of Power Sources* **167**, 212 (2007).
117. Priyono, B., Winowatan, P. W., Syahrial, A. Z., Faizah & Subhan, A. Optimizing the performance of $\text{Li}_4\text{Ti}_5\text{O}_{12}$ /LTO by addition of silicon microparticle in half cell lithium-ion battery anode. *IOP Conference Series: Earth and Environmental Science* **105**, 012121 (2018).
118. Zhan, C., Wu, T., Lu, J. & Amine, K. Dissolution, migration, and deposition of transition metal ions in Li-ion batteries exemplified by Mn-based cathodes – a critical review. *Energy Environ. Sci.* **11**, 243 (2018).
119. Bourlot, S., Blanchard, P. & Robert, S. Investigation of aging mechanisms of high power Li-ion cells used for hybrid electric vehicles. *Journal of Power Sources* **196**. 15th International Meeting on Lithium Batteries (IMLB), 6841 (2011).
120. Kassem, M., Bernard, J., Revel, R., Pélissier, S., Duclaud, F. & Delacourt, C. Calendar aging of a graphite/LiFePO₄ cell. *Journal of Power Sources* **208**, 296 (2012).
121. Edström, K., Gustafsson, T. & Thomas, J. The cathode–electrolyte interface in the Li-ion battery. *Electrochimica Acta* **50**. Polymer Batteries and Fuel Cells: Selection of Papers from First International Conference, 397 (2004).
122. Amine, K., Liu, J., Belharouak, I., Kang, S.-H., Bloom, I., Vissers, D. & Henriksen, G. Advanced cathode materials for high-power applications. *Journal of Power Sources* **146**. Selected papers presented at the 12th International Meeting on Lithium Batteries, 111 (2005).
123. Aurbach, D., Gamolsky, K., Markovsky, B., Salitra, G., Gofer, Y., Heider, U., Oesten, R. & Schmidt, M. The Study of Surface Phenomena Related to Electrochemical Lithium Intercalation into $\text{Li}[\text{sub } x]\text{MO}[\text{sub } y]$ Host Materials (M = Ni, Mn). *Journal of The Electrochemical Society* **147**, 1322 (2000).

124. Love, C., Korovina, A., Patridge, C., Swider-Lyons, K., Twigg, M. & Ramaker, D. Review of LiFePO₄ Phase Transition Mechanisms and New Observations from X-ray Absorption Spectroscopy. *Journal of the Electrochemical Society* **160**, A3153 (2013).
125. Ellis, B. L., Lee, K. T. & Nazar, L. F. Positive Electrode Materials for Li-Ion and Li-Batteries. *Chemistry of Materials* **22**, 691 (2010).
126. Chung, K. Y. & Kim, K.-B. Investigations into capacity fading as a result of a Jahn–Teller distortion in 4V LiMn₂O₄ thin film electrodes. *Electrochimica Acta* **49**, 3327 (2004).
127. Li, X., Xu, Y. & Wang, C. Suppression of Jahn–Teller distortion of spinel LiMn₂O₄ cathode. *Journal of Alloys and Compounds* **479**, 310 (2009).
128. Lewerenz, M., Münnix, J., Schmalstieg, J., Käbitz, S., Knips, M. & Sauer, D. U. Systematic aging of commercial LiFePO₄|Graphite cylindrical cells including a theory explaining rise of capacity during aging. *Journal of Power Sources* **345**, 254 (2017).
129. Lewerenz, M., Fuchs, G., Becker, L. & Sauer, D. U. Irreversible calendar aging and quantification of the reversible capacity loss caused by anode overhang. *Journal of Energy Storage* **18**, 149 (2018).
130. Redondo-Iglesias, E., Venet, P. & Pelissier, S. Eyring acceleration model for predicting calendar ageing of lithium-ion batteries. *Journal of Energy Storage* **13**, 176 (2017).
131. Stroe, D. *Lifetime Models for Lithium-ion Batteries used in Virtual Power Plant Applications* PhD thesis (2014).
132. Grolleau, S., Delaille, A., Gualous, H., Gyan, P., Revel, R., Bernard, J., Redondo-Iglesias, E. & Peter, J. Calendar aging of commercial graphite/LiFePO₄ cell – Predicting capacity fade under time dependent storage conditions. *Journal of Power Sources* **255**, 450 (2014).
133. Sarasketa-Zabala, E., Gandiaga, I., Rodriguez-Martinez, L. & Villarreal, I. Calendar ageing analysis of a LiFePO₄/graphite cell with dynamic model validations: Towards realistic lifetime predictions. *Journal of Power Sources* **272**, 45 (2014).
134. Zheng, Y., He, Y.-B., Qian, K., Li, B., Wang, X., Li, J., Miao, C. & Kang, F. Effects of state of charge on the degradation of LiFePO₄/graphite batteries during accelerated storage test. *Journal of Alloys and Compounds* **639**, 406 (2015).

135. Stroe, D., Swierczynski, M., Kær, S. K. & Teodorescu, R. Degradation Behavior of Lithium-Ion Batteries During Calendar Ageing—The Case of the Internal Resistance Increase. *IEEE Transactions on Industry Applications* **54**, 517 (2018).
136. Bloom, I., Cole, B., Sohn, J., Jones, S., Polzin, E., Battaglia, V., Henriksen, G., Motloch, C., Richardson, R., Unkelhaeuser, T., Ingersoll, D. & Case, H. An accelerated calendar and cycle life study of Li-ion cells. *Journal of Power Sources* **101**, 238 (2001).
137. Swierczynski, M., Stroe, D., Stan, A., Teodorescu, R. & Kær, S. K. Lifetime Estimation of the Nanophosphate LiFePO_4/C Battery Chemistry Used in Fully Electric Vehicles. *IEEE Transactions on Industry Applications* **51**, 3453 (2015).
138. Eddahech, A., Briat, O. & Vinassa, J.-M. Performance comparison of four lithium-ion battery technologies under calendar aging. *Energy* **84**, 542 (2015).
139. Röder, P., Stiaszny, B., Ziegler, J. C., Baba, N., Lagaly, P. & Wiemhöfer, H.-D. The impact of calendar aging on the thermal stability of a $\text{LiMn}_2\text{O}_4\text{-Li}(\text{Ni}_{1/3}\text{Mn}_{1/3}\text{Co}_{1/3})\text{O}_2/\text{graphite}$ lithium-ion cell. *Journal of Power Sources* **268**, 315 (2014).
140. Belt, J., Utgikar, V. & Bloom, I. Calendar and PHEV cycle life aging of high-energy, lithium-ion cells containing blended spinel and layered-oxide cathodes. *Journal of Power Sources* **196**, 10213 (2011).
141. Julius, Maheshwari, A., Heck, M., Lux, S. & Vetter, M. Impedance change and capacity fade of lithium nickel manganese cobalt oxide-based batteries during calendar aging. *Journal of Power Sources* **353**, 183 (2017).
142. de Hoog, J., Timmermans, J.-M., Ioan-Stroe, D., Swierczynski, M., Jaguemont, J., Goutam, S., Omar, N., Van Mierlo, J. & Van Den Bossche, P. Combined cycling and calendar capacity fade modeling of a Nickel-Manganese-Cobalt Oxide Cell with real-life profile validation. *Applied Energy* **200**, 47 (2017).
143. Wang, J., Purewal, J., Liu, P., Hicks-Garner, J., Soukazian, S., Sherman, E., Sorenson, A., Vu, L., Tataria, H. & Verbrugge, M. Degradation of lithium ion batteries employing graphite negatives and nickel-cobalt-manganese oxide + spinel manganese oxide positives: Part 1, aging mechanisms and life estimation. *Journal of Power Sources* **269** (2014).

144. Baghdadi, I., Briat, O., Delétage, J.-Y., Gyan, P. & Vinassa, J.-M. Lithium battery aging model based on Dakin's degradation approach. *Journal of Power Sources* **325**, 273 (2016).
145. Thomas, E., Bloom, I., Christophersen, J. & Battaglia, V. Statistical methodology for predicting the life of lithium-ion cells via accelerated degradation testing. *Journal of Power Sources* **184**, 312 (2008).
146. Redondo-Iglesias, E., Venet, P. & Pélissier, S. Influence of the non-conservation of SoC value during calendar ageing tests on modelling the capacity loss of batteries, 1 (2015).
147. Yoshida, H., Imamura, N., Inoue, T., Takeda, K. & Naito, H. Verification of Life Estimation Model for Space Lithium-Ion Cells. *Electrochemistry* **78**, 482 (2010).
148. Buller, S. *Impedance based simulation models for energy storage devices in advanced automotive power systems* Zugl.: Aachen, Techn. Hochsch., Diss., 2002. PhD thesis (Aachen, 2003), 138 S. : Ill., graph. Darst.
149. Andre, D., Meiler, M., Steiner, K., Walz, H., Soczka-Guth, T. & Sauer, D. Characterization of high-power lithium-ion batteries by electrochemical impedance spectroscopy. II: Modelling. *Journal of Power Sources* **196**, 5349 (2011).
150. Käbitz, S., Gerschler, J. B., Ecker, M., Yurdagel, Y., Emmermacher, B., André, D., Mitsch, T. & Sauer, D. U. Cycle and calendar life study of a graphite | $\text{LiNi}_{1/3}\text{Mn}_{1/3}\text{Co}_{1/3}\text{O}_2$ Li-ion high energy system. Part A: Full cell characterization. *Journal of Power Sources* **239**, 572 (2013).
151. Ecker, M., Nieto, N., Käbitz, S., Schmalstieg, J., Blanke, H., Warnecke, A. & Sauer, D. U. Calendar and cycle life study of $\text{Li}(\text{NiMnCo})\text{O}_2$ -based 18650 lithium-ion batteries. *Journal of Power Sources* **248**, 839 (2014).
152. Lam, L. & Bauer, P. Practical Capacity Fading Model for Li-Ion Battery Cells in Electric Vehicles. *IEEE Transactions on Power Electronics* **28**, 5910 (2013).
153. Reichert, M., Andre, D., Rösmann, A., Janssen, P., Bremes, H.-G., Sauer, D., Passerini, S. & Winter, M. Influence of relaxation time on the lifetime of commercial lithium-ion cells. *Journal of Power Sources* **239**, 45 (2013).

154. Ecker, M., Gerschler, J. B., Vogel, J., Käbitz, S., Hust, F., Dechent, P. & Sauer, D. U. Development of a lifetime prediction model for lithium-ion batteries based on extended accelerated aging test data. *Journal of Power Sources* **215**, 248 (2012).
155. Millner, A. Modeling Lithium Ion battery degradation in electric vehicles, 349 (2010).
156. Guenther, C., Schott, B., Hennings, W., Waldowski, P. & Danzer, M. A. Model-based investigation of electric vehicle battery aging by means of vehicle-to-grid scenario simulations. *Journal of Power Sources* **239**, 604 (2013).
157. Wright, R., Motloch, C., Belt, J., Christophersen, J., Ho, C., Richardson, R., Bloom, I., Jones, S., Battaglia, V., Henriksen, G., Unkelhaeuser, T., Ingersoll, D., Case, H., Rogers, S. & Sutula, R. Calendar- and cycle-life studies of advanced technology development program generation 1 lithium-ion batteries. *Journal of Power Sources* **110**, 445 (2002).
158. Rechkemmer, S. K., Zang, X., Zhang, W. & Sawodny, O. Empirical Li-ion aging model derived from single particle model. *Journal of Energy Storage* **21**, 773 (2019).
159. Petit, M., Prada, E. & Sauvant-Moynot, V. Development of an empirical aging model for Li-ion batteries and application to assess the impact of Vehicle-to-Grid strategies on battery lifetime. *Applied Energy* **172**, 398 (2016).
160. Sethuraman, V. A., Hardwick, L. J., Srinivasan, V. & Kostecki, R. Surface structural disordering in graphite upon lithium intercalation/deintercalation. *Journal of Power Sources* **195**, 3655 (2010).
161. Manka, D. & Ivers-Tiffée, E. Electro-optical measurements of lithium intercalation/de-intercalation at graphite anode surfaces. *Electrochimica Acta* **186**, 642 (2015).
162. Wang, J., Liu, P., Hicks-Garner, J., Sherman, E., Soukiazian, S., Verbrugge, M., Tataria, H., Musser, J. & Finamore, P. Cycle-life model for graphite-LiFePO₄ cells. *Journal of Power Sources* **196**, 3942 (2011).
163. Omar, N., Abdel Monem, M., Firouz, Y., Salminen, J., Smekens, J., Hegazy, O., Gualous, H., Mulder, G., Van den Bossche, P., Coosemans, T. & Van Mierlo, J. Lithium iron phosphate based battery – Assessment of the aging parameters and development of cycle life model. *Applied Energy* **113**, 1575 (2014).

164. Suri, G. & Onori, S. A control-oriented cycle-life model for hybrid electric vehicle lithium-ion batteries. *Energy* **96**, 644 (2016).
165. Li, Z., Lu, L., Ouyang, M. & Xiao, Y. Modeling the capacity degradation of LiFePO₄/graphite batteries based on stress coupling analysis. *Journal of Power Sources* **196**, 9757 (2011).
166. Sarasketa-Zabala, E., Gandiaga, I., Martinez-Laserna, E., Rodriguez-Martinez, L. & Villarreal, I. Cycle ageing analysis of a LiFePO₄/graphite cell with dynamic model validations: Towards realistic lifetime predictions. *Journal of Power Sources* **275**, 573 (2015).
167. Todeschini, F., Onori, S. & Rizzoni, G. An experimentally validated capacity degradation model for Li-ion batteries in PHEVs applications. *IFAC Proceedings Volumes* **45**. 8th IFAC Symposium on Fault Detection, Supervision and Safety of Technical Processes, 456 (2012).
168. Bacci, M. L., Cheli, F., Sabbioni, E., Tarsitano, D. & Vignati, M. Aging models for high capacity LiFePO₄ cells, 1 (2017).
169. Ebrahimi, M., Rastegar, M., Mohammadi, M., Palomino, A. & Parvania, M. Stochastic Charging Optimization of V2G-Capable PEVs: A Comprehensive Model for Battery Aging and Customer Service Quality. *IEEE Transactions on Transportation Electrification* **6**, 1026 (2020).
170. Schimpe, M., von Kuepach, M. E., Naumann, M., Hesse, H. C., Smith, K. & Jossen, A. Comprehensive Modeling of Temperature-Dependent Degradation Mechanisms in Lithium Iron Phosphate Batteries. *Journal of The Electrochemical Society* **165**, A181 (2018).
171. Ouyang, M., Feng, X., Han, X., Lu, L., Li, Z. & He, X. A dynamic capacity degradation model and its applications considering varying load for a large format Li-ion battery. *Applied Energy* **165**, 48 (2016).
172. Cordoba-Arenas, A., Onori, S., Guezennec, Y. & Rizzoni, G. Capacity and power fade cycle-life model for plug-in hybrid electric vehicle lithium-ion battery cells containing blended spinel and layered-oxide positive electrodes. *Journal of Power Sources* **278**, 473 (2015).
173. Mauri, M., Castelli-Dezza, F., Carmeli, M. S., Scarforoglio, M. & Marchegiani, G. Electro-Thermal Aging Model of Li -Ion Batteries for Vehicle-to-Grid Services, 1 (2019).
174. Hoke, A., Brissette, A., Smith, K., Pratt, A. & Maksimovic, D. Accounting for Lithium-Ion Battery Degradation in Electric Vehicle Charging Optimization. *IEEE Journal of Emerging and Selected Topics in Power Electronics* **2**, 691 (2014).

175. Smith, K., Earleywine, M., Wood, E., Neubauer, J. & Pesaran, A. Comparison of Plug-In Hybrid Electric Vehicle Battery Life Across Geographies and Drive-Cycles. **1** (2012).
176. Su, L., Zhang, J., Wang, C., Zhang, Y., Li, Z., Song, Y., Jin, T. & Ma, Z. Identifying main factors of capacity fading in lithium ion cells using orthogonal design of experiments. *Applied Energy* **163**, 201 (2016).
177. Sangwan, V., Kumar, R. & Rathore, A. K. An Empirical Capacity Degradation Modeling and Prognostics of Remaining Useful Life of Li-ion Battery using Unscented Kalman Filter, **1** (2018).
178. Dai, H., Zhang, X., Gu, W., Wei, X. & Sun, Z. A Semi-Empirical Capacity Degradation Model of EV Li-Ion Batteries Based on Eyring Equation, **1** (2013).
179. Gao, Y., Jiang, J., Zhang, C., Zhang, W., Ma, Z. & Jiang, Y. Lithium-ion battery aging mechanisms and life model under different charging stresses. *Journal of Power Sources* **356**, 103 (2017).
180. Cui, Y., Du, C., Yin, G., Gao, Y., Zhang, L., Guan, T., Yang, L. & Wang, F. Multi-stress factor model for cycle lifetime prediction of lithium ion batteries with shallow-depth discharge. *Journal of Power Sources* **279**. 9th International Conference on Lead-Acid Batteries – LABAT 2014, 123 (2015).
181. Guo, J., Li, Z. & Pecht, M. A Bayesian approach for Li-Ion battery capacity fade modeling and cycles to failure prognostics. *Journal of Power Sources* **281**, 173 (2015).
182. Choi, S. S. & Lim, H. S. Factors that affect cycle-life and possible degradation mechanisms of a Li-ion cell based on LiCoO₂. *Journal of Power Sources* **111**, 130 (2002).
183. Marongiu, A., Roscher, M. & Sauer, D. U. Influence of the vehicle-to-grid strategy on the aging behavior of lithium battery electric vehicles. *Applied Energy* **137**, 899 (2015).
184. Dufo-López, R. & Bernal-Agustín, J. L. Multi-objective design of PV-wind-diesel-hydrogen-battery systems. *Renewable Energy* **33**, 2559 (2008).
185. Mishra, S., Pecht, M., Smith, T., McNee, I. & Harris, R. Remaining life prediction of electronic products using life consumption monitoring approach (2002).

186. Lee, Y.-L. & Tjhung, T. in *Metal Fatigue Analysis Handbook* (eds Lee, Y.-L., Barkey, M. E. & Kang, H.-T.) 89 (Butterworth-Heinemann, Boston, 2012).
187. Ratnakumar, B., Smart, M., Whitcanack, L. & Ewell, R. The Impedance characteristics of Mars Exploration Rover Li-ion batteries. *Journal of Power Sources* **159**, 1428 (2006).
188. Huang, C., Sakamoto, J., Wolfenstine, J. & Surampudi, S. The Limits of Low-Temperature Performance of Li-Ion Cells. *Journal of The Electrochemical Society* **147**, 2893 (2000).
189. Zhang, S., Xu, K. & Jow, R. 060. The low temperature performance of Li-ion batteries. *Journal of Power Sources* **115**, 137 (2003).
190. Waldmann, T., Wilka, M., Kasper, M., Fleischhammer, M. & Wohlfahrt-Mehrens, M. Temperature dependent ageing mechanisms in Lithium-ion batteries – A Post-Mortem study. *Journal of Power Sources* **262**, 129 (2014).
191. Bauer, M., Guenther, C., Kasper, M., Petzl, M. & Danzer, M. A. Discrimination of degradation processes in lithium-ion cells based on the sensitivity of aging indicators towards capacity loss. *Journal of Power Sources* **283**, 494 (2015).
192. Lin, H.-p., Chua, D., Salomon, M., Shiao, H.-C., Hendrickson, M., Plichta, E. & Slane, S. Low-Temperature Behavior of Li-Ion Cells. *Electrochemical and Solid-State Letters* **4**, A71 (2001).
193. Ning, G., Haran, B. & Popov, B. N. Capacity fade study of lithium-ion batteries cycled at high discharge rates. *Journal of Power Sources* **117**, 160 (2003).
194. Zhang, S. S. The effect of the charging protocol on the cycle life of a Li-ion battery. *Journal of Power Sources* **161**, 1385 (2006).
195. Jalkanen, K., Karppinen, J., Skogström, L., Laurila, T., Nisula, M. & Vuorilehto, K. Cycle aging of commercial NMC/graphite pouch cells at different temperatures. *Applied Energy* **154**, 160 (2015).
196. Schuster, S. F., Bach, T., Fleder, E., Müller, J., Brand, M., Sextl, G. & Jossen, A. Nonlinear aging characteristics of lithium-ion cells under different operational conditions. *Journal of Energy Storage* **1**, 44 (2015).
197. Niehoff, P., Kraemer, E. & Winter, M. Parametrisation of the influence of different cycling conditions on the capacity fade and the internal resistance increase for lithium nickel manganese cobalt oxide/graphite cells. *Journal of Electroanalytical Chemistry* **707**, 110 (2013).

198. Gantenbein, S., Schönleber, M., Weiss, M. & Ivers-Tiffée, E. Capacity Fade in Lithium-Ion Batteries and Cyclic Aging over Various State-of-Charge Ranges. *Sustainability* **11** (2019).
199. Mercer, M. P., Otero, M., Ferrer-Huerta, M., Sigal, A., Barraco, D. E., Hoster, H. E. & Leiva, E. P. Transitions of lithium occupation in graphite: A physically informed model in the dilute lithium occupation limit supported by electrochemical and thermodynamic measurements. *Electrochimica Acta* **324**, 134774 (2019).
200. Koller, M., Borsche, T., Ulbig, A. & Andersson, G. Defining a degradation cost function for optimal control of a battery energy storage system, **1** (2013).
201. Oh, K.-Y., Siegel, J. B., Secondo, L., Kim, S. U., Samad, N. A., Qin, J., Anderson, D., Garikipati, K., Knobloch, A., Epureanu, B. I., Monroe, C. W. & Stefanopoulou, A. Rate dependence of swelling in lithium-ion cells. *Journal of Power Sources* **267**, 197 (2014).
202. Dahn, J. Phase diagram of Li_xC_6 . *Physical Review B* **44**. cited By 669, 9170 (1991).
203. Fuller, T., Doyle, M. & Newman, J. Simulation and Optimization of the Dual Lithium Ion Insertion Cell. *Journal of the Electrochemical Society* **141**. cited By 1080, 1 (1994).
204. Zhang, W.-J. Structure and performance of LiFePO_4 cathode materials: A review. *Journal of Power Sources* **196**, 2962 (2011).
205. Masquelier, C., Patoux, S., Wurm, C. & Morcrette, M. Polyanion-Based Positive Electrode Materials (2003).
206. Shu, X., Guo, Y., Yang, W., Wei, K. & Zhu, G. Life-cycle assessment of the environmental impact of the batteries used in pure electric passenger cars. *Energy Reports* **7**, 2302 (2021).
207. Deng, D. Li-ion batteries: basics, progress, and challenges. *Energy Science & Engineering* **3**, 385.
208. Etacheri, V., Marom, R., Elazari, R., Salitra, G. & Aurbach, D. Challenges in the development of advanced Li-ion batteries: a review. *Energy Environ. Sci.* **4**, 3243 (9 2011).
209. Martinez-Laserna, E., Sarasketa-Zabala, E., Villarreal Sarria, I., Stroe, D.-I., Swierczynski, M., Warnecke, A., Timmermans, J.-M., Goutam, S., Omar, N. & Rodriguez, P. Technical Viability of Battery Second Life: A Study From the Ageing Perspective. *IEEE Transactions on Industry Applications* **54**, 2703 (2018).

210. Mathews, I., Xu, B., He, W., Barreto, V., Buonassisi, T. & Peters, I. M. Technoeconomic model of second-life batteries for utility-scale solar considering calendar and cycle aging. *Applied Energy* **269**, 115127 (2020).
211. Aghabali, I., Bauman, J., Kollmeyer, P. J., Wang, Y., Bilgin, B. & Emadi, A. 800-V Electric Vehicle Powertrains: Review and Analysis of Benefits, Challenges, and Future Trends. *IEEE Transactions on Transportation Electrification* **7**, 927 (2021).
212. FASTNED. *FastNed - Vehicles and charging tips* <https://support.fastned.nl/hc/en-gb/sections/115000180588-Vehicles-charging-tips?page=1#articles>.
213. Fergus, J. Recent developments in cathode materials for lithium ion batteries. *Journal of Power Sources* **195**, 939 (2010).
214. Muratori, M. & Rizzoni, G. Residential Demand Response: Dynamic Energy Management and Time-Varying Electricity Pricing. *IEEE Transactions on Power Systems* **31**, 1108 (2016).
215. Wang, S., Bi, S. & Zhang, Y. A Demand Response Management for Profit Maximizing Energy Loads in Real-Time Electricity Market. *IEEE Transactions on Power Systems* **33**, 6387 (2018).
216. Rassaei, F., Soh, W. & Chua, K. Distributed Scalable Autonomous Market-Based Demand Response via Residential Plug-In Electric Vehicles in Smart Grids. *IEEE Transactions on Smart Grid* **9**, 3281 (2018).
217. Yan, Q., Zhang, B. & Kezunovic, M. Optimized Operational Cost Reduction for an EV Charging Station Integrated With Battery Energy Storage and PV Generation. *IEEE Transactions on Smart Grid* **10**, 2096 (2019).
218. Pilloni, V., Floris, A., Meloni, A. & Atzori, L. Smart Home Energy Management Including Renewable Sources: A QoE-Driven Approach. *IEEE Transactions on Smart Grid* **9**, 2006 (2018).
219. Liberati, F., Giorgio, A. D., Giuseppi, A., Pietrabissa, A., Habib, E. & Martirano, L. Joint Model Predictive Control of Electric and Heating Resources in a Smart Building. *IEEE Transactions on Industry Applications* **55**, 7015 (2019).
220. Althaher, S., Mancarella, P. & Mutale, J. Automated Demand Response From Home Energy Management System Under Dynamic Pricing and Power and Comfort Constraints. *IEEE Transactions on Smart Grid* **6**, 1874 (2015).

221. Sharma, S., Xu, Y., Verma, A. & Panigrahi, B. K. Time-Coordinated Multienergy Management of Smart Buildings Under Uncertainties. *IEEE Transactions on Industrial Informatics* **15**, 4788 (2019).
222. Hadi, A. A., Silva, C. A. S., Hossain, E. & Challoo, R. Algorithm for Demand Response to Maximize the Penetration of Renewable Energy. *IEEE Access* **8**, 55279 (2020).
223. Manganeli, M., Greco, G. & Martirano, L. Design of a New Architecture and Simulation Model for Building Automation Toward Nearly Zero Energy Buildings. *IEEE Transactions on Industry Applications* **55**, 6999 (2019).
224. Hafiz, F., Awal, M. A., d. Queiroz, A. R. & Husain, I. Real-Time Stochastic Optimization of Energy Storage Management Using Deep Learning-Based Forecasts for Residential PV Applications. *IEEE Transactions on Industry Applications* **56**, 2216 (2020).
225. Tan, X., Qu, G., Sun, B., Li, N. & Tsang, D. H. K. Optimal Scheduling of Battery Charging Station Serving Electric Vehicles Based on Battery Swapping. *IEEE Transactions on Smart Grid* **10**, 1372 (2019).
226. Amamra, S.-A. & Marco, J. Vehicle-to-Grid Aggregator to Support Power Grid and Reduce Electric Vehicle Charging Cost. *IEEE Access* **7**, 178528 (2019).
227. Chaudhari, K., Ukil, A., Kumar, K. N., Manandhar, U. & Kollimalla, S. K. Hybrid Optimization for Economic Deployment of ESS in PV-Integrated EV Charging Stations. *IEEE Transactions on Industrial Informatics* **14**, 106 (2018).
228. Ahmadian, A., Sedghi, M., Mohammadi-ivatloo, B., Elkamel, A., Aliakbar Golkar, M. & Fowler, M. Cost-Benefit Analysis of V2G Implementation in Distribution Networks Considering PEVs Battery Degradation. *IEEE Transactions on Sustainable Energy* **9**, 961 (2018).
229. Cao, J., Harrold, D., Fan, Z., Morstyn, T., Healey, D. & Li, K. Deep Reinforcement Learning-Based Energy Storage Arbitrage With Accurate Lithium-Ion Battery Degradation Model. *IEEE Transactions on Smart Grid* **11**, 4513 (2020).
230. Padmanabhan, N., Ahmed, M. & Bhattacharya, K. Battery Energy Storage Systems in Energy and Reserve Markets. *IEEE Transactions on Power Systems* **35**, 215 (2020).

231. Leonori, S., Rizzoni, G., Frattale Mascioli, F. M. & Rizzi, A. Intelligent energy flow management of a nanogrid fast charging station equipped with second life batteries. *International Journal of Electrical Power & Energy Systems* **127**, 106602 (2021).
232. Deng, Y., Zhang, Y., Luo, F. & Mu, Y. Operational Planning of Centralized Charging Stations Utilizing Second-Life Battery Energy Storage Systems. *IEEE Transactions on Sustainable Energy* **12**, 387 (2021).
233. Chandra Mouli, G. R., Kefayati, M., Baldick, R. & Bauer, P. Integrated PV Charging of EV Fleet Based on Energy Prices, V2G, and Offer of Reserves. *IEEE Transactions on Smart Grid* **10**, 1313 (2019).
234. Conte, F., Massucco, S., Schiapparelli, G.-P. & Silvestro, F. Day-Ahead and Intra-Day Planning of Integrated BESS-PV Systems Providing Frequency Regulation. *IEEE Transactions on Sustainable Energy* **11**, 1797 (2020).
235. Donadee, J. & Ilić, M. D. Stochastic Optimization of Grid to Vehicle Frequency Regulation Capacity Bids. *IEEE Transactions on Smart Grid* **5**, 1061 (2014).
236. Jin, C., Tang, J. & Ghosh, P. Optimizing Electric Vehicle Charging With Energy Storage in the Electricity Market. *IEEE Transactions on Smart Grid* **4**, 311 (2013).
237. Yao, E., Wong, V. W. S. & Schober, R. Robust Frequency Regulation Capacity Scheduling Algorithm for Electric Vehicles. *IEEE Transactions on Smart Grid* **8**, 984 (2017).
238. Padmanabhan, N., Ahmed, M. & Bhattacharya, K. Battery Energy Storage Systems in Energy and Reserve Markets. *IEEE Transactions on Power Systems* **35**, 215 (2020).
239. Mégel, O., Mathieu, J. L. & Andersson, G. Scheduling distributed energy storage units to provide multiple services under forecast error. *International Journal of Electrical Power & Energy Systems* **72**. The Special Issue for 18th Power Systems Computation Conference., 48 (2015).
240. Engels, J., Claessens, B. & Deconinck, G. Combined Stochastic Optimization of Frequency Control and Self-Consumption With a Battery. *IEEE Transactions on Smart Grid* **10**, 1971 (2019).
241. Shi, Y., Xu, B., Wang, D. & Zhang, B. Using Battery Storage for Peak Shaving and Frequency Regulation: Joint Optimization for Superlinear Gains. *IEEE Transactions on Power Systems* **33**, 2882 (2018).

242. Cheng, B. & Powell, W. B. Co-Optimizing Battery Storage for the Frequency Regulation and Energy Arbitrage Using Multi-Scale Dynamic Programming. *IEEE Transactions on Smart Grid* **9**, 1997 (2018).
243. Han, S., Han, S. & Sezaki, K. Development of an Optimal Vehicle-to-Grid Aggregator for Frequency Regulation. *IEEE Transactions on Smart Grid* **1**, 65 (2010).
244. Sun, S., Dong, M. & Liang, B. Real-Time Welfare-Maximizing Regulation Allocation in Dynamic Aggregator-EVs System. *IEEE Transactions on Smart Grid* **5**, 1397 (2014).
245. Hasanpor Divshali, P. & Evens, C. Optimum Operation of Battery Storage System in Frequency Containment Reserves Markets. *IEEE Transactions on Smart Grid* **11**, 4906 (2020).
246. Oudalov, A., Chartouni, D. & Ohler, C. Optimizing a Battery Energy Storage System for Primary Frequency Control. *IEEE Transactions on Power Systems* **22**, 1259 (2007).
247. Kahrobaee, S., Asgarpoor, S. & Qiao, W. Optimum Sizing of Distributed Generation and Storage Capacity in Smart Households. *IEEE Transactions on Smart Grid* **4**, 1791 (2013).
248. Naghibi, B., Masoum, M. A. S. & Deilami, S. Effects of V2H Integration on Optimal Sizing of Renewable Resources in Smart Home Based on Monte Carlo Simulations. *IEEE Power and Energy Technology Systems Journal* **5**, 73 (2018).
249. Bandyopadhyay, S., Chandra Mouli, G. R., Qin, Z., Elizondo, L. R. & Bauer, P. Techno-economical Model based Optimal Sizing of PV-Battery Systems for Microgrids. *IEEE Transactions on Sustainable Energy*, 1 (2019).
250. Yang, Y., Li, H., Aichhorn, A., Zheng, J. & Greenleaf, M. Sizing Strategy of Distributed Battery Storage System With High Penetration of Photovoltaic for Voltage Regulation and Peak Load Shaving. *IEEE Transactions on Smart Grid* **5**, 982 (2014).
251. Masaud, T. M. & El-Saadany, E. F. Correlating Optimal Size, Cycle Life Estimation, and Technology Selection of Batteries: A Two-Stage Approach for Microgrid Applications. *IEEE Transactions on Sustainable Energy* **11**, 1257 (2020).
252. Hafiz, F., de Queiroz, A. R., Fajri, P. & Husain, I. Energy management and optimal storage sizing for a shared community: A multi-stage stochastic programming approach. *Applied Energy* **236**, 42 (2019).

253. von Appen, J. & Braun, M. Sizing and Improved Grid Integration of Residential PV Systems With Heat Pumps and Battery Storage Systems. *IEEE Transactions on Energy Conversion* **34**, 562 (2019).
254. Atia, R. & Yamada, N. Sizing and Analysis of Renewable Energy and Battery Systems in Residential Microgrids. *IEEE Transactions on Smart Grid* **7**, 1204 (2016).
255. Saez-de-Ibarra, A., Martinez-Laserna, E., Stroe, D.-I., Swierczynski, M. & Rodriguez, P. Sizing Study of Second Life Li-ion Batteries for Enhancing Renewable Energy Grid Integration. *IEEE Transactions on Industry Applications* **52**, 4999 (2016).
256. Graber, G., Galdi, V., Calderaro, V. & Mancarella, P. A stochastic approach to size EV charging stations with support of second life battery storage systems, **1** (2017).
257. Paul, S. & Padhy, N. P. Real-Time Bilevel Energy Management of Smart Residential Apartment Building. *IEEE Transactions on Industrial Informatics* **16**, 3708 (2020).
258. Fu, R., Remo, T. & Margolis, R. 2018 U.S. Utility-Scale Photovoltaics Plus Energy Storage System Costs Benchmark.
259. Singh, A., Reese, S. & Akar, S. Performance and Techno-Economic Evaluation of a Three-Phase, 50-kW SiC-Based PV Inverter, 0695 (2019).
260. Kelly, K., Smith, K., Cosgrove, J., Prohaska, B. & Pesaran, A. Battery Ownership Model - Medium Duty HEV Battery Leasing & Standardization" (2015).
261. Administration, U. E. I. Battery Storage in the United States: An Update on Market Trends (2020).
262. TenneT. *Final Report FCR Pilot* https://netztransparenz.tennet.eu/fileadmin/user_upload/S0_NL/FCR_Final_report_FCR_pilot_alleen_in_Engels_.pdf.
263. TenneT. *FCR Manual for BSP's* https://netztransparenz.tennet.eu/fileadmin/user_upload/S0_NL/Handboek_FCR_voor_BSPs_-_EN_version.pdf.
264. ENTSOE. *Price of Reserved Balancing Reserves* <https://transparency.entsoe.eu/balancing/r2/balancingVolumesReservationPrice/show>.

265. Stein, J. S., Robinson, C., King, B., Deline, C., Rummel, S. & Sekulic, B. PV Lifetime Project: Measuring PV Module Performance Degradation: 2018 Indoor Flash Testing Results, 0771 (2018).
266. Europe-SolarStore.com. *LG chem RESU 10H - 400V lithium-ion storage battery* <https://www.europe-solarstore.com/lg-chem-resu-10h-400v-lithium-ion-storage-battery.html>.
267. van der Meer, D., Chandra Mouli, G. R., Morales-España Mouli, G., Elizondo, L. R. & Bauer, P. Energy Management System With PV Power Forecast to Optimally Charge EVs at the Workplace. *IEEE Transactions on Industrial Informatics* **14**, 311 (2018).
268. Wang, J., Purewal, J., Liu, P., Hicks-Garner, J., Soukazian, S., Sherman, E., Sorenson, A., Vu, L., Tataria, H. & Verbrugge, M. W. Degradation of lithium ion batteries employing graphite negatives and nickel-cobalt-manganese oxide + spinel manganese oxide positives: Part 1, aging mechanisms and life estimation. *Journal of Power Sources* **269**, 937 (2014).
269. Baccouche, I., Jemmali, S., Manai, B., Omar, N. & ESSOUKRI BEN AMARA, N. Improved OCV model of a Li-ion NMC battery for online SOC estimation using the extended Kalman filter. *Energies* **10**, 764 (2017).
270. YOSHIDA, H., IMAMURA, N., INOUE, T., TAKEDA, K. & NAITO, H. Verification of Life Estimation Model for Space Lithium-Ion Cells. *Electrochemistry* **78**, 482 (2010).
271. Voulis, N. Harnessing Heterogeneity Understanding Urban Demand to Support the Energy Transition, 1 (2019).
272. Sadeghianpourhamami, N., Refa, N., Strobbe, M. & Devellder, C. Quantitive analysis of electric vehicle flexibility: A data-driven approach. *International Journal of Electrical Power & Energy Systems* **95**, 451 (2018).
273. Helmus, J., Spoelstra, J., Refa, N., Lees, M. & van den Hoed, R. Assessment of public charging infrastructure push and pull rollout strategies: The case of the Netherlands. *Energy Policy* **121**, 35 (2018).
274. KNMI. *Forecast of Solar Radiation in The Netherlands* <https://www.knmi.nl/research/observations-data-technology/projects>.
275. Laboratory, N. R. E. *Cost-Reduction Roadmap for Residential Solar Photovoltaics (PV), 2017–2030* <https://www.nrel.gov/docs/fy18osti/70748.pdf>.

276. Nelder, C. & Rogers, E. Reducing EV Charger Infrastructure Costs (2019).
277. EV, E. *Elaad open data sets* <https://platform.elaad.io/analyses.html>.
278. Vermeer, W., Mouli, G. R. C. & Bauer, P. Optimal Sizing and Control of a PV-EV-BES Charging System Including Primary Frequency Control and Component Degradation. *IEEE Open Journal of the Industrial Electronics Society* **3**, 236 (2022).
279. Li, J., Abdallah, T. & Sullivan, C. *Improved calculation of core loss with nonsinusoidal waveforms* in *Conference Record of the 2001 IEEE Industry Applications Conference. 36th IAS Annual Meeting (Cat. No.01CH37248)* **4** (2001), 2203.

ACKNOWLEDGEMENTS

Over the past years of completing this PhD journey, I have fantasized several times of completing this work and writing these acknowledgements. To be able to do this now, fills me with great joy and almost brings a tear to my eye. However, i could not and would not have done it without the support and care of many people. Without who it would not have been as fun. For this I would like to express my deepest gratitude.

I also would like to thank professor Pavol Bauer, my promotor, for giving me the opportunity to pursue my PhD.

To Francesca, Marco and Wenli, it has been great sharing the office with you, and doing this whole thing together. Francesca, after being my buddy during our master, I am so happy that we could do our PhDs together. Thank you for all the fun times we shared! Marco, it has been great spending time with you. Especially our times in LA and Crato have been highlights of my PhD. Thank you for that! Wenli, thank you for your kind spirit and all the good times we shared. It seems ages ago that the four of us went to Crato in our first year, and reminiscing back to those times fills me with joy. Thank you for that!

I also want to thank all other DCE&S colleagues! Having nice colleagues with whom to have good discussions; technical talks, but also bullshit talks has been great. A special shout out to all the people who made the conference trips so much fun! Thanks for everything and all the best in your futures.

Next, I would like to to the lab managers, Bart, Joris, Harry and Mladen, for your help when things got frustrating. But also thanks for our casual chats, which might have been just as helpful.

I have had the pleasure of joining the people at Power Research Electronics for the converter development. Marck, you have been super helpful during this process and I am really grateful for that. Also thanks to Jos, Mike, and Joshua for your contributions to this work!

I could not have done this without the never ending support of all my friends, you know who your are. Besides supporting me throughout my phd, you also gave me the opportunity to focus on other important things in life, and gave me the necessary distractions when i needed them the most. This helped me to grow as a person as well. I cannot express in words how much that means to me!

A special thanks to Annemieke for your endless care, loving, and support. Nobody has seen the level of emotion during this process, both the highs and the lows, as much as you have. And nobody has supported me as much as you have. I will always be grateful to you for that.

Finally, I would like to express my deepest gratitude to my parents. I dedicate this work to you, since a little piece of text can never convey what you mean to me.

CURRICULUM VITAE

PERSONAL DATA

Name	Wiljan Vermeer
Date of Birth	September 13, 1993
Place of Birth	's-Hertogenbosch
Citizen of	the Netherlands

EDUCATION

2016-2018	MSc Electrical Power Engineering Delft University of Technology Delft, The Netherlands
2011 – 2016	BSc Electrical Engineering Eindhoven University of Technology Eindhoven, The Netherlands

PUBLICATIONS

Articles in peer-reviewed journals:

1. Einstein, A. Über die von der molekularkinetischen Theorie der Wärme geforderte Bewegung von in ruhenden Flüssigkeiten suspendierten Teilchen. *Annalen der Physik* **322**, 549 (1905).
2. Einstein, A. Zur Elektrodynamik bewegter Körper. *Annalen der Physik* **322**, 891 (1905).

Conference contributions:

3. Einstein, A. *Implications of a fixed vacuum speed of light in Relativity* Oct. 2–6, 1905 (1st Conference on Special Relativity, Zurich, Switzerland).